Tailored Binder Concept for Water-Based Anode Slurries to Improve Li-ion Battery Performance

Zur Erlangung des akademischen Grades einer

DOKTORIN DER INGENIEURWISSENSCHAFTEN (Dr.-Ing.)

von der KIT-Fakultät für Chemieingenieurwesen und Verfahrenstechnik des

Karlsruher Instituts für Technologie (KIT)

genehmigte

DISSERTATION

von

Katarzyna Hofmann (geb. Pesta), M.Sc.

aus Olsztyn, Polen

Tag der mündlichen Prüfung: 20.05.2026

Erstgutachter: Prof. Dr. rer. nat. Norbert Willenbacher

Zweitgutachter: Prof. Dr. rer. nat. Helmut Ehrenberg

Preface

This publication-based dissertation consists of three peer-reviewed scientific journal articles. They include the main results of my experimental work from September 2020 until September 2024 at the Karlsruhe Institute of Technology (KIT), Institute of Mechanical Process Engineering and Mechanics (MVM) in the group of Applied Mechanics (AME).

This thesis includes an abstract, a theoretical introduction to lithium-ion batteries and disperse systems, as well as a motivation behind the aims of this work. The main part of this dissertation consists of the following publications:

1. Hofmann, K., Hegde, A. D., Liu-Theato, X., Gordon, R., Smith, A., Willenbacher, N. Effect of mechanical properties on processing behavior and electrochemical performance of aqueous processed graphite anodes for lithium-ion batteries. Journal of Power Sources 2024; 593: 233996.

2. Hofmann, K., Willenbacher, N. How carboxymethylcellulose adsorption and porous active material particles diminish the adhesion of graphite-silicon anodes in lithium-ion batteries. Energy Materials 2025; 5, 500092.

3. Hofmann, K., Smith, A., Willenbacher, N. Cross-Linked Acrylate Binder for High-Rate Graphite Anodes. Battery Energy 2025, e70054.

The thesis concludes with a summary and an outlook, as well as a joint bibliography. The bibliography includes all references of the publications. Hereby, the publications are slightly changed. Some diagrams and images are modified in size and color, taking into account the format of this dissertation.

Acknowledgements

This dissertation would not have been possible without the support of many people, whom I am deeply grateful to.

First and foremost, I would like to thank my supervisor, Prof. Dr. Norbert Willenbacher, for giving me the opportunity to do my doctorate under his guidance at the Institute of Mechanical Process Engineering and Mechanics (MVM) – Applied **e**Mechanics Group (AME). Norbert, thank you for the trust and support you have given me. I have learned a lot from you, not only in the field of scientific research but also through our inspiring conversations about culture, politics, travel, and many other topics, which have enriched me personally.

Special thanks go to Dr. Anna Smith, who enabled me to perform electrochemical measurements at Batterietechnikum (IAM-ESS). Anna, thank you for your professional guidance, for sharing your knowledge, and for your invaluable help at every stage of my research. I am also grateful to the entire Batterietechnikum Team, especially Sven Leuthner, Olivia Wiegand, as well as to Marcus Müller from Electrode Development Team at IAM-ESS, for their practical support in cell assembly and calendering of electrodes.

Furthermore, I would like to thank Ronald Gordon for his openness, the time he generously shared, and the many insightful scientific discussions that greatly deepened my understanding of the subject and helped shape the direction of my research.

An especially enriching experience was my research stay at Seoul National University in April/May 2024. I would like to thank CELEST for partially funding this visit, and Prof. Kyung Hyun Ahn and his doctoral students, especially Jinny, for their warm welcome into the research group and their kind support during my stay. This was an unforgettable period that will always remain in my memory.

I thank my colleagues at AME: Ophélie, Annika V., Jonas, Felipe, Kevin, David, Moritz, Wolf, Max, Katrin, Karim, Annika H., Karla, Bruna, Claude, Bo, Yiliang, Tillman, Marianne, Patrick, Selina, and Verena. Thank you for the great atmosphere at work, our discussions, and the time spent both at the Institute and beyond. Special thanks go to you, Ophélie, for your invaluable support, energy, and all the beautiful moments we shared together.

Thank you, Karsten, for your help and ideas regarding technical solutions in the laboratory. I would also like to thank Dr. Bernhard Hochstein for sharing his knowledge in the field of rheology, mechanics, and many other issues – I learned a lot from you.

Furthermore, I would like to thank the technical staff of the MVM, especially Klaus Hirsch, Astrid Huber, and Regina Mall, for their valuable technical support.

Many thanks to Volker Zibat from the Laboratory for Electron Microscopy (LEM) for the long hours of microstructure investigation.

I thank my students: Vanessa Zwinger, Akshay Hegde, Doménica Paz Puga, Christina Eichenseher, Thomas Textor, and Sofia Mayr for their support in the laboratory, motivation, and interest in my research topic.

My deepest gratitude goes to my family, who have always been, and continue to be, a constant source of love, support, and encouragement. I would especially like to thank my mother - Mamuś, bez Twojej miłości, wiary i nieustającego wsparcia nie byłoby możliwe osiągnięcie tego etapu. Dziękuję, że mimo dzielącego nas dystansu zawsze byłaś i jesteś blisko.

Special thanks go to my grandma Henia. Babciu, po latach Twojego cierpliwego i jakże motywującego pytania „*A dużo ci jeszcze zostało?*" mogę w końcu z radością i ulgą odpowiedzieć: "*Babciu, nareszcie skończyłam."*

Last but not least, Tim – Kochanie, thank you for your unconditional support, care, and belief in me, for your motivation, ideas, and perseverance. You are my strength, my love, my inspiration, and my greatest source of support.

Abstract

Due to anthropogenic causes, global warming has accelerated since the Industrial Revolution, leading to rising temperatures on land and in the oceans, the melting of glaciers, and rising sea levels. These changes contribute to more frequent and intense extreme weather events worldwide and have significant consequences for ecosystems and human societies. To limit the effects of global warming, the governments of 195 countries signed the Paris Agreement in 2015, committing to actions aimed at keeping the average global temperature rise well below 2 °C and pursuing efforts to limit it to 1.5 °C above pre-industrial levels. According to the latest scientific assessments, the Intergovernmental Panel on Climate Change (IPCC) indicates that achieving this target requires global carbon neutrality by around 2050. In response, many countries, including the European Union, have committed to achieving climate neutrality by 2050. The European Green Deal is the EU's plan to reach this goal by reducing emissions, promoting clean energy, and supporting sustainable growth. Achieving these ambitions will require a substantial shift away from fossil fuels, as well as immediate and significant reductions in emissions across all major economic sectors, including energy, transport, industry, construction, and agriculture. However, the transition to renewable energy requires reliable storage solutions, since its production is intermittent and depends on weather conditions. Among the available options, lithium-ion batteries (LIBs) are currently the most widely used and promising solution for meeting these needs.

Battery efficiency strongly depends on electrode engineering. While most research focuses on developing new active materials in order to improve the performance of LIBs, polymeric binders receive comparatively less attention. However, studies have shown that binders play a crucial role not only in slurry processing but also in overall cell performance. They affect particle distribution and interactions in slurries, thereby determining the final microstructure of the corresponding dry layers. As rheology modifiers, they enable a uniform coating process and are essential for electrode integrity by providing cohesion within the layer and adhesion to the current collector. While these functionalities influence electrochemical performance, the link between binder selection and desired electrochemical performance is not yet fully understood.

This thesis focuses on understanding the fundamental mechanisms controlling the functionality of polymeric binders, with the aim of developing a binder formulation concept yielding anodes for LIBs with improved electrochemical performance, including high rate capability, cyclic stability, and long battery lifetime. This approach does not rely on the synthesis of new polymers but instead employs tailored mixtures of well-established binders, thereby exploiting the capacity of the active material in waterborne slurry formulations prepared at a technical scale.

The role of styrene butadiene rubber (SBR) in aqueous-processed graphite anodes and its influence on mechanical properties, processability, and electrochemical behavior was systematically studied. To this end, graphite anodes with application-relevant mass loadings (5.7 and 10.1 mg cm^{-2}) were prepared with varying SBR contents and subjected to comprehensive mechanical and electrochemical testing to determine the optimal adhesion level that ensures failure-free processing without compromising the electrochemical performance. The addition of SBR not only exponentially increases the adhesion of the anode layer to the copper current collector but also leads to a linear increase in layer cohesion, which plays a key role in withstanding external stresses, particularly at higher mass loadings. However, it has been demonstrated that an excessive adhesion strength of anodes does not result in any significant advantages with regard to the anode's processability, as evidenced by the results of bending and winding tests. Cycling tests in full-cell pouch configuration revealed, contrary to expectations, that anodes without SBR and therefore with very low adhesive strength exhibit remarkable cycling stability. Furthermore, higher SBR concentrations and greater anode mass loadings lead to more severe degradation of electrochemical cell performance, primarily attributed to elevated internal resistance and SBR degradation.

The impact of carboxymethyl cellulose (CMC), originally incorporated into the formulation as a thickening and dispersing agent, on the adhesive strength between the electrode active layer and the current collector for the graphite and graphite/silicon composite anodes was investigated. In aqueous slurries, CMC adsorbs onto active material particles, and to determine this behavior for graphite, micro-silicon, and nano-silicon, a rheological approach was applied. In the absence of SBR, CMC alone does not provide substantial electrode adhesion. However, its adsorption onto active material particles indirectly affects the overall anode adhesion. The adsorbed CMC layer hinders the strong direct bonding of SBR to active material particles, thereby forming the weakest link between the active layer and the copper current collector. This effect is more pronounced with increasing CMC M_w due to enhanced adsorption. Furthermore, the microstructure of active material particles was found to have a strong impact on anode adhesion. SBR can diffuse into nano-silicon agglomerates and become trapped, resulting in very low adhesion for graphite–nano-silicon composite anodes despite minimal CMC adsorption on nano-silicon surfaces.

Based on these findings, a tailored binder system combining a commercially available, highly cross-linked acrylate binder (Carbopol® Ultrez10, x-PAA) with SBR was applied for graphite anodes. At reduced polymer content, x-PAA–based anode slurries maintain high-shear viscosities comparable to the CMC reference and exhibit a yield stress, which enhances slurry stability. Furthermore, SBR content could be lowered without compromising adhesion strength, since x-PAA does not adsorb onto graphite particles, as confirmed by ATR- FTIR spectroscopy. Consequently, the total binder content could be reduced by nearly 40 wt% in comparison to reference anodes comprising CMC. Under fast-charging conditions, cells with x-PAA anodes outperform those with CMC or linear polyacrylic acid (l-PAA) due to the absence of an adsorbed

polymer layer on the active material particles, which facilitates more efficient Li-ion insertion and extraction. However, a trade-off with long-term cycling stability must be considered, since the substantially lower binder content of x-PAA anodes reduces cohesion, leading to faster capacity fading during prolonged cycling compared with the CMC-based reference.

Zusammenfassung

Aufgrund anthropogener Ursachen hat sich die globale Erwärmung seit der industriellen Revolution beschleunigt. Dies hat zu steigenden Temperaturen an Land und in den Ozeanen, zum Abschmelzen der Gletscher und zum Anstieg des Meeresspiegels geführt. Diese Veränderungen tragen weltweit zu häufigeren und intensiveren Extremwetterereignissen bei und haben erhebliche Folgen für Ökosysteme und menschliche Gesellschaften. Um die Auswirkungen der globalen Erwärmung zu begrenzen, unterzeichneten die Regierungen von 195 Ländern im Jahr 2015 das Pariser Abkommen. Sie verpflichteten sich darin zu Maßnahmen, die darauf abzielen, den globalen Temperaturanstieg deutlich unter 2 °C zu halten und Anstrengungen zu unternehmen, um ihn auf 1,5 °C über dem vorindustriellen Niveau zu begrenzen. Laut den neuesten wissenschaftlichen Einschätzungen des Zwischenstaatlichen Ausschusses für Klimawandel (IPCC) ist zur Erreichung dieses Ziels eine globale CO_2-Neutralität bis etwa 2050 erforderlich. Als Reaktion darauf haben sich viele Länder, darunter die Europäische Union (EU), verpflichtet, bis 2050 klimaneutral zu sein. Der Europäische Grüne Deal ist der Plan der EU, um dieses Ziel durch Emissionsreduktionen, die Förderung sauberer Energie und die Unterstützung eines nachhaltigen Wachstums zu erreichen. Um diese ehrgeizigen Ziele zu realisieren, ist eine Abkehr von fossilen Brennstoffen sowie eine sofortige und deutliche Reduzierung der Emissionen in allen wichtigen Wirtschaftssektoren – darunter Energie, Verkehr, Industrie, Bauwesen und Landwirtschaft – erforderlich. Der Übergang zu erneuerbaren Energien erfordert jedoch zuverlässige Speicherlösungen, da deren Erzeugung fluktuierend ist und von den Wetterbedingungen abhängt. Unter den derzeit verfügbaren Optionen sind Lithium-Ionen-Batterien (LIBs) die am weitesten verbreitete und vielversprechendste Lösung, um diesen Anforderungen gerecht zu werden.

Die Effizienz von Batterien hängt stark vom Elektrodendesign ab. Während sich der Großteil der Forschungsarbeiten auf die Entwicklung neuer aktiver Materialien zur Verbesserung der Leistung von LIBs konzentriert, erhalten polymere Bindemittel vergleichsweise weniger Aufmerksamkeit. Studien haben jedoch gezeigt, dass Bindemittel nicht nur für die Slurry-Verarbeitung, sondern auch für die Gesamtleistung der Zelle eine entscheidende Rolle spielen. Sie beeinflussen die Partikelverteilung in den Slurries und die Mikrostruktur der getrockneten Elektrodenschichten. Als Rheologiemodifikatoren ermöglichen sie einen zuverlässigen Beschichtungsprozess und sind für die strukturelle Integrität der Elektrode unerlässlich, da sie den Zusammenhalt innerhalb der Schicht sowie die Haftung am Stromkollektor gewährleisten. Obwohl diese Funktionen die elektrochemische Leistung der Zelle beeinflussen, ist der Zusammenhang zwischen der Bindemittelauswahl und dem Erreichen der gewünschten elektrochemischen Eigenschaften noch nicht vollständig geklärt.

Diese Arbeit konzentriert sich auf das Verständnis der grundlegenden Mechanismen, die die Funktionalität polymerer Bindemittel bestimmen, mit dem Ziel, ein Konzept zur Bindemittelformulierung zu entwickeln, das Anoden für LIBs mit

verbesserten elektrochemischen Eigenschaften ermöglicht – darunter hoher Leistungsfähigkeit, Zyklenstabilität und verlängerter Lebensdauer. Dieser Ansatz basiert nicht auf der Synthese neuer Polymere, sondern auf maßgeschneiderten Mischungen bewährter Bindemittel. Dadurch wird die Kapazität des aktiven Materials in wasserbasierten Slurry-Formulierungen, die im technischen Maßstab hergestellt werden, besser genutzt.

Die Rolle von Styrol-Butadien-Kautschuk (SBR) in wasserbasierten Graphitanoden und dessen Einfluss auf mechanische Eigenschaften, Verarbeitbarkeit und elektrochemisches Verhalten wurde systematisch untersucht. Zu diesem Zweck wurden Graphitanoden mit anwendungsrelevanten Massenbeladungen (5,7 und 10,1 mg cm^{-2}) mit unterschiedlichen SBR-Gehalten hergestellt und umfassenden mechanischen und elektrochemischen Tests unterzogen, um das optimale Haftungsniveau zu ermitteln, das eine störungsfreie Verarbeitung ohne Beeinträchtigung der elektrochemischen Leistung gewährleistet. Die Zugabe von SBR erhöht nicht nur exponentiell die Haftung der Anodenschicht auf dem Kupferstromkollektor, sondern bewirkt auch eine lineare Zunahme der Schichtkohäsion, die eine wichtige Rolle für die Widerstandsfähigkeit gegenüber äußeren Belastungen spielt, insbesondere bei höheren Massenbeladungen. Es wurde jedoch gezeigt, dass eine übermäßige Adhäsion der Anoden keine signifikanten Vorteile für deren Verarbeitbarkeit bietet, wie Biege- und Wickeltests belegen. Elektrochemische Untersuchungen in Vollzellenkonfiguration zeigten zudem entgegen den Erwartungen, dass Anoden ohne SBR, und damit mit sehr geringer Adhäsion, eine bemerkenswerte Zyklenstabilität aufweisen. Darüber hinaus führen höhere SBR-Konzentrationen und größere Anodenmassenbeladungen zu einer verstärkten Verschlechterung der elektrochemischen Leistung, was primär auf einen erhöhten Innenwiderstand sowie auf die Degradation des SBR zurückzuführen ist.

Der Einfluss von Carboxymethylcellulose (CMC), die ursprünglich als Verdickungs- und Dispergiermittel in die Formulierung hinzugefügt wurde, auf die Haftfestigkeit zwischen der aktiven Elektrodenschicht und dem Stromkollektor von Graphit- sowie Graphit/Silizium-Anoden wurde untersucht. In wässrigen Slurries adsorbiert CMC an Partikeln des aktiven Materials. Zur Untersuchung dieses Verhaltens bei Graphit, Mikrosilizium und Nanosilizium wurde ein rheologischer Ansatz angewendet. Ohne SBR trägt CMC allein nicht zur Elektrodenadhäsion bei. Die Adsorption von CMC an Aktivmaterialpartikel beeinflusst jedoch indirekt die gesamte Anodenhaftung. Die adsorbierte CMC-Schicht behindert die direkte starke Bindung von SBR an Aktivmaterialpartikel und stellt somit die schwächste Verbindung zwischen der aktiven Schicht und dem Kupferstromkollektor dar. Dieser Effekt verstärkt sich mit zunehmendem M_w von CMC aufgrund der intensiveren Adsorption. Darüber hinaus wurde festgestellt, dass die Mikrostruktur der Aktivmaterialpartikel einen erheblichen Einfluss auf die Anodenadhäsion hat. SBR kann in Nanosilizium-Agglomerate diffundieren und dort eingeschlossen werden, was zu einer sehr geringen Haftung bei Graphit/Nanosilizium-Anoden führt, obwohl die CMC-Adsorption an Nanosiliziumoberflächen minimal ist.

Auf Grundlage dieser Erkenntnisse wurde für Graphitanoden ein maßgeschneidertes Bindemittelsystem eingesetzt, das ein handelsübliches hochvernetztes Acrylatbindemittel (Carbopol® Ultrez10, x-PAA) mit SBR kombiniert. Bei reduziertem Polymergehalt weisen x-PAA-basierte Anodenslurries eine hohe Scherviskosität auf, die mit der CMC-Referenz vergleichbar ist, und zeigen zudem eine Fließgrenze, welche die Slurry-Stabilität verbessert. Darüber hinaus konnte der SBR-Anteil ohne Beeinträchtigung der Haftfestigkeit verringert werden, da x-PAA nicht an Graphitpartikel adsorbiert, wie ATR-FTIR-Messungen bestätigen. Folglich ließ sich der Gesamtbindergehalt im Vergleich zu CMC-basierten Referenzelektroden um nahezu 40 wt% reduzieren. Unter Schnellladebedingungen übertreffen Zellen mit x-PAA-Elektroden diejenigen mit CMC oder linearem Polyacrylsäure (l-PAA), da keine adsorbierte Polymerschicht auf den Partikeln des Aktivmaterials vorhanden ist, was eine effizientere Li-Ionen-Ein- und -Auslagerung ermöglicht. Allerdings muss ein Kompromiss hinsichtlich der langfristigen Zyklenstabilität berücksichtigt werden, da der deutlich geringere Bindemittelgehalt von x-PAA-Anoden die Kohäsion verringert und im Vergleich zu CMC-basierten Referenzen zu einem schnelleren Kapazitätsverlust während verlängerten Zyklierens führt.

Notations

Abbreviations

AM	Active material
ATR-FTIR	Attenuated total reflection Fourier transform infrared spectroscopy
CA	Citric acid
CB	Carbon black
CC	Constant current
CCCV	Constant current – constant voltage
CMC	Carboxymethyl cellulose
C-rate	Current rate
CV	Constant voltage
DCIR	Direct current inner resistance
DEC	Diethyl carbonate
DMC	Dimethyl carbonate
DS	Degree of substitution
EC	Ethylene carbonate
ECH	Epichlorohydrin
GA	Guar arabic
GG	Guar gum
Gr	Graphite
ICE	Initial coulombic efficiency
LFP	Lithium-iron phosphate
LIB	Lithium-ion battery
LMO	Lithium-ion manganese oxide
l-PAA	Linear polyacrylic acid
M_w	Molecular weight
µ-Si	Micro-silicon
NMC	Lithium nickel manganese cobalt oxide ($LiNi_xMn_yCo_zO_2$)
NMP	N-methyl-2-pyrrolidone
NMR	Nuclear magnetic resonance
n-Si	Nano-silicon
OCV	Open-circuit voltage
PAA	Polyacrylic acid
PC	Propylene carbonate
PE	Polyethylene
PEI	Polyethyleneimide
PEO	Polyethylene oxide
PP	Polypropylene
PUU	Poly(urea-urethane)
PVA	Poly(vinyl alcohol)
PVDF	Polyvinylidene difluoride
SBR	Styrene butadiene rubber
SEI	Solid electrolyte interphase
SEM	Scanning electron microscopy
SOC	State of charge
TGA	Thermogravimetric analysis
VC	Vinylene carbonate
VdW	Van der Waals
x-PAA	Carbopol®Ultrez 10

Latin symbols

e	Elementary charge	[C]
A_H	Hamaker constant	[J]
a	Particle radius	[nm]
h	Interparticle distance	[nm]
F_{max}	Maximal uniaxial stress	[N]
A_0	Initial surface area	[cm^{-2}]
V_{solid}	Volume of solid phase	[cm^{-3}]
V_{liquid}	Volume of liquid phase	[cm^{-3}]
T	Temperature	[K]
T_g	Glass transition temperature	[°C]
k_B	Boltzmann constant	[J K^{-1}]
n_0	Number of ions in bulk phase	[m^{-3}]
Z_0	Ionic valency	[-]
x_s	Solid mass concentration	[wt%]
$x_{50,3}$	Volume-based average diameter	[nm]
v_{ads}	Specific volume of adsorbed polymer	[nm]
m_{AM}	Mass of active material	[g]
S_m	Specific surface area	[m^2 g^{-1}]
U	Voltage	[V]
R	Volume ratio of AM to CMC	[-]
t	Time	[s]

Greek symbols

σ_{max}	Maximum compressive strength	[N mm^{-2}]
φ_{solid}	Solid volume fraction	[vol%]
$\varphi_{CMC,0}$	CMC volume concentration before adsorption	[vol%]
φ_{CMC}	CMC volume concentration after adsorption	[vol%]
ψ_{vdW}	Van der Waals force	[N]
κ^{-1}	Debye length	[nm]
ε_r	Relative permittivity	[-]
ε_0	Permittivity of free space	[F m^{-1}]
η	Viscosity	[Pa s]
τ	Shear stress	[Pa]
τ_0	Yield stress	[Pa]
$\dot{\gamma}$	Shear rate	[s^{-1}]
ζ	Zeta potential	[mV]

Contents

1. Introduction

Climate change, due to the growth of global temperature, represents one of the most urgent challenges facing humanity today, affecting ecosystems, economies, and societies worldwide. In recent years, the effects of climate change have become increasingly noticeable, with natural disasters occurring more frequently and with greater intensity. 2024 was the warmest year on record, with the average air temperature 1.54 °C above the pre-industrial average (Figure 1.1) [1,2]. The Intergovernmental Panel on Climate Change (IPCC) attributes global warming primarily to excessive anthropogenic greenhouse gas emissions, with carbon dioxide (CO_2), methane (CH_4), and nitrous oxide (N_2O) identified as the most significant contributors [3]. These emissions result largely from unsustainable energy use, including the heavy reliance of global economies on fossil fuels. In 2023, compared to pre-industrial levels, methane emissions had increased by 165%, carbon dioxide emissions by 51%, and nitrous oxide by 24% [1].

In order to combat global climate change, various strategies aimed at reducing greenhouse gas emissions are being implemented by countries around the world. One major milestone was the Paris Agreement, adopted by 195 countries at the United Nations Climate Change Conference (COP21) in 2015. Its long-term goal (decades or longer) is to limit the rise in global temperature to well below 2 °C, and preferably to 1.5 °C, above pre-industrial level. Scientific assessments have shown that meeting this goal requires the world to achieve net-zero greenhouse gas emissions by around 2050. In response, the European Union (EU) introduced the European Green Deal and legally committed to becoming climate-neutral by 2050. This target now drives the EU's green transformation, reshaping energy systems, industry, transport, and agriculture, while promoting innovation and sustainable growth across the continent. During the COP28 conference in Dubai in 2023, an ambitious goal was set to triple the current renewable energy capacity (such as solar and wind power) and double energy efficiency by 2030. Achieving these goals requires the development of advanced energy storage technologies to balance the intermittent power supply. Among the available options, lithium-ion batteries (LIBs) are widely regarded as the leading candidate to meet these demands.

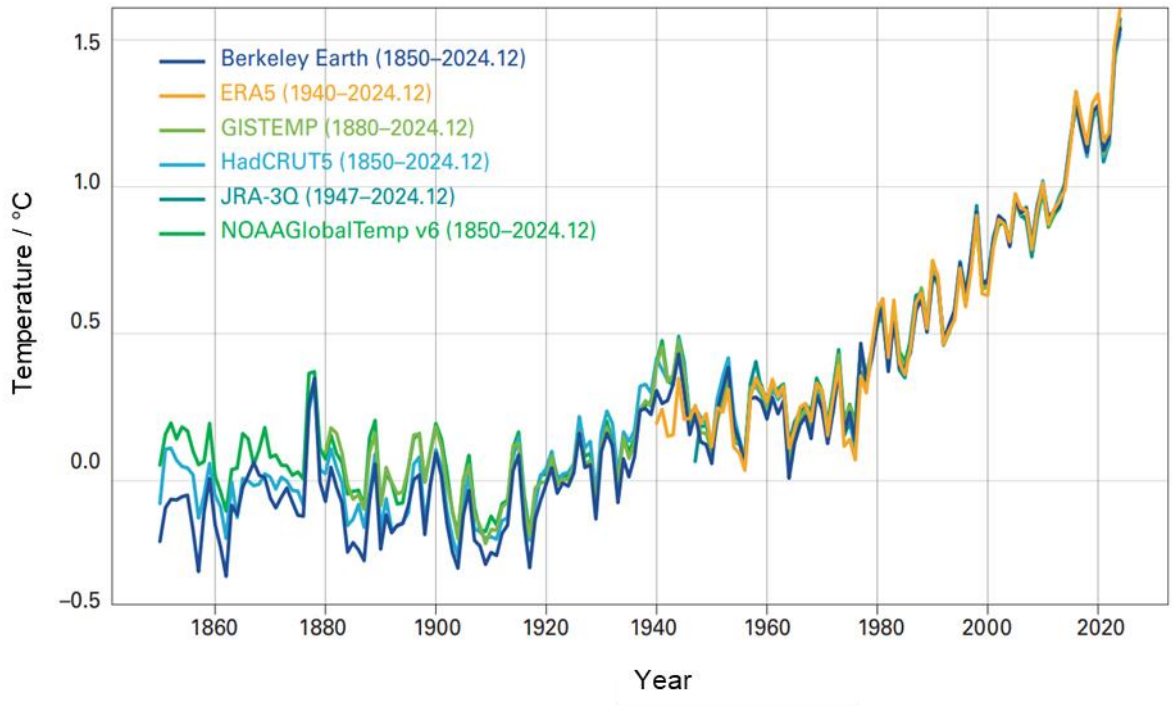

Figure 1.1. Annual global mean temperature anomalies relative to a pre-industrial (1850–1900) baseline shown from 1850 to 2024. Data are from six datasets indicated in the legend. Edited from [1].

Since their commercialization in 1991 by Sony, LIBs have revolutionized the world. They power almost everything — from consumer electronics to industrial, medical, and military systems. The wide use of LIBs can be largely attributed to their advantageous features, such as high energy density, long cycle life, low self-discharge, and modest maintenance requirements [4]. The first LIB consisted of a lithium cobalt positive electrode and a carbon-based negative electrode. Since that time, this technology has undergone substantial development and has emerged as one of the pillars of the green transition. Nevertheless, LIBs still face significant challenges, particularly in terms of safety, performance, production costs, reliance on critical raw materials, and recycling.

1.1. Fundamentals of lithium-ion batteries

1.1.1. Working principle and components of lithium-ion batteries

A LIB consists of a positive (cathode) and a negative (anode) electrode, separated by a porous membrane (separator) and immersed in an ion-conductive electrolyte (Figure 1.2). The positive electrode serves as a source of lithium ions, while the negative electrode acts as a host for lithium ions during charging. Each electrode comprises a metallic current collector, which enables electron flow between electrodes via an external circuit. The separator, however, protects against direct electrical contact between the two electrodes, thereby preventing a short circuit, while enabling lithium ions to pass through.

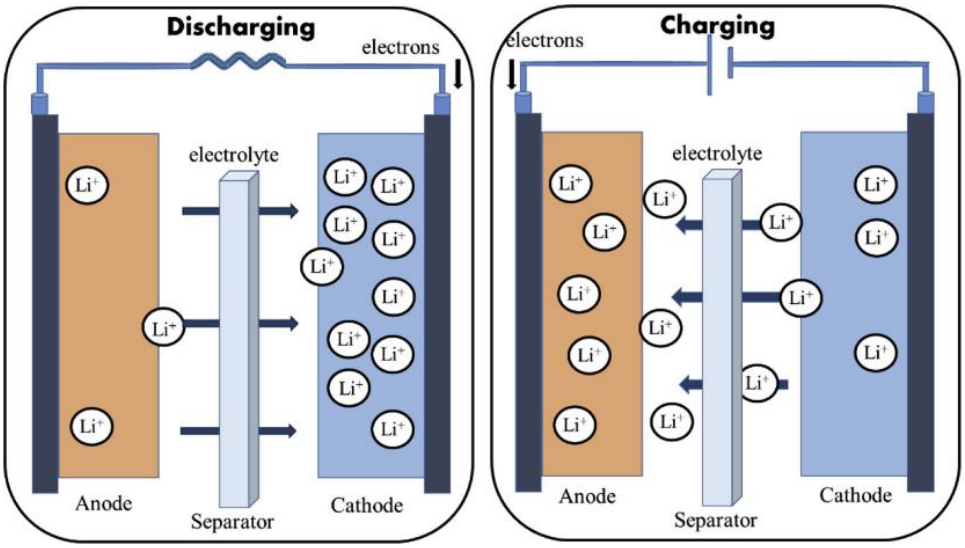

Figure 1.2. Schematic illustration of basic components and operation of a LIB [4].

In principle, a LIB converts chemical energy to electrical energy and vice versa. The basic working principles of LIBs are the same regardless of the electrode materials used. During charging and discharging cycles, lithium ions shuttle between two electrodes, which undergo redox reactions. During charging, when an external power source is connected, lithium ions are extracted from the cathode active material as it undergoes oxidation, releasing electrons according to the reaction:

$$\mathrm{LiMO_2} \rightarrow \mathrm{Li_{1-x}MO_2} + \mathrm{xLi^+} + \mathrm{xe^-}\,, \tag{1}$$

where MO_2 is a metal oxide. The lithium ions migrate through the electrolyte by diffusion and ionic conduction, passing through the separator to the anode. Simultaneously, electrons flow through the external circuit from the cathode to the anode, which undergoes reduction:

$$\mathrm{6C} + \mathrm{xLi^+} + \mathrm{xe^-} \rightarrow \mathrm{Li_xC_6}\,. \tag{2}$$

Lithium ions are incorporated into the anode active material as atomic lithium. During discharge, the redox reactions are reversed, and the flow of electrons through the external circuit generates an electric current that can power an external device. Solid-phase lithium atoms lose electrons and transform back into lithium ions, which are then released from the anode active material (oxidation reaction takes place). These lithium ions migrate to the cathode, which undergoes reduction. At the same time, to maintain charge balance, electrons flow through the external circuit in the opposite direction.

Electrodes are the heart of every battery. Each electrode consists of an electrochemically active layer coated onto a substrate foil, known as the current collector. As cathode active materials, intercalation compounds, such as transition metal oxides or polyanionic compounds, are typically used [5]. These materials can

also be classified by crystal structure, including layered $LiMO_2$ (M = Co, Ni, Mn, etc.), spinel LiM_2O_4 (M = Mn, etc.), and olivine $LiMPO_4$ (M = Fe, Mn, Ni, Co, etc.) compounds (Figure 1.3) [6].

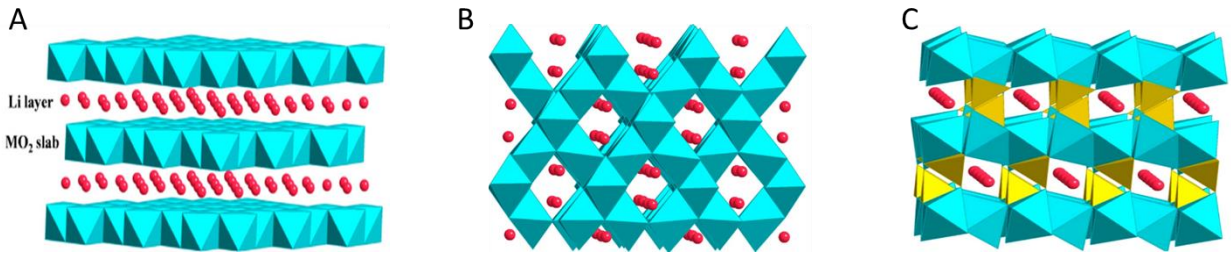

Figure 1.3. Schematic crystal structure of layered $LiMO_2$ (A), spinel LiM_2O_4 (B), and olivine $LiMPO_4$ (C) cathode materials. Blue: transition metal ions; red: Li-ions; yellow: P-ions. Edited from [6].

Many active materials lack sufficient electrical conductivity, so adding conductive additives to the electrode formulation is necessary. In commercial LIBs, various carbon-based materials, such as carbon black, carbon nanotubes, graphite powder, and graphene, are commonly used. Among these, carbon black is the most widely employed. It is a nano-sized powder with primary particles smaller than 100 nm, which tend to form aggregates around 200-300 nm and agglomerates up to several micrometers in size, held together by van der Waals attractive forces [7–9]. Although conductive additives are not classified as electrochemically active materials, they significantly influence the cell performance by lowering the internal cell resistance [10]. Once the amount of the conductive additive in the electrode reaches the critical volume fraction, the electrical conductivity increases sharply due to the formation of electrical pathways throughout the electrode [11–13]. This percolation threshold is lower for conductive additives with a higher aspect ratio [14]. However, excessive addition of conductive additive leads to the reverse effect: nano-sized carbon particles agglomerate, increasing the electrode´s resistivity [15]. Besides the amount, also the morphology, particle size, and surface area of conductive additives strongly affect both the electrochemical performance and electrode´s processing parameters, such as slurry viscosity, electrode porosity, or compressibility [16]. Qi et al. [17] reported that the conductivity of $LiFePO_4$ (LFP) cathodes reaches a maximum at an optimal specific surface area of the conductive additive. Beyond this value, further increases in surface area reduce electrode porosity and conductivity, thereby diminishing discharge rate performance.

Polymeric binders are key components of electrodes. They serve as a matrix in the formulation, holding all powders together and allowing coating on the substrate foil. They significantly influence dispersion properties, electrode microstructure, mechanical and electrical properties, as well as electrochemical behavior. Since

polymeric binders for anode formulations are the main focus of this work, their role is described in more detail in the next section (1.1.3).

The electrode active layer is coated onto a metallic substrate foil, which collects and distributes the electrons during charge and discharge cycles. These current collectors should not only be characterized by high conductivity but also by high mechanical strength, as well as chemical and electrochemical stability within the range of operating potential, which is 0-2 V and 3.5-4.5 V (vs. Li/Li^+) for anode and cathode, respectively. Due to these requirements, the most commonly employed current collector metals are aluminum (Al), with a standard redox potential of 1.37 V vs. Li/Li^+ [18], and copper, with a standard redox potential of 3.38 V vs. Li/Li^+ [18], serving as cathode and anode current collectors, respectively. The thickness of aluminum foils for LIBs typically ranges from 12 and 20 µm, whereas copper foils generally range from 8 to 18 µm. Both aluminum and copper are susceptible to electrochemical dissolution within the cathode operating potential window. However, in the case of aluminum, a passivation layer (Al_2O_3) is formed upon contact with Li salt-containing organic electrolytes. This protective layer suppresses aluminum dissolution within the potential range of 3.0-4.5 V, which coincides with the typical operating voltage of cathode materials [19].

The electrode pores and the space between electrodes are filled with an electrolyte, consisting of a lithium salt such as lithium hexafluorophosphate ($LiPF_6$) dissolved in a mixture of low-viscosity, conductive organic solvents (e.g., diethyl carbonate (DEC), dimethyl carbonate (DMC), ethylene carbonate (EC), or propylene carbonate (PC)). The electrolyte must meet several key criteria, including high chemical, electrochemical, and thermal stability – meaning resistance to side reactions with other cell components, a wide electrochemical stability window to avoid degradation, and stability across a broad temperature range [20]. Furthermore, the electrolyte should exhibit high ionic conductivity, typically in the range of 3×10^{-3} to 2×10^{-2} S cm^{-1} over a wide temperature range [21].

Between the cathode and anode, a separator is positioned to prevent direct contact between the electrodes and thereby avoid short circuits, while still permitting the transport of lithium ions. To enable ionic conduction, separators are typically designed with a porous structure. Commercial separators are most often fabricated from microporous polyolefins such as polyethylene (PE) and polypropylene (PP), with typical thicknesses below 25 µm and porosities of approximately 40 % [20,22]. The key properties of separators include thermal shrinkage resistance, wettability and electrolyte uptake, and mechanical strength. These parameters are critical to ensuring both the safety and the electrochemical performance of lithium-ion cells [22].

1.1.2. Anode active materials

The choice of active material for the anode plays a critical role for overall battery performance and durability. Based on their lithium storage mechanism anode active

materials can be classified into: intercalation-type (e.g., graphite), alloying-type (e.g., silicon, tin), and conversion-type (e.g., transition metal oxides) [23]. Each group offers unique advantages and faces specific challenges in terms of capacity, rate capability, cycle life, and safety.

Graphite

Graphite (Figure 1.4), representing the intercalation-type anode material, is currently the most used active material for negative electrodes in LIBs. Graphite consists of graphene layers, which are stacked on each other in hexagonal or, less commonly, in rhombohedral symmetry [24,25]. Carbon atoms in each layer are strongly bonded via sp^2 hybridized covalent bonds, and the layers are held together by weak van der Waals forces [26]. This results in anisotropy of graphite [24]. Along the basal plane (the surface parallel to the graphene layers), the electronic and thermal conductivities are significantly higher compared to the perpendicular direction (edge plane) [27]. Due to the presence of dangling bonds, functional groups, and defects, the edge sites of graphite demonstrate high electrochemical reactivity [26,28]. The reversible (de-)intercalation of lithium ions into the graphite structure during (dis-) charge cycles, following the equation:

$$Li_xC_n \underset{charge}{\overset{discharge}{\rightleftarrows}} xLi^+ + xe^- + C_n\,, \tag{3}$$

is possible only at edge (prismatic) sites or defective basal planes [25,29]. In the case of full lithiation, graphite reduces to LiC_6, which corresponds to the theoretical specific capacity of 372 mAh g^{-1} and volumetric capacity of 850 mAh cm^{-3}. During these processes, graphene layers undergo moderate volume changes, which for the full lithiation is about 10 % [30,31].

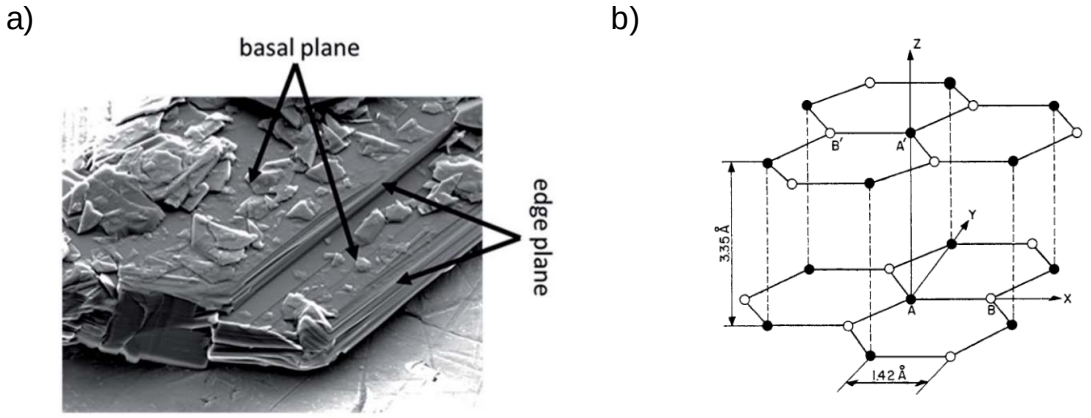

Figure 1.4. (a) SEM image of graphite particle with marked basal and edge (prismatic) plane [32]. (b) Schematic illustration of the layered graphite structure (hexagonal) - there are four atoms per hexagonal unit cell: A and A′ (full circles), B and B′ (open circles); the atoms A and A′ have neighbors directly above and below in adjacent layer planes; the atoms B and B′ have neighbors directly above and below in layer planes 6.71 Å away [24].

Despite their numerous advantages, graphite anodes suffer from limited rate capability during fast charging due to low lithiation kinetics. This can cause overpotential and lithium dendrite formation, increasing the risk of short-circuiting, accelerated aging, and capacity fading [32,33].

Silicon

Silicon represents an alloy-type anode material and is often utilized in its crystalline form. It is composed of a diamond cubic crystal structure (Figure 1.5) [34] and exhibits a maximal theoretical specific capacity of up to 4200 mAh g^{-1} (for $Li_{4.4}Si$), which is more than ten times higher than that of graphite. In addition, silicon has a slightly higher working potential (~ 0.37 V vs Li/Li^+), which reduces the risk of lithium plating and thus enhances battery safety [4,33,35]. However, silicon has some drawbacks, which make the practical implementation challenging. It exhibits poor electronic conductivity (≈ 10^{-3} S cm^{-1}) [36] and slow lithium diffusion (10^{-14}–10^{-13} cm^2s^{-1}) [37], which deteriorates the rate performance of silicon anodes.

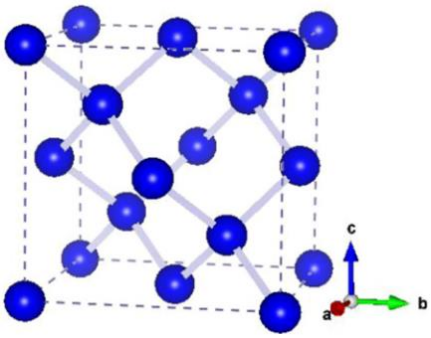

Figure 1.5. The diamond cubic crystal structure of silicon [34].

During the lithiation and delithiation processes, silicon undergoes phase transitions and alloying reactions, leading to significant structural changes and a large volume expansion of about 300 % [5,38,39]. Repeated expansion and contraction of the silicon active material during cycling causes particle fracture and pulverization, leading to delamination from the current collector and subsequent electrical isolation. Additionally, continuous particle expansion during lithiation fractures the solid electrolyte interphase (SEI) layer, exposing new surfaces to irreversible side reactions with the electrolyte and promoting new SEI formation. Both phenomena contribute to rapid capacity fading over repeated cycles [4,34,40,41]. To address these challenges, several approaches have been proposed, including the use of nano-sized silicon (e.g., nanoparticles [42,43], nanowires [44,45], nanotubes [46,47]) to accommodate volume changes and reduce particle fraction. Furthermore, strategies such as carbon coatings [48,49], encapsulation [50,51], or nanosheets [52,53] have been employed to shield silicon particles from direct contact with the electrolyte.

1.1.3. Polymeric binders in anode design

Polymeric binders are electrochemically inactive components that typically account for about 5 wt% of the electrode formulation. Despite their small fraction, they fulfill multiple critical functions. As dispersing agents, binders enable the preparation of homogeneous, aggregate-free slurries, thereby influencing the electrode microstructure and, in turn, its electrical properties. They also serve as rheology modifiers, affecting slurry stability and allowing adjustment of flow behavior, which is essential for reliable coating during electrode fabrication. In addition, binders determine key mechanical properties: they provide cohesion within the electrode layer, preventing crack formation during processing and cycling, and provide strong adhesion between the electrode layer and the current collector, ensuring good processability and avoiding delamination during cell operation. Overall, these functions of polymeric binders have a decisive impact on the electrochemical performance of lithium-ion batteries.

Polymeric binders are required to meet several criteria in order to ensure reliable electrode processing and long-term electrochemical performance [54]:

- high flexibility and adhesion to the current collector and active material,
- sufficient ionic and electronic conductivity,
- high thermal, chemical, and electrochemical stability,
- low swelling and insolubility in the electrolyte,
- strong dispersive capability, enabling homogeneous distribution of electrode components,
- high efficiency, meeting these requirements at minimal binder concentrations.

Depending on the solvent used in wet electrode processing, binders can be classified into those compatible with organic solvents and those suitable for water-based slurries. In the first category, the most widely used material is polyvinylidene fluoride (PVDF) (Figure 1.6 A), which is primarily employed in cathodes. PVDF is valued for its excellent chemical and electrochemical stability; however, it also exhibits several significant drawbacks. It is electrically insulating and prone to swelling and soluble in the electrolyte, which can ultimately result in cell capacity loss. An additional major limitation is its reliance on the toxic organic solvent *N*-methyl-2-pyrrolidone (NMP), which is environmentally hazardous, flammable, and costly [55,56].

The most commonly employed water-based polymeric binder is sodium carboxymethyl cellulose (CMC) (Figure 1.6 B), an anionic polyelectrolyte derived from cellulose. Its structure consists of β-glucopyranose monomers in which a fraction of the hydroxyl groups is substituted by carboxymethyl groups, thereby conferring water solubility. The average number of substituted hydroxyl groups per glucose unit, defined as the degree of substitution (DS), typically ranges from 0.6 to 1.2. A lower DS results in a more hydrophobic CMC and, consequently, a less extended conformation of the polymer chains in water. CMC molecules are capable of forming intermolecular hydrogen bonds, which can promote aggregation in solution. In anode slurries, CMC functions both as a dispersing agent and as a rheology modifier. By adsorbing onto the

active material surface, it stabilizes the particles in aqueous media. More hydrophobic CMC exhibits stronger adsorption on graphite, driven by preferential interactions with its basal planes [57]. For silicon, adsorption takes place via hydrogen or covalent bonding, depending on pH, between carboxylate groups of CMC and silanol groups on the silicon surface [58–61]. The influence of CMC DS, molecular weight (M_w), and concentration on slurry rheology, particle dispersion, and electrode microstructure has been investigated in several studies [62–65]. At both low and high CMC concentrations, gel-like structures are formed, either through hydrophobic attraction between graphite particles or through polymer network formation, respectively [66]. Furthermore, due to partial CMC adsorption onto graphite, the relative high-shear viscosity of graphite slurries decreases with increasing CMC M_w [62]. In addition to these effects, CMC also influences the mechanical integrity of anodes. Gordon et al. [62] demonstrated that in flake-like graphite slurries, a higher CMC molecular weight promotes alignment of particles parallel to the current collector, thereby enhancing the cohesive strength of the electrode layer. However, due to its high glass transition temperature (T_g > 100 °C), CMC exhibits a brittle nature and cannot impart sufficient flexibility to the electrode layer. Consequently, the addition of a rubber latex is required to ensure high adhesive strength between the electrode layer and the current collector foil.

Styrene-butadiene rubber (SBR) (Figure 1.6 C) is synthesized via copolymerization of styrene and 1,3-butadiene. The resulting properties are determined by several structural and processing parameters, including styrene content, cross-link density, emulsifier type, and polymerization conditions [67]. In lithium-ion battery anodes, SBR is employed as an aqueous dispersion of nanoscale polymer particles, serving as an adhesion promoter without altering slurry rheology [62].

Another widely used polymeric binder, particularly for silicon anodes, is polyacrylic acid (PAA) (Figure 1.6 D). Like CMC, PAA contains carboxyl groups, however, their density is considerably higher. This results in a greater number of contact points between PAA and the hydrophilic silicon surface, which is advantageous for accommodating the substantial volume expansion of silicon during cycling. Nevertheless, the linear form of PAA exhibits low viscosity and is therefore an ineffective rheology modifier for anodes. To overcome this limitation, a variety of PAA-based copolymers have been developed in recent years, offering multifunctional properties, including improved ionic and electronic conductivity. These copolymers are commonly synthesized by grafting or cross-linking PAA with other polymers, e.g., CMC [68], poly(vinyl alcohol) (PVA) [69], or sodium alginate [70].

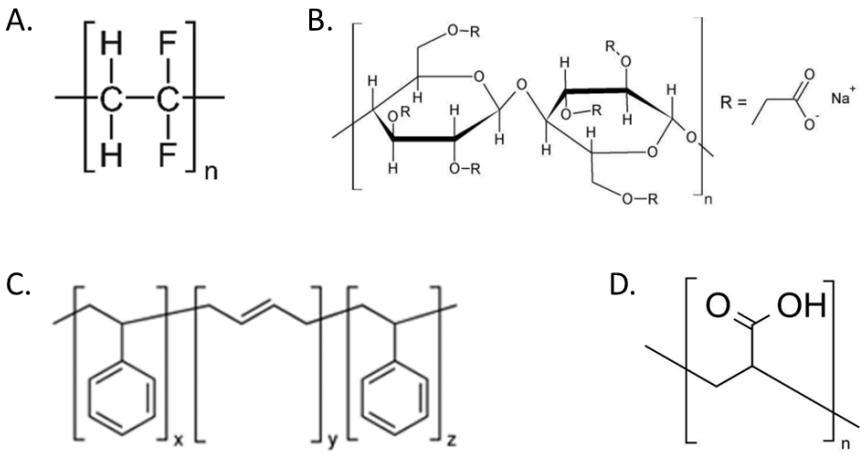

Figure 1.6. Structure formula of (A.) polyvinylidene fluoride, (B.) sodium carboxymethyl cellulose, (C.) styrene-butadiene rubber, and (D.) linear polyacrylic acid.

1.1.4. Cell manufacturing

Even though the electrochemical performance of lithium-ion batteries depends strongly on the type and quality of the individual electrode and cell components, the production steps, processing methods, and parameter settings play an equally critical role, determining not only the manufacturing costs and production throughput but also the properties of the final cell. Regardless of the cell format (pouch, prismatic, or cylindrical), the manufacturing steps are largely similar. They can generally be divided into three main stages: electrode preparation, cell assembly, and cell finishing (Figure 1.7).

The mixing step plays a decisive role in defining the electrode microstructure and, consequently, its mechanical, electrical, and electrochemical properties. Electrode preparation is conventionally carried out using wet processing. Typically, the binder is first dissolved in the solvent before the dry mixture of active materials and conductive additives is incorporated and dispersed to form a homogeneous slurry. In many cases, a pre-mixing step of the dry components is also included in the mixing procedure. Aqueous processing is typically employed for anodes, whereas cathode fabrication conventionally still relies on organic solvents such as *N*-methyl-2-pyrrolidone (NMP). Slurry mixing is most commonly performed in a batch process using a planetary mixer, although continuous extrusion has gained increasing attention in recent years [71–74]. As a final step, the slurry is degassed and agglomerates are filtered out to prevent defects during coating.

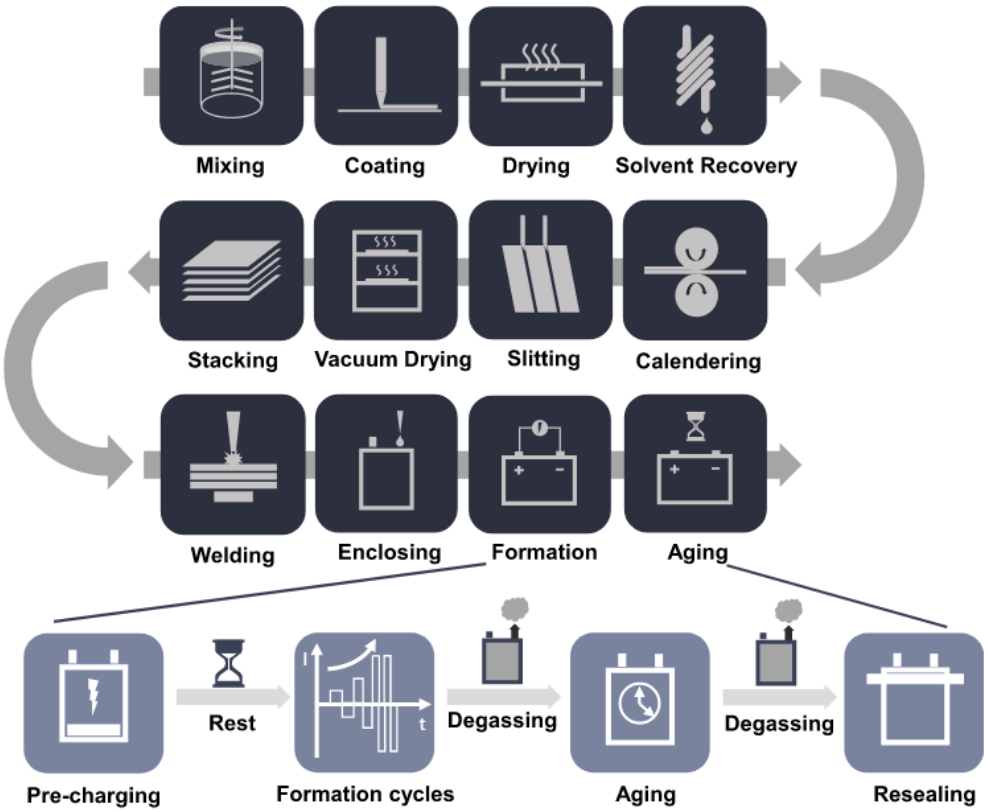

Figure 1.7. Schematic of manufacturing steps of LIBs [71].

Subsequently, the slurry is coated onto the current collector foil using slot-die coating and then dried. Optimizing the drying conditions is crucial, as inappropriate drying may lead to segregation of the electrode components, resulting in non-uniform material distribution and altered electrode microstructure, which significantly deteriorates the mechanical properties of the electrode and, in turn, impairs its electrochemical performance [75–79]. For cathode manufacturing, the use of NMP necessitates solvent recovery due to its cost and toxicity, making the drying and recovery steps the most energy-intensive stages of production, accounting for almost 50 % of total energy consumption [71]. Consequently, dry coating has emerged as a promising alternative, offering significant reductions in energy consumption and environmental impact [80,81]. This technology has already been commercialized in certain applications, demonstrating its industrial feasibility.

After electrode drying, a compression step known as calendering is applied. In this process, the electrode is guided between two rotating rollers and compacted. As a result, the electrode microstructure changes: the porosity decreases, and more contact points between electrode components are formed. This improves the mechanical as well as electrical properties and increases the volumetric energy density of the electrode [82]. However, the trade-off between ionic and electronic conductivity must be taken into account when selecting the optimal electrode porosity, and thus the appropriate degree of compression. In general, higher electrode porosity enhances effective ionic conductivity because the increased electrolyte-filled void space

facilitates Li^+ transport. Nevertheless, high porosity alone does not guarantee low ionic resistance. If the pore network is poor (high tortuosity), ionic transport is hindered. Increased compression improves electronic conductivity, which is particularly critical for cathodes. On the other hand, too strong compression may elevate ionic resistance due to increased tortuosity and can also induce cracking of active material particles, which in turn may negatively affect the electrochemical performance of the cell [83]. After, or sometimes before, the calendering step, the electrode coil is slit into smaller rolls. Prior to cell assembly, the slitted coils are dried under vacuum to minimize residual moisture entering the cell.

Three main cell formats are commonly used in automotive applications: pouch, cylindrical, and prismatic (Figure 1.8). In pouch cell assembly, the process begins with unwinding the electrode coils, followed by punching the electrodes to the desired shape. The separated electrode sheets are then stacked, typically using a Z-folding process [84], in which electrodes are inserted between a continuously running separator folded in a zigzag pattern. These stacks are then sealed within an aluminum pouch. For cylindrical cells, the electrodes and separators are wound into a specific sequence (separator-anode-separator-cathode) around a central pin, forming a jelly roll, which is then placed into a cylindrical housing [84]. Prismatic cells employ a similar electrode–separator configuration to cylindrical cells, however, instead of being wound, the layers are folded and stacked before being enclosed in a rigid rectangular casing [85].

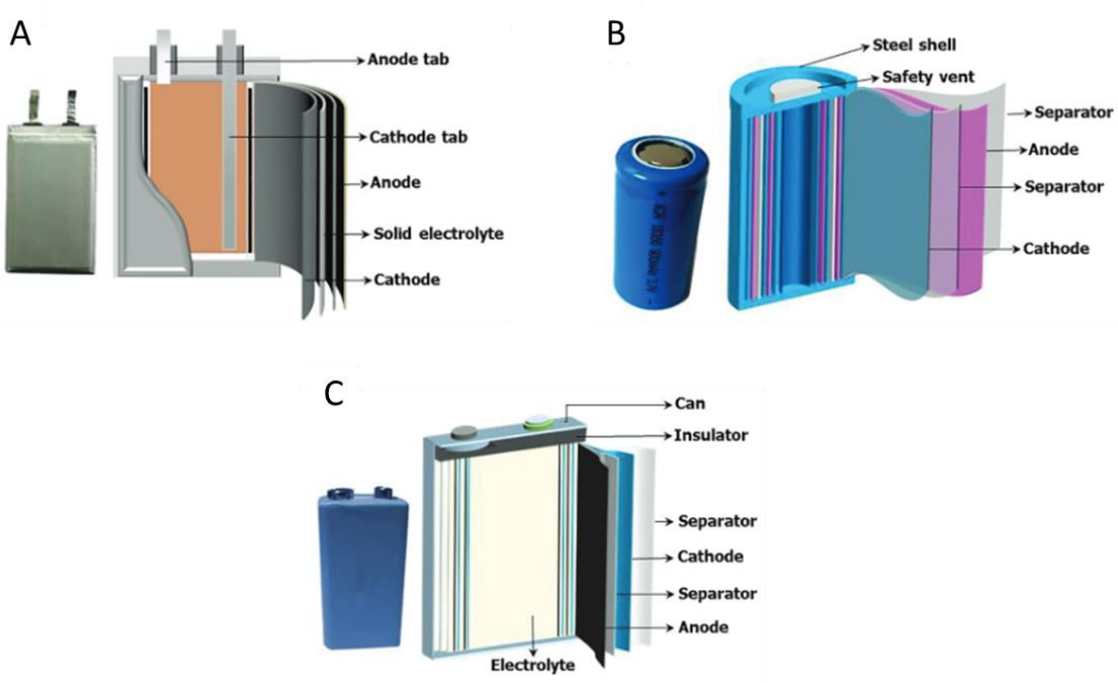

Figure 1.8. Schematic illustration of different cell formats: (A) pouch cell, (B) cylindrical cell and (C) prismatic cell. Edited from [86].

Subsequently, the current collector foils are connected to the cell tabs, usually via laser or ultrasonic welding, and the stacks or jelly rolls are inserted into the cell housing. Pouch cells are enclosed in multilayer aluminum composite foils, whereas cylindrical and prismatic cells typically use metal housings. Electrolyte is then filled under extremely dry conditions (dew point < −60 °C) [72], and the housing is sealed.

The final step of manufacturing is cell finishing. Initially, formation is performed, lasting up to 24 hours, during which the first charge–discharge cycles occur and the solid electrolyte interphase (SEI) is formed. During formation, the C-rate is gradually increased over successive cycles to reduce formation time and associated costs. After formation, cells are stored on aging shelves, and key quality parameters, such as capacity, internal resistance, and self-discharge rate, are monitored over a period of up to three weeks [72,84].

1.1.5. Electrochemical cell performance evaluation

The key characteristic of LIBs is the open-circuit voltage (OCV), representing the potential difference between anode and cathode when no current flows and the electrode potentials are at equilibrium [87]. This potential difference depends on the lithium concentration in the active material. Since the theoretical calculation of the OCV is complex and not feasible for all electrode materials, it is generally determined experimentally. While the OCV curve describes the equilibrium state of the battery, practical operation always involves current flow or relaxation processes. This leads to deviations from OCV, which become visible in the discharge characteristics.

Under the load, the system is driven out of thermodynamic equilibrium, and the cell voltage deviates from the OCV. This deviation, referred to as overvoltage or polarization, reflects the combined influence of three contributions: ohmic polarization, kinetic polarization, and mass-transfer polarization. Together, these effects shift the discharge curve downward relative to the OCV (Figure 1.9). Ohmic polarization originates from electronic resistance in the electrodes and ionic resistance in the electrolyte and separator. Kinetic polarization arises from the finite charge-transfer rate of the electrochemical reactions at the electrode–electrolyte interfaces. Mass-transfer polarization is associated with concentration gradients in the electrolyte and within active material particles that develop due to limited lithium diffusion.

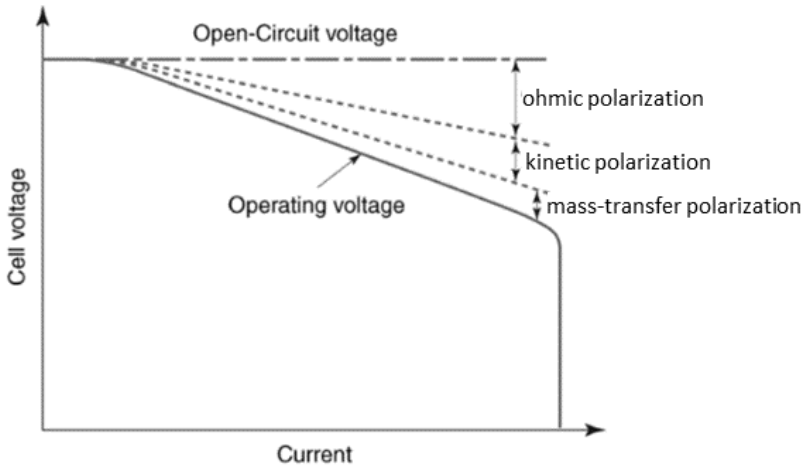

Figure 1.9. Effect of current density on polarization. Edited from [88].

At high current densities, these polarization effects become increasingly pronounced, leading to earlier voltage cutoff and an apparent loss of accessible capacity. During galvanostatic charging or discharging of lithium-ion batteries, the applied current is typically expressed in terms of the C-rate. A rate of 1C corresponds to a current that would fully (dis)charge the nominal capacity of a cell within one hour. For example, a battery with a nominal capacity of 1.5 Ah has a 1C rate of 1.5 A, discharging the cell in one hour, while a 5C rate corresponds to 7.5 A and a discharge time of 12 minutes.

Charging procedures

The most commonly applied charging protocol for LIBs is the constant-current–constant-voltage (CCCV) method (Figure 1.10). During the constant-current (CC) phase, the cell is charged at a fixed current while the voltage rises until it reaches the upper cut-off value. Subsequently, the protocol switches to the constant-voltage (CV) phase, in which the voltage is maintained at this limit while the current gradually decreases toward a predefined lower threshold (cut-off current). Although the decreasing current in the CV phase extends the overall charging time compared to constant-current-only charging, maintaining the cell voltage at a fixed value effectively prevents overcharging and reduces the risk of degradation phenomena such as lithium plating [89].

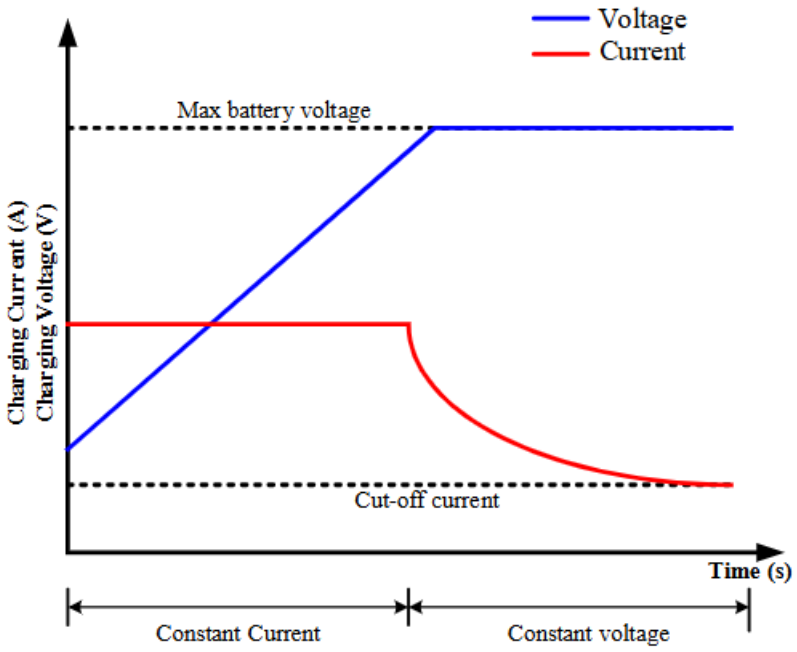

Figure 1.10. Exemplary constant-current constant-voltage (CCCV) charging profile [90].

Rate capability test

Since discharge characteristics are strongly dependent on the applied current, the rate capability test is commonly employed to systematically evaluate cell performance at different C-rates. From an electrochemical perspective, rate capability describes the ability of a cell to deliver a defined specific capacity (e.g., in mAh g^{-1}) within a prescribed voltage window when operated at increasing current densities [91]. The test, therefore, provides insight into how much of the theoretical capacity remains accessible as transport and kinetic limitations become more pronounced at higher rates. The results are typically presented as rate capability plots, in which the discharge (or charge) capacity is plotted as a function of C-rate (Figure 1.11).

Practical requirements for rate capability vary depending on the application: consumer electronics typically operate at around 1C, while power tools demand currents above 10C, battery electric vehicles reach up to about 10C, and hybrid electric vehicles may require rates of 40C or higher [88]. The achievable rate capability is closely linked to cell design and materials selection. It is influenced by factors such as electrolyte conductivity, separator properties, active material type, particle size, electrode porosity, and microstructure. Among these, electrode thickness plays a particularly critical role: thinner electrodes generally enable higher rate capability because ionic and electronic transport resistances are reduced, allowing faster charge and discharge without severe polarization.

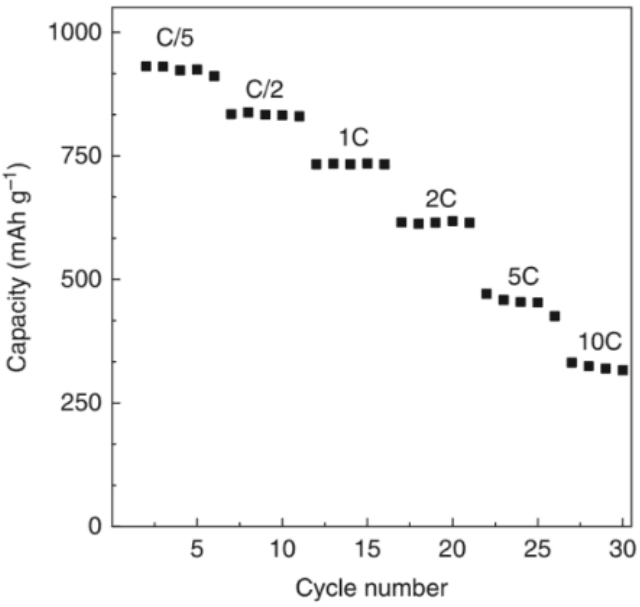

Figure 1.11. Rate capability plot of a Fe_2O_3 vs. Li cell cycled at C-rate values between C/5 and 10C [92].

Long-term cycling and aging

Long-term cycling tests are employed to evaluate the durability of lithium-ion batteries under repeated charge–discharge operation. In these experiments, the cell is cycled at defined current rates and voltage windows until a significant fraction of its initial capacity is lost (commonly, 80 % capacity retention is considered as a threshold). The evolution of discharge capacity, coulombic efficiency, and internal resistance over many cycles provides quantitative insight into the degradation processes that govern battery lifetime. Performance degradation during prolonged cycling is primarily associated with a gradual increase in internal resistance and a loss of active material. These changes originate from interfacial side reactions that continuously consume active lithium and electrolyte, structural and mechanical deterioration of the active materials, and the growth of contact resistance within the electrodes [88]. As a result, both the cycle life and the rate capability of the battery are progressively reduced.

The dominant aging mechanisms during long-term cycling often originate at the anode. These include continuous solid–electrolyte interphase (SEI) growth driven by electrolyte decomposition, as well as lithium deposition in the form of homogeneous plating or localized accumulation. Deposited lithium may further react with the electrolyte or may loose electric contact, thereby accelerating capacity fade though loss of active lithium inventory [93]. Additional degradation pathways arise through crosstalk phenomena. E.g. transition metals such as Mn, Ni, Co, or Fe can dissolve from the cathode and migrate to the anode, where they catalyze parasitic reactions and destabilize the SEI [94]. Mechanical deterioration, such as electrode delamination, adhesion loss, and particle cracking, further contributes to performance decay. Gas

evolution within the electrolyte can cause pouch cells to swell or lead to internal pressure build-up in rigid housing designs.

1.1.6. Mechanical properties of electrodes

The mechanical behavior of LIB electrodes is largely governed by adhesion and cohesion. Adhesion describes the bonding between the active electrode layer and the current collector, while cohesion refers to the internal integrity of the electrode layer itself. Both are strongly influenced by the binder system, as well as by electrode microstructure, porosity, and thickness.

Adhesion is a complex interfacial phenomenon describing the attachment of an adherent to a substrate, arising from multiple underlying mechanisms. Several mechanisms have been proposed to explain adhesion, three of which are particularly relevant for lithium-ion battery electrodes: physical adsorption, chemical bonding, and mechanical interlocking. Physical adsorption is based on van der Waals forces and is always present, as all adhesive interactions require molecules to be in intimate contact. Chemical bonding involves the formation of covalent, hydrogen, or ionic bonds across the substrate–adhesive interface. Mechanical interlocking occurs when an adhesive penetrates a surface roughness of the substrate, enhancing adhesion through structural anchoring. [95] Finally, also the viscoelastic deformation and flow of soft polymers above their glass transition temperature, such as SBR, strongly contributes to the adhesive strength between electrode layer and current collector [96].

Adhesive strength is commonly measured using a peel test, in which one surface is fixed while the other is peeled off at a constant angle and velocity. Ideally, failure occurs at the adhesive-substrate interface (adhesive failure), however, fracture can also occur within the adhesive layer or the adherent itself (Figure 1.12). The energy required to separate two surfaces is referred to as the adhesive fracture energy, which depends on several parameters, such as temperature and (for viscoelastic materials) test rate.

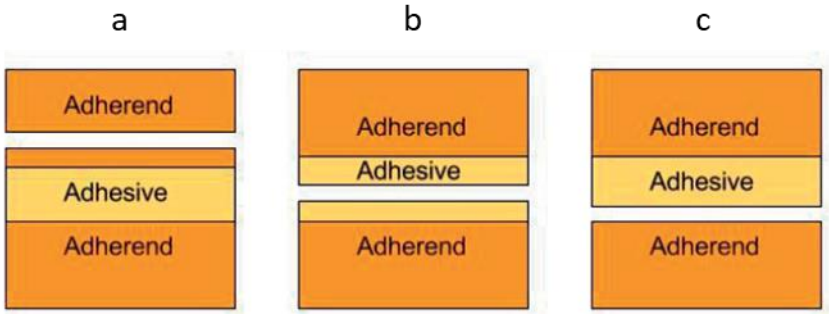

Figure 1.12. Failure modes during peel-test: (a) cohesive failure in adherent, (b) cohesive failure in adhesive, (c) adhesive failure. Edited from [97].

Cohesion refers to the internal forces that hold together the components of a material. In porous electrode layers, cohesion originates from interparticle contacts and the polymer binder network, which together provide internal strength. Cohesion can be evaluated by a compression test [62], where a specimen of defined geometry is compressed between two parallel plates at a constant velocity. The resulting compressive strength σ_{max} is defined as the maximal uniaxial stress F_{max} reached when the material fails, normalized to the initial sample cross-sectional area A_0:

$$\sigma_{max} = \frac{F_{max}}{A_0}. \tag{4}$$

Both adequate cohesive strength within the electrode layer and adhesive strength between the active layer and the current collector is essential to maintain the structural integrity of the electrode, preventing particle detachment, cracking, or disintegration during fabrication and electrochemical cycling.

1.2. Disperse systems

A dispersion is a mixture of at least two immiscible components, consisting of a continuous phase in which a second phase (dispersed phase) is distributed. Depending on the physical state of the phases and the size of the dispersed entities, dispersions can be divided into suspensions (solid particles in liquids), emulsions (liquid droplets in liquids), foams (gas in liquids or solids), and aerosols (solid or liquid particles in gases). In terms of particle size, one distinguishes molecularly dispersed systems (< 1 nm, true solutions), colloidal dispersions (1 nm–1 µm), and coarse dispersions (> 1 µm) [98]. Lithium-ion battery slurries can be classified as multicomponent suspensions, as the dispersed phase comprises particles spanning a broad size range, from nanometer-sized conductive additives to active material particles with dimensions of several tens of micrometers. Consequently, LIB slurries can be regarded as suspensions that combine the characteristics of both colloidal and coarse dispersions, depending on the particle size of the individual components. The properties of the dispersed phase largely dictate the characteristics of a dispersion. In the case of suspensions, the most relevant parameters include the average particle size, particle size distribution, particle shape, surface roughness of the dispersed particles, as well as solid volume fraction φ_{solid} defined as:

$$\varphi_{solid} = \frac{V_{solid}}{V_{solid} + V_{liquid}}, \tag{5}$$

where V_{solid} and V_{liquid} are volumes of solid and liquid phases, respectively [98].

1.2.1. Interparticle interactions

In colloidal suspensions, particles are subjected to a variety of interparticle forces, including attractive van der Waals interactions, electrostatic repulsion, steric repulsion, and, in certain cases, attractive depletion forces.

Van der Waals forces arise from dipole or induced-dipole interactions at the atomic level. The van der Waals forces include Keesom interactions (permanent dipole/permanent dipole interactions), Debye interactions (permanent dipole/induced dipole interactions), and London interactions (induced dipole/induced dipole interactions). Among them, London forces are always present, as they do not require the existence of permanent polarity or charge-induced polarity in molecules [99]. Van der Waals forces are relatively long-ranged compared to other atomic or molecular level forces, with an effective range of approximately 0.2 nm to over 10 nm. For two equally large sphere particles of radius *a*, at very short distances of separation ($h \ll a$), the van der Waals attraction can be approximated as:

$$\psi_{vdW} = -\frac{A_H a}{12h}, \tag{6}$$

where A_H is the Hamaker constant.

Electrostatic repulsion in colloidal suspensions arises from the surface charge of particles, which can result from dissociation of surface groups or adsorption of ionic species such as surfactants. The charged particles are surrounded by a cloud of counter-ions, forming the so-called electric double layer. The electrostatic potential decreases linearly from the particle surface ψ_0 to a value ψ_d at the outer edge of the double layer (also called Stern layer) and then decays $\sim\frac{1}{r}exp(-\kappa r)$, approaching zero in the bulk solution. The range of the electrostatic repulsion is characterized by the so-called Debye length κ^{-1}, which is given by:

$$\frac{1}{\kappa} = \left(\frac{\varepsilon_r \varepsilon_0 k_B T}{2 n_0 Z^2 e^2}\right)^{\frac{1}{2}}, \tag{7}$$

where ε_r is the relative permittivity, ε_0 the permittivity of free space, k_B the Boltzmann constant, *T* the absolute temperature, n_0 the number of ions in the bulk phase, *Z* the ionic valency, and *e* the elementary charge. When two particles approach such that their double layers begin to overlap, repulsion mainly arises due to the osmotic pressure emerging from the surplus of counterions in the overlap region and in second order also to the energetic cost of compressing the counter-ion clouds [100].

Depletion attraction can occur when non-adsorbing polymers are present in a dispersion. The polymers are excluded from a layer of thickness Δ around each particle (corresponding to their radius of gyration). This reduces the entropy of the system,

which in turn increases when the particles approach each other closer than 2Δ their excluded volume layers overlap. Then the non-adsorbing polymers gain more space for diffusional motion and the entropy of the system increases, i.e. the free energy decreases [101]. This depletion phenomenon thus acts as an attractive force its strength is proportional to the concentration of the non-adsorbing polymer and the range is given by its radius of gyration.

1.2.2. Polymer adsorption

Two essential requirements of an electrode slurry are stability and good processability. From a thermodynamic perspective, dispersions are inherently unstable, since the high surface area of dispersed particles is associated with excess surface energy, creating a driving force for aggregation. Thus, in the absence of long-range repulsive forces, attractive interactions dominate and particles tend to agglomerate. This can be mitigated by the adsorption of a stabilizing layer, typically composed of polymers or surfactants, which counteracts attractive forces and improves dispersion stability.

Polymers dissolved in the continuous phase can interact with solid interfaces and adsorb at the particle–liquid boundary. The driving force for polymer adsorption is the higher affinity of polymer segments for the particle surface compared with that of solvent molecules. Adsorption occurs when the enthalpic gain per monomer surface contact exceeds the loss of configurational entropy, i.e., when the adsorption energy per monomer is greater than k_BT. In a good solvent, saturation of particle surfaces with adsorbed polymer results in the formation of dense interfacial layers. When particles approach closely, these layers overlap, generating steric repulsion that kinetically stabilizes the dispersion (Figure 1.13).

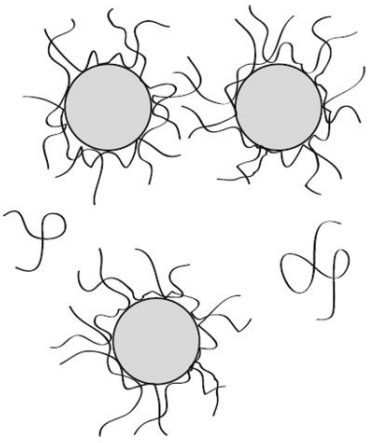

Figure 1.13. Schematic illustration of colloidal particles sterically stabilized through polymer adsorption [102].

Adsorbed polymers may adopt different conformations at the interface, commonly described as trains (segments directly bound to the surface), loops (segments extending into the solution between anchor points), and tails (chain ends protruding into the solution) [103]. Segments with strong surface affinity act as anchoring points, while non-adsorbing segments remain solvated by the medium and extend into solution, providing steric stabilization. The repulsive steric force strongly depends on the thickness of the adsorbed layer as well as on the density of monomers in the adsorption layer including its variation perpendicular to the particle surface. In cases where the thickness of the adsorbed layer is much smaller than the particle diameter, the monomer density can be approximated to be constant and the repulsive potential decreases quadratically with particle surface separation [104]. In graphite anode slurries, particle stabilization is primarily electrosteric. Anionic polyelectrolytes CMC or PAA adsorb onto the graphite particles, in neutralized slurries, their carboxyl groups are dissociated and the polymer chains extend into the surrounding aqueous phase creating a steric barrier that prevents particle contact and provides dispersion stability [105].

2. Motivation and manuscript outline

This thesis is an experimental investigation into the role of polymeric binders in waterborne slurry processing, as well as mechanical stability, microstructure, and electrochemical properties of lithium-ion anodes to create a tailored binder concept that yields anodes with improved processing behavior and electrochemical performance, based on industrially relevant formulations. Hereby, the study does not focus on the synthesis of novel polymers, but on the use of tailored mixtures of commercially available, well-established polymeric binders.

The effects of polymer concentration and type on electrode mechanical properties, processability, and electrochemical performance are systematically studied. Furthermore, the adsorption behavior of polymeric binders on various active materials and the adhesion strength between individual anode components are quantified and correlated with the mechanical properties of the anodes. The correlation between binder and microstructure of the active materials is also investigated in relation to the mechanical properties of the corresponding electrodes. Finally, building on these findings, the application of a commercially available acrylate polymer with specific functionalities is introduced as an effective binder for high-rate graphite anodes.

The first section of this thesis provides a concise overview of the global environmental context and highlights the role of lithium-ion batteries as a critical technology for sustainable energy storage. This is followed by an introduction of the fundamentals of lithium-ion batteries, including their components, with particular emphasis on negative electrodes, their working principles, manufacturing processes, and the basic concepts of electrochemistry. In addition, the theoretical background on interparticle interactions in colloidal dispersions and their stability is introduced. The introductory part concludes with the motivation for this work and an outline of the thesis structure. The main body of the thesis is divided into three sections, each comprising a scientific article published in a peer-reviewed journal.

The first scientific paper (section 3) addresses the determination of the optimal adhesion level of the aqueous processed graphite anodes that enables failure-free electrode processing while maintaining the robust electrochemical performance of the cell. This work provides a comprehensive mechanical characterization of graphite anodes, including benchmarking. Graphite anodes with varying adhesion strengths and two different industry-relevant mass loadings were fabricated, and their mechanical properties, including cohesion and adhesion, were characterized both before and after calendering. These results highlight the functionality of SBR, demonstrating its role not only as an adhesion promoter but also in enhancing anode cohesion. The anodes were further evaluated for their susceptibility to various mechanical stresses that occur during electrode processing steps, such as bending, winding, punching, and cutting. The adhesion strength between the anode active layer and the copper current collector was systematically adjusted by varying the SBR concentration. Furthermore, the electrochemical performance of the graphite anodes

was evaluated in a full-cell pouch configuration. To assess morphological and mechanical changes in the electrodes induced by long-term cycling, a post-mortem analysis was performed, comprising visual inspection, light microscopy, SEM, and 90°-peel tests.

Section 4 presents a scientific article that investigates the effect of an adsorbing polymeric binder, originally designed as a thickening and dispersing agent, within a two-binder system on the adhesion strength between the active anode layer and the copper current collector. To this end, aqueous processed anodes containing three different active materials (graphite, micro-silicon, and nano-silicon) and a CMC-SBR binder system were produced. CMC with three different molecular weights was employed, and the adsorption behavior of CMC on the three different active materials was evaluated using a rheological approach. The adhesion strength between the individual anode components (active materials, CMC, and copper current collector) and SBR was determined by 90°-peel tests. The adhesion strength of anodes with varying active materials and CMC M_w was then evaluated, analyzed in relation to the adsorption results and to the peel tests of electrode components with SBR films, and compared against reference anodes prepared with a non-adsorbing polymeric binder. Furthermore, the influence of the porous structure of the active material, examined for nano-silicon, on the anode´s adhesion strength was investigated through gravimetric experiments.

The third publication (section 5) examines the suitability of a highly cross-linked polyacrylic acid (x-PAA) copolymer as a non-adsorbing binder with high thickening efficiency for the fabrication of high-rate graphite anodes. In this study, a commercially available polymer, Carbopol Ultrez 10 from Lubrizol (USA), was employed to prepare water-based anode slurries with high-shear viscosities comparable to those of the CMC reference. The mechanical properties of the corresponding electrodes were systematically investigated using 90°-peel tests to evaluate adhesion and compression tests to assess cohesion. In addition, the electrochemical performance of graphite anodes containing x-PAA binder was further evaluated in comparison with two reference formulations employing CMC and linear PAA (l-PAA) binders. To this end, pouch cells with commercial NMC111 cathodes were assembled and subjected to rate capability tests in both charge and discharge directions, as well as long-term cycling stability evaluations. Following the rate capability tests in the charge direction and after extended cycling, the cells were disassembled and subjected to post-mortem analyses to elucidate the effects of cycling, with particular attention to lithium plating and the deterioration of anode mechanical properties.

Sections 6 and 7 conclude this thesis with a summary and an outlook. The summary highlights the key findings regarding different aspects of binder functionality in aqueously processed anodes for lithium-ion batteries, emphasizing their impact on electrode processing, mechanical integrity, and electrochemical performance. The outlook extends the discussion by identifying potential research directions and development opportunities focused on enhancing the use of polymeric binders in next-generation lithium-ion battery technologies.

3. Effect of mechanical properties on processing behavior and electrochemical performance of aqueous processed graphite anodes for lithium-ion batteries

Full title:	Effect of mechanical properties on processing behavior and electrochemical performance of aqueous processed graphite anodes for lithium-ion batteries
Authors:	Katarzyna Hofmann, Akshay Dattatraya Hegde, Xinyang Liu-Theato, Ronald Gordon, Anna Smith, Norbert Willenbacher
Status:	Published
Bibliographic data:	Journal of Power Sources 2024; 593: 233996; DOI: 10.1016/j.jpowsour.2023.233996

Abstract

A combination of styrene-butadiene rubber (SBR) and sodium carboxymethyl cellulose (CMC) is a well-established binder system in aqueous processed anodes for lithium-ion batteries. The main function of SBR is to increase the adhesive strength between the active anode layer and the current collector, providing a robust connection capable of withstanding mechanical stresses encountered during cell manufacturing and cell cycling. To determine the optimal adhesion level ensuring failure-free processing without compromising the electrochemical performance we variated SBR concentration and investigated the effect on the processability and electrochemical performance of graphite anodes with application relevant mass loadings (5.7 mg cm^{-2} and 10.1 mg cm^{-2}). Our results indicate that the inclusion of SBR enhances cohesion of anodes, a vital factor in preserving the mechanical integrity during bending, winding and cutting, particularly at elevated mass loadings. However, our findings reveal that unnecessarily high adhesion does not yield benefits on the processability of anodes. Furthermore, SBR is virtually dispensable for adhesion during cell cycling, and it proves to be counterproductive, primarily due to the rise in internal resistance and, most likely, SBR degradation. For the system investigated here, optimal adhesion was found for 1.5% SBR in the current collector-free anode.

3.1. Introduction

Aqueous processed anodes are state-of-the-art electrodes for lithium-ion batteries. They consist of active material, conductive additives and polymeric binders, which are coated on the copper current collector after aqueous processing into a homogeneous slurry. To distinguish between an electrode with a current collector and a current collector-free active layer, in this publication, the term 'electrode layer' specifically refers to the current collector-free electrode.

A combination of sodium carboxymethyl cellulose (CMC) and styrene butadiene rubber (SBR) is a widely used binder system for aqueous processed anodes [57,106,107]. In industry-relevant formulations, the binder concentration varies in the range from 2 to 5 wt% [55] with the CMC to SBR ratio being between 1:1 and 1:3 [108–112]. The cellulose serves mainly as a thickener and stabilizer, while SBR ensures high adhesion of the electrode layer to the current collector [57,62,64,106,107]. Adhesion, together with cohesion, determines the mechanical stability of the electrode, which is subjected to various mechanical stresses, both external during manufacturing and internal during cell cycling. The determination of the optimal electrode adhesion level, ensuring their failure-free processing without compromising the electrochemical performance, is a crucial inquiry in electrode manufacturing. Nevertheless, a precise quantitative criterion for achieving this remains notably absent.

The production of lithium-ion battery cells consists of multiple steps. In general, three main manufacturing stages can be distinguished: electrode production, cell fabrication, and cell finishing [84]. As starting point of the electrode production, all components - active material, conductive agent, polymeric binders, and solvent - are mixed to form a homogeneous slurry. Avoiding agglomeration and ensuring uniform contact between all particles is of great importance for the transport processes of electrons and lithium ions within the electrode [113,114]. In addition, the slurry must exhibit suitable flow properties to ensure adequate processability during the coating process. In the next step, the slurry is cast on a metal current collector and dried, which is the most energy-intensive step in the entire battery manufacturing [71]. The electrodes are then transported to the calender and compressed in order to improve anode’s properties such as volumetric energy density, conductivity, particle contact and mechanical properties [82]. Calendering is followed by slitting, wherein electrode sheets are cut in a longitudinal direction [115]. Here care must be taken to minimize cut-off waste with respect to material costs and particle contamination. Depending on cell design, the electrodes are either punched and stacked (pouch cells) or wound around a mandrel or a pin (prismatic and cylindrical cells) [84]. After packaging and filling with the electrolyte, the cells undergo the most expensive and time-consuming manufacturing step: cell formation [116]. The battery production line relies heavily on the use of roll-to-roll technology, enabling shorter lead times for the various stages of production, thereby increasing process productivity [71].

The variety and complexity of external mechanical loads, such as compression, bending or tension, to which electrodes are exposed during the manufacturing process, increase the risk of losing their mechanical integrity. Adjustment of process parameters such as calender pressure, roller speed or temperature profile during drying can reduce the mechanical stress exerted on the electrodes. However, these possibilities are technically limited. The state-of-the-art loading density of graphite anodes in automotive applications reaches values up to 18 mg cm^{-2} corresponding to an areal capacity of 5.23 mAh cm^{-2} [117]. For electrodes with such high mass loading the manufacturing process becomes significantly more challenging, since thicker electrodes tend to delaminate and fracture. It is generally postulated that a pronounced adhesion can offer significant advantages in electrode manufacturing [115].

On the other hand, electrodes experience internal stresses during cycling arising from the volume changes of the active material particles due to the repeating (de)intercalation of lithium-ions with each charge and discharge cycle, respectively. As a result, deformation of the electrodes may occur [118]. Consistent with the prevailing notion in the field of battery technology, it is widely acknowledged that high electrode adhesion is the key to improved electrochemical performance and prolonged battery cycle life, as sufficient adhesion significantly reduces the risk of delamination, thereby preventing the loss of electrical contact between the active layer and the current collector [115,119–126]. Lee et al. [125] observed better capacity retention of CMC/SBR-based graphite anodes with the addition of 0.6 % polyacrylic acid (PAA, M_w = 5 kDa). This was attributed to enhanced adhesive strength of anodes resulting from the inclusion of PAA. However, it must be considered that cycle performance depends on many different factors such as the chemistry of the binder used. To the best of the authors' knowledge, the influence of adhesion alone on the electrochemical performance of electrodes, independent of other factors affecting electrochemistry, has not been studied yet.

SBR is synthesized from 1,3-butadiene and styrene monomers and its properties depend on molecular structure, i.e. the ratio of styrene to butadiene, degree of cross-linking, type of emulsifier, polymerization temperature, etc. [67,127]. In the battery industry, SBR is used in latex form. The addition of SBR to the anode paste affects not only the adhesion but also the internal bonding between particles. Lim et al. [122] investigating the impact of SBR and CMC on the drying behavior of anode slurries using cantilever deflection method found that due to the bridging of graphite particles by SBR, the drying stress increases, indicating improved mechanical properties of the electrode layer. However, the literature lacks data on the cohesion of anodes containing SBR in industrially relevant quantities. Furthermore, determining the cohesive strength within the thin electrode layer can be challenging, as the measured values often include both particle – particle cohesion and electrode layer – current collector adhesion. Son et al. [128] introduced a method using the Surface and Interfacial Cutting and Analysis System (SAICAS) which allows a measurement of cohesion at a specific depth within the electrode composite. Gordon et al. [62] were

the first to determine cohesion values independently of anode adhesion by subjecting thick anode layers to well-defined mechanical load.

In this paper we present novel findings and insights into the role of SBR and the corresponding mechanical properties (adhesion and cohesion) of industry-relevant aqueous processed graphite anodes, concerning their impact on processing and electrochemical performance. Given that the choice of SBR concentration, and thus the level of electrode adhesion, in industrial production strongly depends on the cell design, we produced and investigated anodes with varying SBR content (0 wt%, 1.5 wt%, 2.8 wt% and 4.5 wt%) and two different mass loadings (5.7 mg cm^{-2} and 10.1 mg cm^{-2}, corresponding to areal capacities of 2.15 mAh cm^{-2} and 3.50 mAh cm^{-2}, respectively).

Firstly, we examine the impact of the mechanical properties of anodes, altered by varying SBR concentration, on their processability through bending and winding tests, as well as their crack-susceptibility during punching and cutting. Subsequently, we investigate the electrochemical performance of the anodes in single-layered pouch cells, focusing on the effects of the mechanical properties varying with SBR content. Finally, post-mortem analysis of cycled anodes is conducted to investigate morphological and mechanical changes in the electrodes induced by long-term cycling.

3.2. Experimental

3.2.1. Materials

Surface-modified natural graphite (SMG A5, Showa Denko Materials Co, Ltd., Japan) with elongated irregularly shaped particles (Supplementary Figure S3.1) with an average particle diameter $x_{50,3}$ = 17,8 µm and density of 2.23 g cm^{-3} was used as an active material in the water-based anode slurries. Carbon black (CB, C-Nergy Super C65, Imerys Graphite & Carbon, Switzerland) with an average primary particle size $x_{50,3}$ = 32 nm and density of 1.8 g cm^{-3} served as a conductive agent. Sodium carboxymethyl cellulose (CMC, TEXTURECEL 20000 GA 07, DuPont, USA) with an average molecular weight of about M_w = 700 kDa and degree of substitution DS = 0.7 was utilized as a binder. The second polymer used in the current study was styrene butadiene rubber (SBR, TRD 2001, JSR, Japan), which is a 48 vol% aqueous dispersion composed of 170 nm particles with a glass transition temperature of −2 °C and a degree of cross-linking of 89.9 % ± 0.5 % [62].

3.2.2. Sample preparation

In order to set different degrees of adhesion between electrode layer and copper current collector slurries with varying SBR weight concentrations (0 wt%, 1.5 wt%,

2.8 wt%, 4.5 wt% - referred to the dry anode layer) but with a constant solid mass content x_s = 42 wt% and a constant graphite to carbon black mass ratio of 49:1 were prepared. The fixed concentration of CMC was 2 wt% with respect to dry film. In the first step, CMC granulate was dissolved in 95 % of the total amount of distilled water by stirring with a propeller at 1200 rpm for 30 min. First, carbon black and subsequently graphite powder was added to the resulting 1.5 wt% CMC solution and stirred with a dissolver at 2000 rpm for 5 min in each step. Finally, SBR was admixed to the paste by using the same mixing parameters. Slurries with no addition of SBR continued to be stirred for the next 5 min, so the total mixing time was identical for all pastes. In the last step, the remaining amount of distilled water was added to set the target solid content and the slurry was mixed at 2000 rpm for additional 5 min. The resulting slurries were degassed in a desiccator and cast on a 10 µm thick copper foil (SE-Cu, Schlenk Metallfolien GmbH & Co. KG, Germany) using a doctor blade (ZUA 2000, Zehntner GmbH, Switzerland) with the coating velocity of 10 mm s^{1}. To obtain anodes with different areal capacities, 2.15 mAh cm^{2} and 3.50 mAh cm^{-2} the coating gap was set to 160 µm and 250–265 µm, respectively. The anode tapes were dried at 70 °C for 30 min. Some of the prepared anodes were calendered with a roll-to-roll calendar (GKL, Saueressig GmbH, Germany) with a roll width of 400 mm and a working speed of 1 m min^{-1}. Anodes were compressed to a target porosity of about 50 %. The specifications of the anodes are summarized in Table 3.1. In addition, specimens subjected to the compression test for cohesion characterization were prepared by pouring the slurry into a silicone mold and drying it at 50 °C for about 18 h. Subsequently, the anode bricks were cut and ground into 5 mm × 5 mm cubes using sandpaper.

Tab. 3.1 Parameters of anode layers with two different mass loadings before and after calendering.

Graphite mass loading, mg cm^{-2}	Areal capacity, mAh cm^{-2}	Dry coating thickness before calendering, µm	Porosity before calendering, %	Density before calendering, g cm^{-3}	Dry coating thickness after calendering, µm	Porosity after calendering, %	Density after calendering, g cm^{-3}
5.7 ± 0.2	2.15	65 ± 3	57 ± 2	0.94 ± 0.04	56 ± 1	49 ± 1	1.09 ± 0.01
10.1 ± 0.3	3.50	111 ± 3	55 ± 1	0.97 ± 0.04	101 ± 3	51 ± 1	1.07 ± 0.04

3.2.3. Rheological characterization

For the determination of the flow behavior of anode slurries, a stress-controlled rheometer (Physica, MCR 501, Anton Paar GmbH, Germany) with a plate-plate geometry (PP25TG, diameter d = 25 mm, gap height h = 1 mm) was used. Rotational steady shear measurements were performed in a logarithmic shear stress ramp (10 points per decade) from 0.01 to 1000 Pa at 20 °C and in a logarithmic time scale from 60 s to 5 s.

3.2.4. Mechanical characterization

Compression test

In order to determine the cohesive strength of anodes a compression test according to DIN 51104 standard was carried out. For this purpose, a universal testing machine (Texture Analyser TA.XT plus, Stable Micro Systems, UK) with a 50 kg load cell was utilized.

Peel test

The adhesion strength of fresh non-calendered and calendered anodes as well as of cycled anode tapes was determined in a 90°-peel-test using a universal testing machine (Texture Analyser TA.XT plus, Stable Micro Systems, UK) with a 5 kg load cell. Cycled anodes were rinsed with DMC and oven-dried overnight before testing. Anode tapes were cut into 2.5 cm wide strips and almost the entire sample length was fixed with double-sided adhesive tape on a movable test plate. A protruding part of the anode was clamped to the machine arm forming a 90° angle. Samples were peeled with a constant velocity of 5 mm s^{-1}. The force needed to peel the coatings from the copper foil was recorded, normalized to the sample width, and averaged over at least 3 measurements. In this way, the line load was determined and used in this study as a measure of adhesion.

In addition, adhesion values were determined for calendered, non-cycled commercial graphite anodes with CMC/SBR as binder system and with 3.50 mAh cm^{-2} capacity as benchmark for our in-house fabricated 10.1 mg cm^{-2} (3.50 mAh cm^{-2}) anodes.

Bending test

To examine the bendability of the anodes, non-calendered tapes were tested using a universal testing machine (Texture Analyser TA.XT plus, Stable Micro Systems, UK) with a 5 kg load cell and an additional setup, specially designed for this purpose. A single-sided coated electrode tape was rolled on its non-coated side over a 45 mm diameter cylinder, attaching one end of the electrode to a clamp and the other to the Texture Analyser arm, which during the test pulled the electrode at a constant

angle of 90° and at a constant speed of v = 1 m min^{-1}, simulating the trajectory of the electrode in a continuous coating/drying line for sample production. In addition, each experiment was recorded with a camera (Bresser MikroCamII 3.1 MP, Bresser GmbH, Germany) and optically analyzed in terms of crack formation. The camera's focus was directed to the specific spot where the anode was bent on the roll.

Winding test

To investigate the winding ability of anodes as a function of SBR content, calendered anode tapes were attached to a 5 mm diameter steel pin using adhesive tape and wound. Subsequently, the tapes were unwound and examined using an optical microscope (Keyence VHX- 6000, Keyence Corporation, Japan) for any signs of crack formation.

Cutting and punching

Delamination and particle abrasion of the anode coating during cutting and punching as a function of SBR concentration was visually investigated. A hand-held punching device (Nogami, Japan) with a diameter of 15 mm was used to punch out multiple samples for half-cell measurements in coin cells. Similarly, a punching device based on steel band cutting (Manz, Germany) was used to punch 5.4 cm × 5.4 cm sized anode samples for pouch cell assembly.

3.2.5. Electrochemical characterization

Cell assembly

Two types of anodes with different mass loading were fabricated. The anodes with lower mass loading exhibit an areal capacity of 2.15 mAh cm^{-2} and the anodes with the higher mass loading 3.50 mAh cm^{-2}. The practical areal capacities were determined using a half-cell setup in coin cells. To this end, anode specimens and separators were dried in a vacuum oven for 24 h at 130 °C and 180 °C, respectively. The counter electrode consisted of metallic lithium (MTI Corporation, US) with a diameter of 15.8 mm and a thickness of 250 µm. Working electrodes were prepared by punching the anodes with a diameter of 15 mm. The separator, made of glass fiber (GF/B) with a diameter of 17 mm and a thickness of 1.5 mm was obtained from Whatman QMA (US). Finally, 200 µl LP30 (50 wt%/50 wt% ethylene carbonate (EC)/dimethyl carbonate (DMC) and 1 M LiPF6) for each coin-cell was used as electrolyte. For cell assembly, spacers with a diameter of 16 mm and a thickness of 0.5 mm were utilized. The assembled cells were then subjected to a pressure of 6.89 MPa using a hydraulic crimper (MSK-110, MTI Corporation, US) and stored at 40 °C overnight to ensure adequate wetting before electrochemical measurements.

For the pouch cell assembly, calendered anodes and commercially available single-sided coated cathodes were punched with sizes of 5.4 × 5.4 cm and 5.0 × 5.0 cm, respectively. The separators used were 5.9 × 5.9 cm in size and consisted of a PET-based material with a ceramic coating. After vacuum drying for 24 h at 130 °C (electrodes) and 180 °C (separators), lab-scale pouch cells were assembled under dry room conditions (–60 °C dew point) in a semi-automated manufacturing line. Then, 5.7 mg cm^{-2} and 10.1 mg cm^{-2} anodes were paired with commercial NMC111 ($LiNi_{0.33}Mn_{0.33}Co_{0.33}O_2$)- and NMC622 ($LiNi_{0.6}Mn_{0.2}Co_{0.2}O_2$)-based cathodes, respectively. The areal capacity of the NMC111 cathode corresponds to about 1.75 mAh cm^{-2} and that of the NMC622 cathode to about 3.0 mAh cm^{-2}. In the next step, cells were filled with 450 µl (5.7 mg cm^{-2} anodes) or 900 µl (10.1 mg cm^{-2} anodes) LP30 with 3 wt% of vinylene carbonate (VC) as an additive. The cells were then sealed under vacuum. Finally, cells were stored in an oven overnight at 40 °C to allow for complete wetting.

Formation cycle

In the formation step, half-cell type (Gr‖Li) coin cells and full-cell type (Gr‖NMC) pouch cells were cycled using Basytec CTS LAB in the voltage window 0.005 V–1 V and 3 V–4.2 V, respectively. Cells were charged (lithiation of graphite) with 0.1C constant current (CC), up to 0.005 V (half coin-cells) and 4.2 V (full cells), and held at the respective potential until current dropped below 0.05C during the constant voltage (CV) step. Half coin and pouch cells were discharged (delithiation of graphite) at 0.1C (CC). In total, four cycles were performed. The full pouch cells with 3.50 mAh cm^{-2} anodes were first charged with 0.1C until 4.2 V and a subsequent CV-phase until I < C/20, then discharged with 0.5C until 3 V. Afterwards 6 cycles were applied where cells were charged with 0.5C (including CV until I < C/20) and discharged with 0.5C. Finally, the full cells were charged to 3.7 V at 0.1C (CC) for storage until the following cell test.

Rate capability test

Full pouch cells were subjected to different discharge C-rates to evaluate their rate capability. Therefore, cells were always charged using a CCCV method (0.5C until 4.2 V, CV until I < C/20). For the discharge step, the C-rate was systematically varied between 0.5C and 5C using a CC method. Each C-rate variation was carried out for two full cycles. Finally, two last cycles at 0.5C were performed to check for degradation during rate testing. To avoid any kind of lithium plating, the test was specifically performed in discharge direction only.

Cycling test

The long-term cycling performance of the pouch cells, previously tested for the rate capability, was investigated under a CC charge method at 2C, followed by a CV phase until I < 0.1C. The discharge step was carried out at CC 3C. The voltage window for this test was set between 3 V and 4.2 V. Cells including 5.7 mg cm^{-2} anodes were cycled until 80 % of the initial capacity was reached, whereas cells based on 10.1 mg cm^{-2} anodes were stopped after about 2500 cycles.

Direct current internal resistance (DCIR) and cell capacity determination

During long-term cycling of pouch cells, a check-up cycle was performed to evaluate cell degradation. Therefore, cells were charged at 0.1C (CC until upper voltage limit, CV until I < C/20) to reach 100 % state of charge (SOC) and discharged at CC 0.1C until reaching the lower voltage limit to determine cell discharge capacity. Based on the actual discharge capacity and using an Ah counter method several states of charge (SOC), namely 10 %, 30 %, 50 %, 70 %, and 90 %, were adjusted. DCIR values were determined for these SOC applying current pulses of 1C for 20 s in discharge direction. A resting period of 30 min was applied between the different SOC values and before pulsing. Using Ohm's law, the DC internal resistances were determined based on the current and the potential drop, i.e., the difference between the voltage level at the end of the pulse and at the beginning of the pulse.

3.2.6. Anode microstructure

The microstructure of the anodes was evaluated using a scanning electron microscope (SEM) (Zeiss Leo 1530). Furthermore, anodes and separators were optically analyzed using a light microscope (OLYMPUS BX53 M, Japan) upon post-mortem analysis.

3.3. Results and discussion

3.3.1. Flow behavior

In order to investigate the influence of mechanical properties on the processing behavior and electrochemical performance of anodes, slurries with varying SBR concentration in a range between 0 % and 4.5 % were produced and rheologically characterized. All concentrations are given in weight percent and refer to the dry electrode layer unless otherwise stated. All prepared anode slurries exhibit shear thinning flow behavior (Supplementary Figure S3.2(a)) and, as expected, the SBR concentration has a minor effect on this characteristic, consistent with the findings of Lim et al. [66], who demonstrated that SBR affects the flow properties of electrode

suspensions only in the absence of CMC or at low CMC concentrations. As the CMC amount increases, its adsorption onto the graphite particles and the corresponding effect on particle-particle interactions dominate over the effect of SBR on the flow behavior of the slurry.

Furthermore, regardless of SBR amount, the slurries exhibit a moderate yield stress, ranging between 50 and 70 Pa (Supplementary Figure S3.2(b)). The negligible effect of SBR on the flow behavior of industry-relevant slurries is undoubtedly an advantage in electrode manufacturing as it allows the modification of the mechanical properties of anodes without the need to adjust the process parameters in slurry production.

3.3.2. Adhesion

Anode layers with two different mass loadings were obtained from the produced slurries and subsequently calendered. The adhesion of the anodes was investigated via 90°-peel test before and after calendering and the corresponding results are shown in Figure 3.1(a). Anodes only with CMC as a binder exhibit a line load of about 2.8 N m^{-1} and 5.5 N m^{-1} before and after calendering, respectively. The adhesive strength between the active anode layer and the copper current collector demonstrates an exponential growth with increasing amount of SBR. This trend persists regardless of anode mass loading and compression level, highlighting the role of SBR as an adhesion promoter. This anticipated outcome aligns with the findings reported in the literature [62,124,128,129]. The adhesion of the calendered graphite benchmark anode comparable to our 3.50 mAh cm^{-2} anode is 7 N m^{-1}, which corresponds to 1.5 % SBR.

Furthermore, the negative electrodes with higher mass loading exhibit about 10–25 % lower line load compared to 5.7 mg cm^{-2} anodes. The adverse effect of increasing coating thickness on electrode adhesion is established in the literature [124,129]. The adhesion is controlled by the presence of SBR on the active layer/current collector interface [124,129,130] and the decline in adhesive strength as the mass loading increases may be associated with the binder migration away from the current collector during drying [75]. However, disclosing the physical origin of this phenomenon is not straightforward and requires further fundamental research.

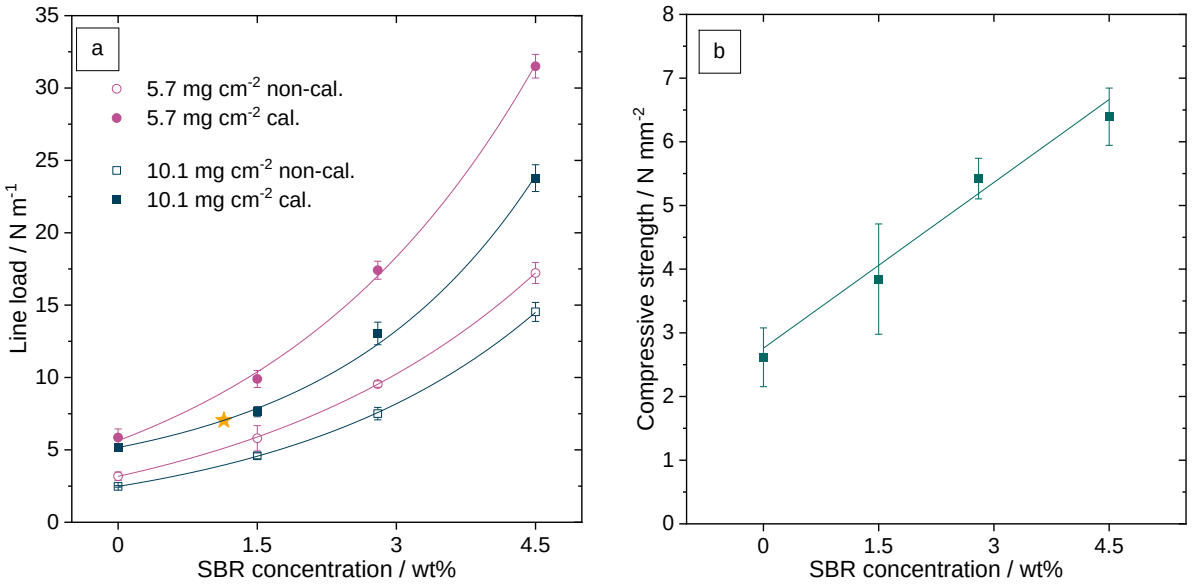

Figure 3.1. Mechanical properties of anodes with various concentration of SBR. (a) Adhesive strength of 5.7 mg cm^{-2} and 10.1 mg cm^{-2} anode layers to the copper current collector before (non-cal.) and after calendering (cal.). The exponential growth function is fitted to the data and the results are shown as straight lines with the color matching that of the corresponding experimental data. The orange star indicates the adhesive strength of the calendered benchmark anode with specifications comparable to our 10.1 mg cm^{-2} anode; (b) Compressive strength of thick anode layers as a function of SBR concentration.

The compression of the electrode coating during the calendering process leads to reduction in layer porosity and increases the particle/ particle and particle/copper foil contact area. Consequently, calendering noticeably enhances the adhesion of anodes, which is also consistent with the findings reported in the literature [131,132]. Therefore, assuming that the adhesive strength of the non-calendered electrodes is already high enough that mechanical integrity is guaranteed for the following processing, applying compression can serve as a means to reduce the binder content in anodes.

3.3.3. Cohesion

Besides adhesion, also cohesive strength is a crucial factor in ensuring the mechanical stability of electrodes. Following the method presented by Gordon et al. [62] we employ the compression test on cube shaped thick anode layers to investigate cohesion independently of adhesion. The compressive strength, defined as the maximum compressive force that a sample can withstand until fracture, is shown in Figure 3.1(b) as a function of SBR concentration. Obviously, the addition of SBR to the anode slurry enhances the cohesion of the anode layer and a linear increase with SBR concentration is observed. This suggests that SBR molecules can bridge graphite particles covered by an adsorbed CMC layer, and the elastomer can reinforce the particle network structure and hence the cohesion of the dry anode layer [121]. The observed increase in cohesive strength with SBR concentration contradicts the

findings reported in the literature [62]. However, it is important to note that the literature data were obtained for anodes utilizing synthetic graphite, which differs from the material studied in the current work. This may be significant because CMC bound to natural graphite through van der Waals interactions may be easier released from the graphite surface during drying than CMC bound to artificial graphite by covalent bonds [75]. This in turn can affect the distribution of SBR, which may adhere to the released graphite surface, bonding the particles together and improving cohesion. This topic requires further in-depth investigations beyond the scope of this work.

We selected and reproduced, on a lab-scale, three processes occurring during the fabrication of electrodes: bending of non-calendered anodes, winding of calendered anodes and cutting. The results of the relationship between the mechanical properties of anodes and their processability are presented and discussed below.

3.3.4. Bending

An integral part of electrode fabrication is the transport of coated foils (un-/winding of electrode coils) between the production stages using roller profiles. By redirecting the anode sheets by 90° (Figure 3.2(a)), we tested the fracture resistance of the non-calendered anodes as a function of SBR content and electrode layer thickness. According to the linear-elastic bending theory, the thicker the specimen to be bent, the greater the bending stresses acting on it. Assuming a linear shear stress distribution over the rectangular cross-section of the specimen, the shear stress increases from the axis of the neutral line towards the outer edge, where it reaches its maximum. The thicker the coating, the greater the forces acting on its edge. All electrodes, with the exception of the thick one without SBR, withstood the applied bending stress without any visible coating defects. Obviously, the compressive strength of the anodes is high enough to withstand the acting bending forces, except for the thick layer without SBR. In this case, the compressive strength is lowest and the bending force highest, and we can observe multiple cracks in longitudinal direction (Figure 3.2(c)). Since the only parameter that differentiates the bending test of 5.7 mg cm^{-2} and 10.1 mg cm^{-2} anodes is the force acting on the film related to the difference in its thickness, it becomes obvious that cohesion is a key property for maintaining anode integrity during bending.

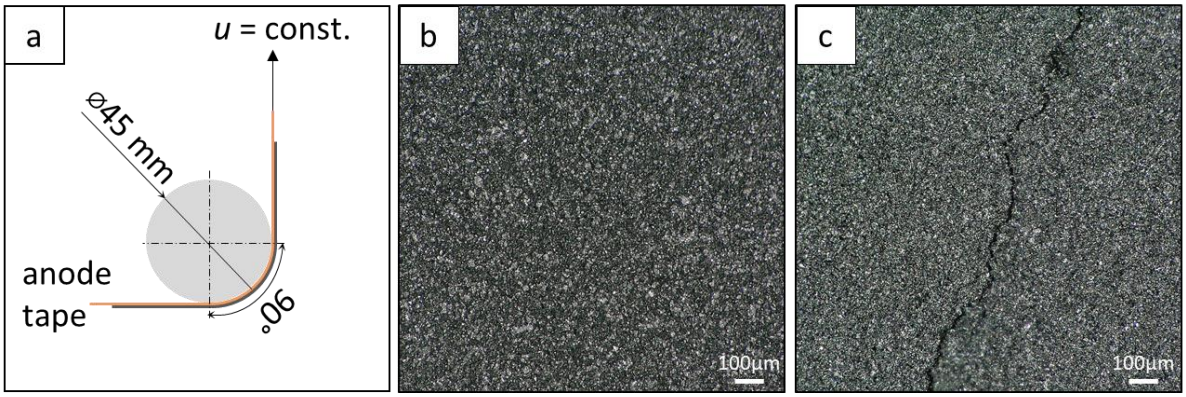

Figure 3.2. Schematic depiction of bending test for non-calendered anode tapes (a) and microscopic images of anode with higher mass loading without SBR before (b) and after bending test (c).

3.3.5. Winding

During manufacturing of cylindrical cells, electrodes are wound around a mandrel. In the winding test, we examine the calendered anodes for their coilability. Compared to the bending test, anode samples experience greater stresses, primarily due to the significantly smaller diameter of the metallic pin used for winding (9 times smaller than the diameter of the roll cylinder). Based on the obtained results presented in Figure 3.3 and Supplementary Figure S3.3, three findings can be drawn. First, anodes with lower mass loading show less intense cracking than thicker anodes. The former exhibit some micro-cracks due to winding (Figure 3.3(b)), whereas the latter show significantly more cracks and coating bulges in the longitudinal direction (Figure 3.3(c)). This can be explained by the fact that thicker electrodes exhibit higher bending stresses at their surface as outlined in section 3.3.4. Similarly, more cracking is expected to occur if a thinner mandrel would be used.

Second, the winding tests do not show a correlation between the occurrence of cracks and the adhesion strength of the active layer to the current collector. Third, additional winding tests conducted on uncompressed 10.1 mg cm^{-2} anodes with 2.8 % SBR and with about the same adhesion level as calendered 10.1 mg cm^{-2} anodes without SBR showed severe cracking and delamination of the electrode coating (Supplementary Figure S3.3). This confirms findings from a literature study [133], in which LMO-based non-calendered cathodes were exposed to a controlled bending load by pulling them over mandrels of different diameters. Using confocal microscopy, they detected coating defects (cracks, wave formation and delamination), which vanished as the calendering degree increased.

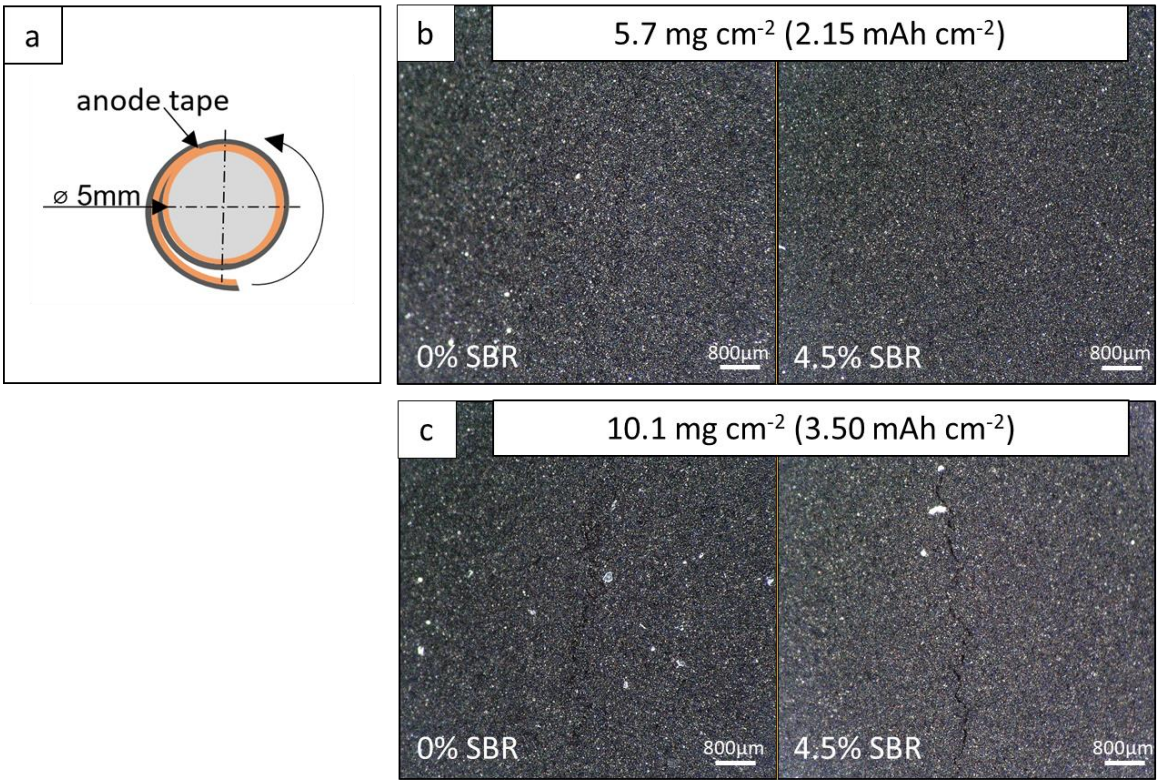

Figure 3.3. (a) Scheme of winding test for calendered anode tapes; microscopic images of anodes with a mass loading of 5.7 mg cm^{-2} (b) and anodes with a mass loading of 10.1 mg cm^{-2} (c) with 0 % and 4.5 % of SBR after winding test.

3.3.6. Cutting

Slitting is an indispensable step preceding cell assembly, the key aspect of which is to achieve high-quality cuts on the electrode edges and minimize cut-off-waste. In the present study, calendered anodes are examined during steel band cutting with regard to coating delamination and particle abrasion. Figure 3.4 and Figure S3.4 show cut calendered anodes with mass loading of 5.7 mg cm^{-2} and 10.1 mg cm^{-2}, respectively, containing different amounts of SBR. A clear dependence is apparent. Higher SBR concentration leads to lower particle abrasion and minimized layer delamination upon cutting, indicating improved mechanical stability. Electrodes without SBR exhibit jagged and uneven edges after cutting, whereas increasing SBR concentration results in cleaner and more precise cuts. A similar trend was observed while cutting the calendered and non-calendered anodes with a paper guillotine in order to prepare samples for the 90°-peel-test (Supplementary Figures S3.5–S3.7).

The obtained results underscore the significance of both adhesion and cohesion during electrode cutting. When these mechanical properties are elevated, they contribute to achieving cuts of superior quality.

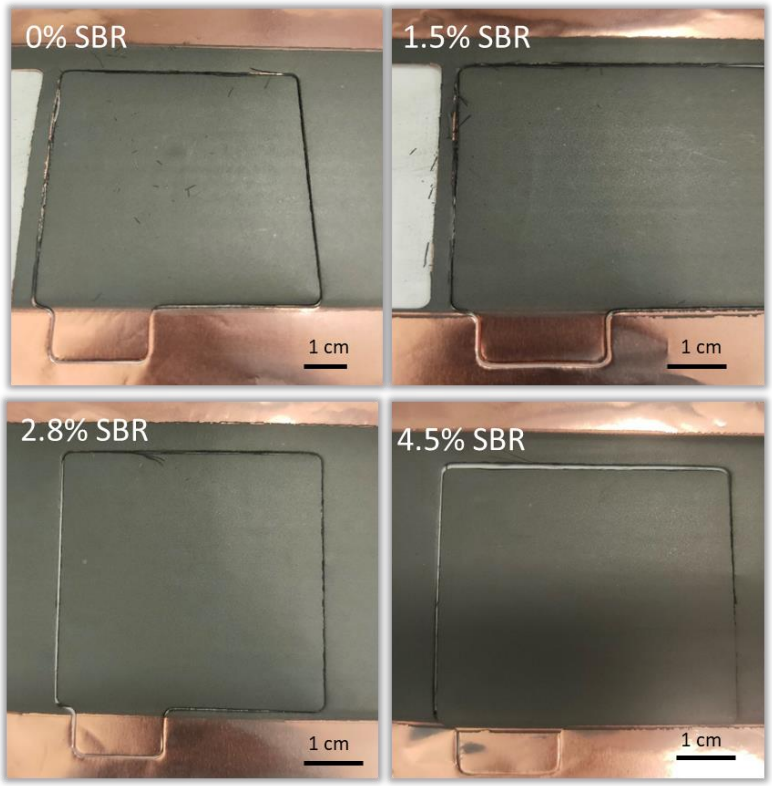

Figure 3.4. Calendered punched 5.7 mg cm^{-2} (2.15 mAh cm^{-2}) anodes containing different SBR concentrations.

3.3.7. Cell performance

To match our in the lab available commercial cathodes, namely NMC111 with 1.75 mAh cm^{-2} and NMC622 with 3.00 mAh cm^{-2} areal capacity, the target areal capacity of anodes with lower and higher mass loading was set at 2.15 mAh cm^{-2} and 3.50 mAh cm^{-2}, respectively, in terms of full-cell balancing.

The practical areal capacity of anodes with varying film thicknesses and resulting anode loading was determined through tests conducted in half-cell type coin cells. The measured capacities were plotted against the coating gap, and the data were fitted with a linear function (Supplementary Figure S3.9). In this way, a coating gap of 160 µm for 2.15 mAh cm^{-2} anodes and 250 µm, 255 µm, 260 µm and 265 µm for 3.50 mAh cm^{-2} anodes containing 0 %, 1.5 %, 2.8 % and 4.5 % SBR, respectively, was determined. This corresponds to a graphite mass loading of 5.7 ± 0.2 mg cm^{-2} and 10.1 ± 0.3 mg cm^{-2} for 2.15 mAh cm^{-2} and 3.50 mAh cm^{-2} anodes, respectively.

Since the coin-cell tests in half-cell configuration are not suitable for evaluating the rate stability and long-term cycling [134], full-cell type pouch cells were built to obtain rate capability and long-term cycling stability data for the different anodes. To this end, 2.15 mAh cm^{-2} and 3.50 mAh cm^{-2} anodes were paired with NMC111 and NMC622 cathodes, respectively. All electrochemical tests were carried out on three cells for each anode formulation.

Asymmetric rate capability tests of anodes in pouch cells were conducted at a constant charging rate of 0.5C, which was completed using a constant voltage phase with a current limit of I < C/20, and varying discharging rates between 0.5C and 5C. The absolute initial cell capacity at 0.5C is independent of SBR concentration and is about 43 mAh and 70 mAh for 2.15 mAh cm^{-2} and 3.50 mAh cm^{-2} anodes, respectively (Supplementary Figure S3.10).

Figure 3.5(a) illustrates the rate performance in terms of relative capacity retention for cells containing 5.7 mg cm^{-2} anodes with different SBR fraction. Up to 3C a slight decrease in the relative cell capacity is observed with increasing C-rate, which is independent of SBR concentration. Starting at 3C, there is a pronounced decline in cell capacity with increasing C-rate and SBR concentration. The retained cell capacities at 3C are as follows: 90 %, 89 %, 88 % and 85 % for corresponding anodes with 0 %, 1.5 %, 2.8 % and 4.5 % SBR, respectively. At 5C the retained capacity drops to 81 %, 77 %, 74 % and 59 % for anodes including 0 %, 1.5 %, 2.8 % and 4.5 % SBR, respectively.

Cells including anodes with higher mass loadings follow a similar trend as 5.7 mg cm^{-2} anodes. The results of the rate capability test for cells containing 10.1 mg cm^{-2} anodes are shown in Figure 3.5(b). At C/2 and 1C all cells show comparable relative capacity, respectively. However, starting at 2C a systematic decrease in relative cell capacity with increasing SBR fraction becomes evident. At 3C the retained capacity is about 70 %, 67 %, 58 % and 43 % for cells with anodes containing 0 %, 1.5 %, 2.8 % and 4.5 % SBR, respectively. This expected effect is more pronounced at the highest studied C-rate (5C) and is attributed to increased internal cell resistance due to elevated fraction of electrochemically inactive material, namely SBR. Higher internal cell resistance leads to pre-mature reaching of cell voltage limits, restricting charge amount during discharge and thus reducing relative cell capacity. However, it must be considered that C-rates higher than 3C are less relevant for the application of anodes with higher mass loading. All cells show similar capacities at the last step of the test using C/2 cycles compared to the initial capacities at C/2, highlighting that no obvious degradation took place during the rate test. This further supports a relation between poor rate capability and elevated internal cell resistance most likely due to higher SBR fractions.

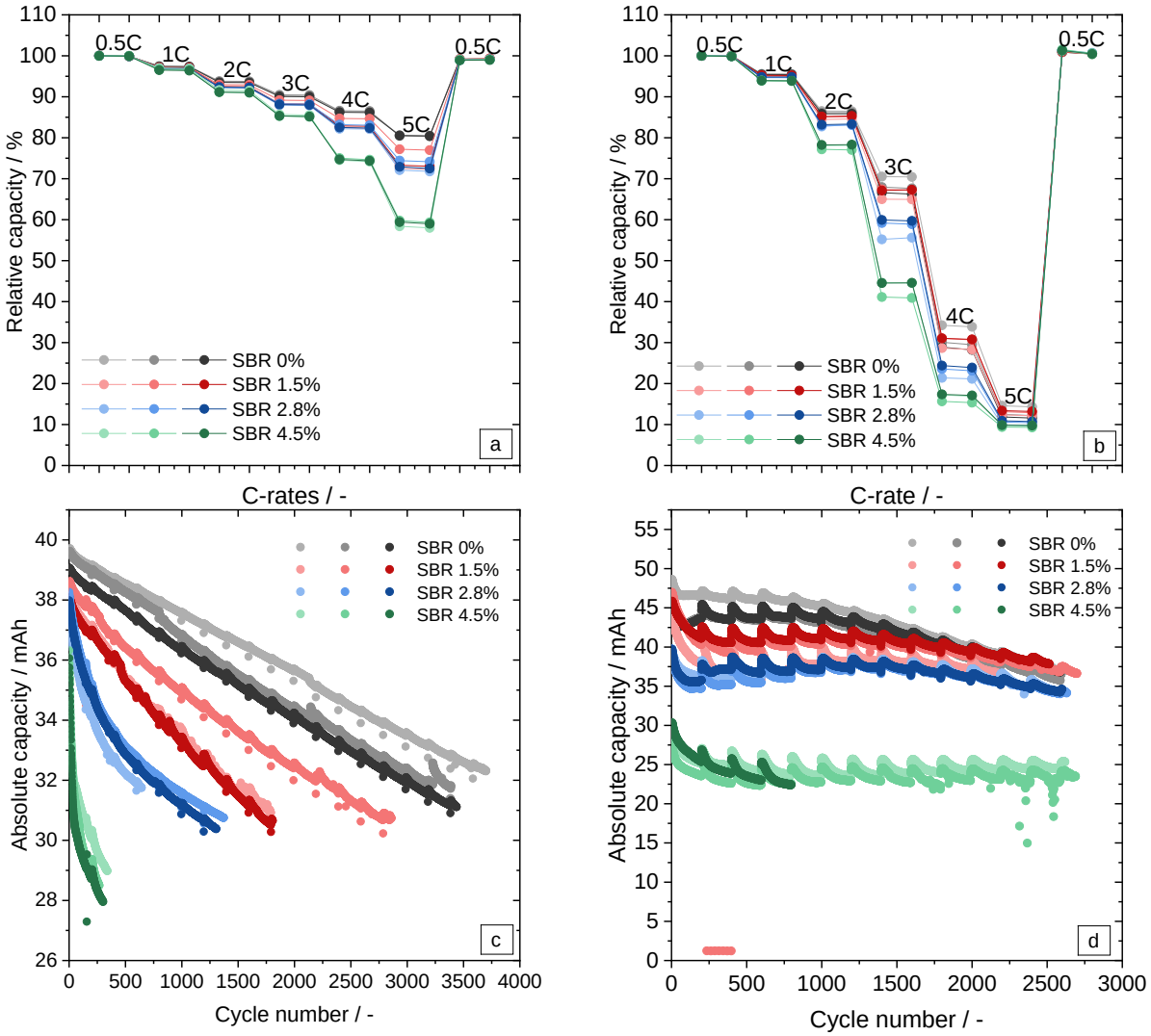

Figure 3.5. Relative cell capacity as function of discharge C-rate for pouch cells containing 5.7 mg cm^{-2} (a) and 10.7 mg cm^{-2} (b) anodes with different SBR concentrations; Absolute capacity as a function of cycle number for pouch cells containing 5.7 mg cm^{-2} (c) and 10.7 mg cm^{-2} (d) anodes with different SBR concentrations; Three cells were tested for each anode composition.

Long-term cycling was performed on pouch cells under 2C charge CC with CV (I < C/10) and 3C discharge CC cycling protocol. Note that every 200 cycles a check-up cycle was performed applying a C-rate of C/10 resulting in such disturbed cycling data every 200 cycles. Cells containing anodes with a mass loading of 5.7 mg cm^{-2} were stopped after reaching 80 % of their initial capacity. Conversely, cells with 10.1 mg cm^{-2} anodes were stopped after around 2500 cycles. The evolution of absolute discharge capacity against cycle number for cells containing anodes with lower mass loading is provided in Figure. 3.5(c). All cells show nearly the same initial capacity of around 39 mAh and a monotonic capacity loss upon cycling. Remarkably, anodes with the highest SBR content show drastic capacity fading, reaching 80 % of their initial capacity after only about 200 cycles. In contrast, the pouch cells containing

anodes with 0 % and 1.5 % of SBR exhibit a capacity loss of only 1 %–2 % after the same number of cycles. Interestingly, cells containing anodes without SBR and thus with very low adhesion yield superior performance. Contrary to expectations regarding an eventual roll-over effect after prolonged cycling, cells including anodes based on low SBR fraction exhibit remarkable cycling stability, suggesting mechanical integrity even in complete absence of SBR. Evidently, 2 wt% CMC or additional low SBR content is sufficient to compensate for the mechanical stress in the anode due to volume fluctuations during cycling. Presumably, in addition to elevated internal cell resistance cells comprising high SBR fractions could undergo accelerated capacity loss due to electrochemical isolation of active material particles at contact points with SBR, which swells poorly in the electrolyte [132,133]. This effect may be especially pronounced for higher mass loadings.

A similar trend is observed for cells with 10.1 mg cm^{-2} anodes (Figure 3.5 (d)). Significantly notable is the discernible discrepancy in the absolute initial discharge capacity between cells containing anodes with 4.5 % SBR, which stands at approximately 30 mAh, and other cells with absolute capacities spanning from 40 to 48 mAh. This behavior can be attributed to an elevated inherent resistance of cells, inducing premature reaching of lower cell voltage limit during discharge at high C-rates and subsequently reducing initial discharge cell capacity. Accordingly, anodes with the highest SBR concentration were not discharged as deeply as cells with the other anodes, thus protecting themselves from irreversible capacity loss (see plateauing of absolute capacity over the number of cycles). This goes hand-in-hand with the stronger capacity fading of cells with low SBR content (high absolute cell capacity) as the depth of discharge is greater than for cells with low SBR content within the anode. The high C-rate was applied to collect more cycle data over time. Here, the high C-rate applied on the 10.1 mg cm^{-2} anodes was too high to sufficiently cycle all cells within the full dis/charge window. Since slow cycling has little resistance effect on the cell, within the check-up cycle 0.1C discharge C-rate was applied every 200 cycles. One can observe (Figure S3.12), that a similar capacity decay is observed for cells with SBR content of 0, 1.5 and 3 % SBR. The cells with high SBR content show higher capacity retention, again, due to the low depth of discharge during cycling protecting from more severe ageing.

At intervals of 200 cycles, a check-up cycle was performed to assess the direct current inner resistance (DCIR) at different SOCs. Figure S3.13 (Supplementary) illustrates the evolution of DCIR induced by long-term cycling in cells with 5.7 mg cm^{-2} anodes containing varying SBR content. DCIR of all cells increases upon cycling, as expected. However, there is an exception for cells with 4.5 % SBR, as they exhibit a decreasing resistance after 200 cycles. Additionally, these cells also show the highest absolute resistance, due to the highest content of inactive material. Based on DCIR data of cells at 10 %, 50 %, 70 % and 90 % SOC the internal resistance slightly decreases with increasing SOC. Overall, DCIR values are similar for cells with 0, 1.5 and 3 % SBR. For the cells with 10.1 mg cm^{-2} anodes a more distinct trend is observed (Supplementary Figure S3.14). Clearly, the lower the SBR content the lower the

internal resistance values at SOC 30, 50, 70 and 90 %. At SOC 10 % no real trend can be seen, however the resistances are 2.5-fold higher than for the other SOCs and increase with a much greater slope over the number of cycles.

3.3.8. Post-mortem analysis

Prior to post-mortem analysis pouch cells were fully discharged at 3.0 V including a CV-phase for 4 h to ensure complete delithiation of the anodes. After cell disassembly, anodes and separators were examined optically for cycle-induced morphological alterations. Lithium plating can be identified on the separators (black dots) and especially on the edges of the anodes (silver-grey deposits) (Figure 3.6). This phenomenon is more pronounced for anodes with higher mass loading (Supplementary Figure S3.15). Additionally, for 5.7 mg cm^{-2} anodes there is a noticeable tendency towards greater lithium deposition with higher SBR content. The lithium plating phenomenon might indicate increased electric resistance of the graphite coating.

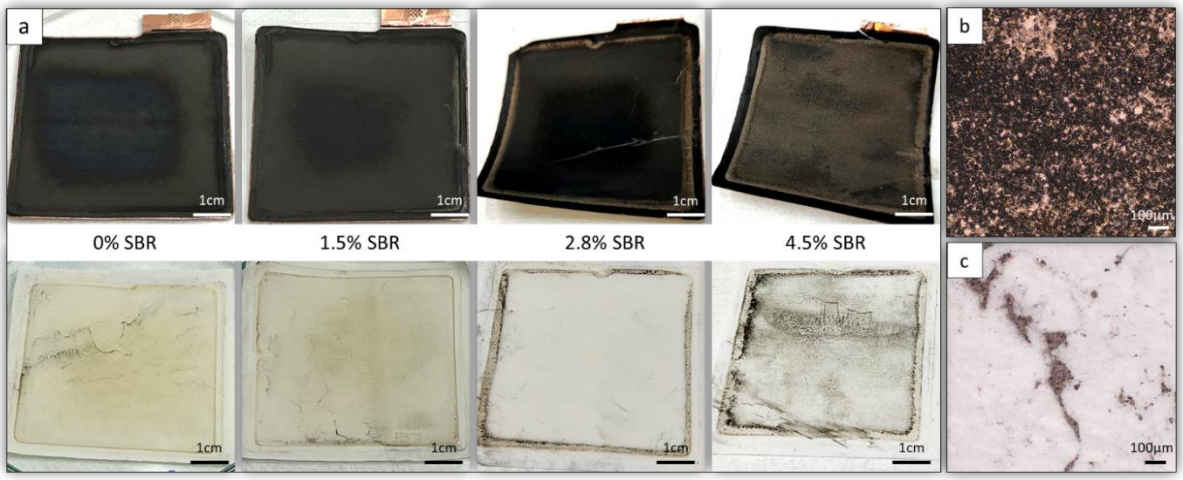

Figure 3.6. (a) Disassembled 5.7 mg cm^{-2} (2.15 mAh cm^{-2}) anodes with different SBR concentrations (upper row) and corresponding separators (bottom row); microscopic images of anode (b) and separator (c) with visible lithium plating.

To gain further insights into the morphological changes of the anodes occurring during cycling, the negative electrodes were examined using SEM. Figure 3.7 illustrates SEM images of anodes with higher mass loading before and after cycling. A crust-like deposit with globular structures covering graphite particles can be observed on the surface of the cycled anodes, which is reported to be the characteristic morphology of the solid-electrolyte interphase (SEI) when $LiPF_6$ salt and carbonate solvents are used as the electrolyte [135]. However, the SEI layer is inhomogeneous and non-uniformly distributed, which is more evident as the SBR concentration increases. This allows us to hypothesize that the SBR concentration may influence the

SEI formation, which is also postulated in sparse literature [136]. SBR may degrade during prolonged cycling and the resulting decomposition products may react with the electrolyte, contributing to the formation of additional SEI. Another reason could be the relatively low electrolyte permeability of CMC/SBR, especially at higher mass loadings [137], such that the surface of the graphite particles at increased amounts of SBR may not have sufficient contact with the electrolyte to form a uniform and robust SEI layer. However, both theories require further research to be validated.

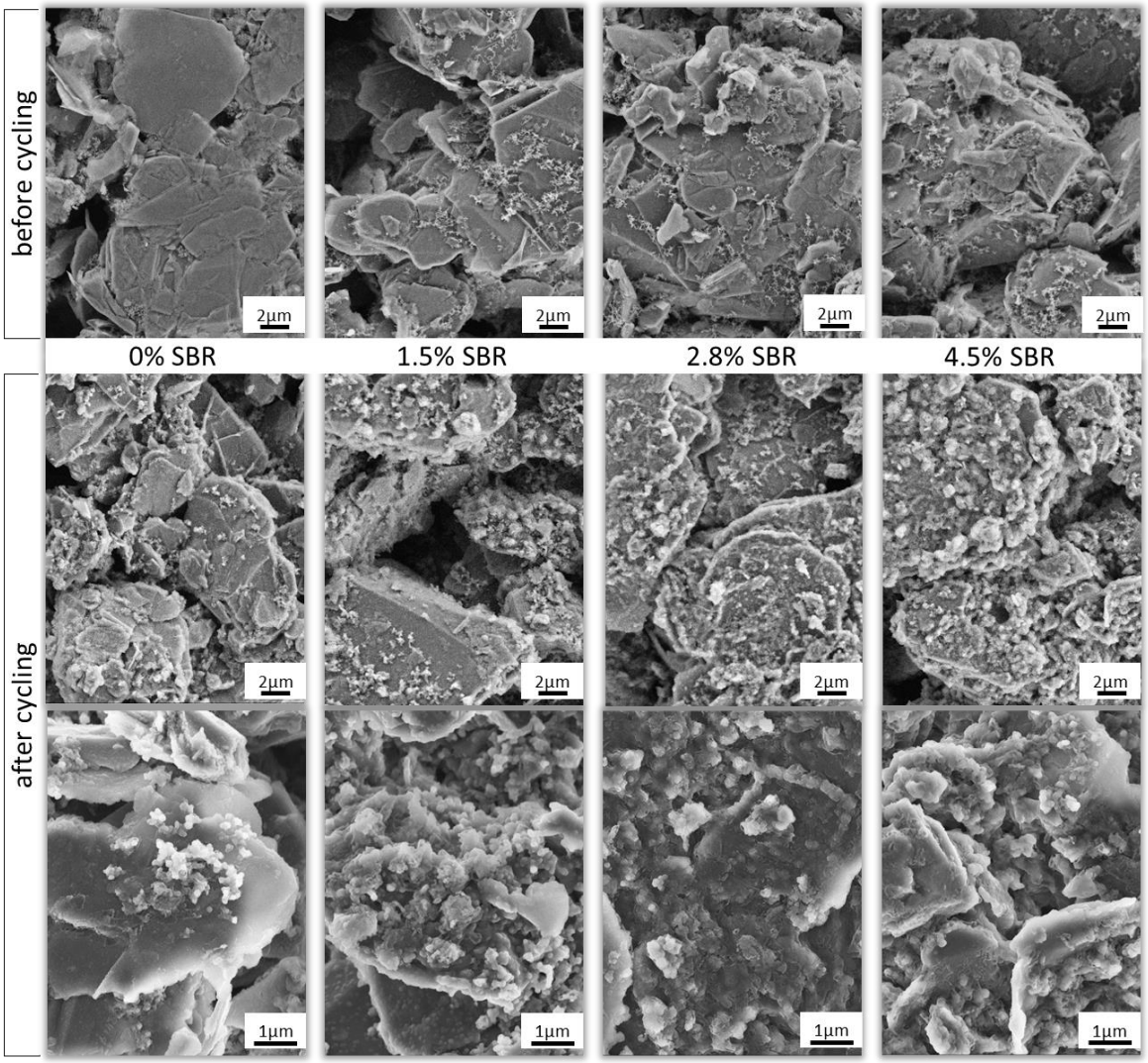

Figure 3.7. SEM images of 10.1 mg cm^{-2} (3.50 mAh cm^{-2}) anodes with different SBR concentration before and after 2500 cycles.

To investigate the effect of cycling on the anode adhesion, the cycled negative electrodes were rinsed with DMC, dried overnight in an oven and subjected to a 90°-peel test. A comparison of the pre- and post-cycle line loads as a function of SBR content is depicted in Figure 3.8.

The obtained results show a strong cycling-induced decrease in anode adhesion, which is independent of the initial adhesive strength and mass loading. These findings are consistent with the observations made by Dai et al. [138], who reported a progressive decrease in the adhesive strength of graphite anodes as the number of

cycles at 1C increase. This decline is likely attributed to the mechanical degradation of the binder due to the repetitive expansion and contraction of the material particles during the (de)intercalation of lithium ions in graphite. It is also possible, as mentioned above, that SBR decomposes during cycling, which in turn, would be consistent with our hypothesis posed in connection with the formation of additional SEI resulting from the reaction of SBR decomposition products with the electrolyte.

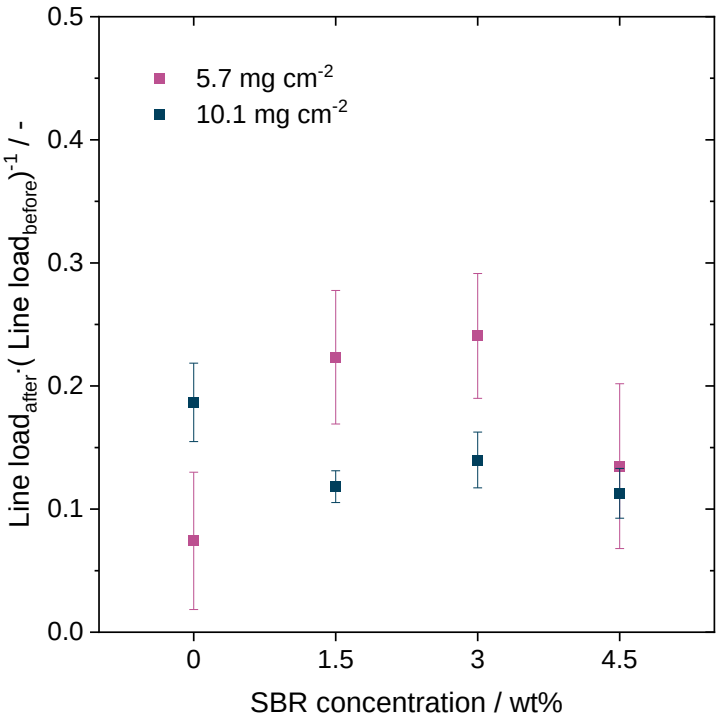

Figure 3.8. The ratio of the line load of cycled anodes and fresh calendered anodes before cycling as a function of SBR concentration and mass loading.

3.4. Conclusions

In this work, the amount of SBR in water-based anode slurries has been systematically varied to study its effect on the mechanical properties of graphite anodes, their processability and electrochemical performance at two different mass loadings (5.7 and 10.1 mg cm^{-2}).

As expected, the addition of SBR does not influence the flow behavior of anode slurries, however, the adhesion of the anode layer to the current collector increases exponentially and the compressive strength of the layer, i.e., its cohesion, increases linearly with increasing SBR concentration.

The electrodes were examined for potential mechanical failure when subjecting them to different mechanical stresses (bending, tension, compression) that commonly occur during battery manufacturing steps. No macroscopic defects were found during

bending tests on non-calendered anodes, except for the 10.1 mg cm^{-2} anodes without SBR, which demonstrated intensive crack formation. In all cases, the compressive strength of the anodes was high enough to withstand the acting bending forces, except for the thick layer without SBR, when the compressive strength was lowest and the bending force highest. During winding tests, samples experience greater stresses compared to bending and accordingly crack formation occurred regardless of adhesive strength. Higher mass loading led to more pronounced cracking. During punching and cutting, however, higher adhesion and cohesion of anode layers resulted in fewer particle abrasion and coating delamination, finally yielding higher quality edges.

The electrochemical performance of anodes was investigated in full-cell pouch configuration. 5.7 mg cm^{-2} (2.15 mAh cm^{-2}) and 10.1 mg cm^{-2} (3.50 mAh cm^{-2}) anodes were paired with NMC111 (1.75 mAh cm^{-2}) and NMC622 (3.00 mAh cm^{-2}) cathodes, respectively. The rate capability was found to decrease with increasing SBR content, particularly at higher anode mass loading. Against expectations, anodes without SBR and thus with very low adhesive strength show remarkable cycling stability. Higher SBR fractions lead to an accelerated capacity fading. Also, the higher the SBR content, the lower the absolute cell capacity, which is a result of premature shut-off during cycling due to higher internal cell resistance. The inbuilt resistance measured at different SOC shows an increase with the number of cycles and SOC. Overall, higher SBR content and higher mass loading within the anode caused greater cell capacity degradation.

Post-mortem analysis revealed deposition of lithium metal on the anode was more pronounced with increasing SBR concentration and higher mass loading. In addition, globular, crust-like deposits on the surface of anodes suggest that SBR impedes the formation of a uniform SEI. The adhesive strength of cycled anodes dropped to about 10 %–20 % of its original value irrespective of mass loading and SBR content. Post-mortem analysis suggests mechanical degradation and decomposition of SBR due to prolonged cycling. Consequently, SBR can no longer provide as high bonding between anode layer and current collector as at the beginning, before cycling. The possible polymer decomposition products may react with the electrolyte, contributing to the formation of additional inhomogeneous SEI.

Conclusively, excessively high adhesion does not confer any discernible advantages to the processability of anodes. The addition of SBR enhances the cohesive strength of anode layers, which plays a key role in withstanding external stresses, particularly at high mass loadings. However, augmented SBR concentrations lead to the deterioration of electrochemical performance of the cell, primarily attributed to elevated internal resistance and SBR degradation. In our particular case we found an optimal adhesion of non-calendered 5.7 and 10.1 mg cm^{-2} anodes at 4.6 and 5.8 N m^{-1}, respectively, corresponding to 1.5 % SBR in the anode layer.

3.5. Supplementary data

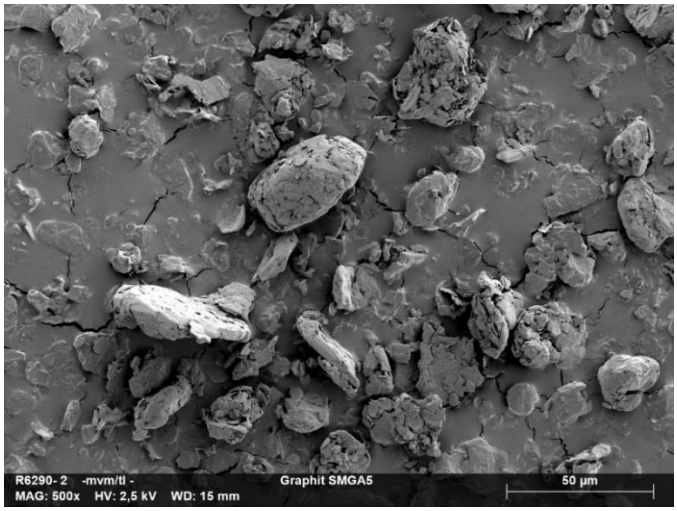

Figure S3.1. SEM image of graphite particles (SMG A5) used as active material.

Figure S3.2 (a) shows the flow behavior of anode slurries with varying SBR concentrations (0 %, 1.5 %, 2.8 %, 4.5 %). The yield stress of the anode pastes as a function of SBR content is depicted in Figure S3.2 (b).

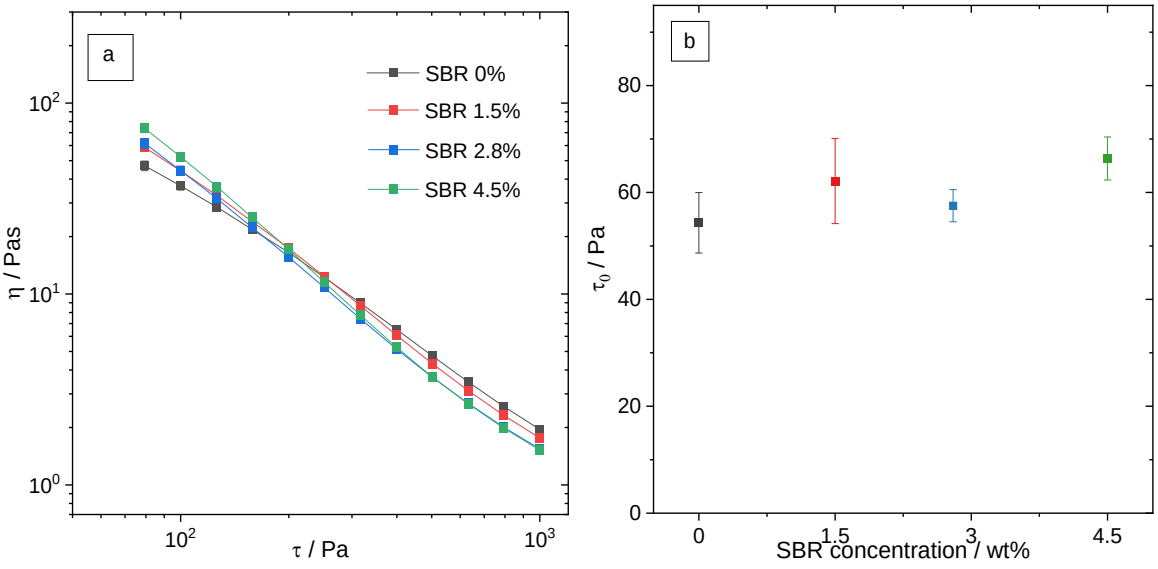

Figure S3.2. Viscosity as a function of shear stress (a) and yield stress τ_0 as a function of SBR concentration (b) for anode slurries with constant particle loading $\phi_s = 25$ vol% and varying SBR weight concentration.

Figure S3.3 illustrates a non-calendered anode containing 2.8% SBR after the winding test. Strong coating defects such as cracks and coating delamination are visible.

Figure S3.3. Non-calendered 10.1 mg cm^{-2} anode with 2.8 % SBR after winding test.

Figure S3.4 shows steel band cut calendered anodes with mass loading of 10.1 mg cm^{-2} and varying SBR concentration. Depending on the SBR concentration, differences in cut quality can be observed, which is due to the different adhesion and cohesion values of the electrodes.

Figure S3.4. Calendered punched 10.1 mg cm^{-2} (3.50 mAh cm^{-2}) anodes containing 0 %, 1.5 %, 2.8 % and 4.5 % SBR after steel band cutting.

Figure S3.5 to S3.8 show calendered and non-calendered anodes with mass loading of 5.7 mg cm^{-2} and 10.1 mg cm^{-2} and varying SBR concentration after cutting with a paper guillotine in order to prepare samples for 90°-peel-test. With increasing SBR concentration and thus improving mechanical properties of the electrodes, less particle residue and layer delamination are observed at the cut edges. This trend is more pronounced for anodes with a higher mass loading.

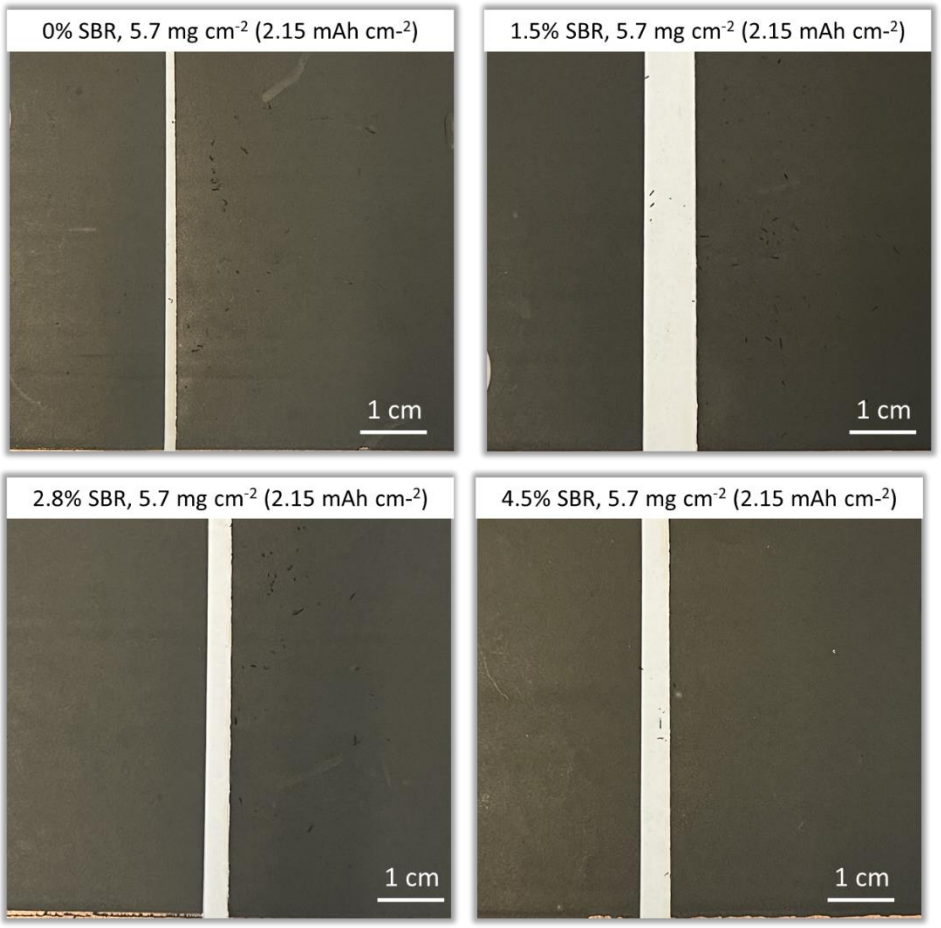

Figure S3.5. Calendered 5.7 mg cm^{-2} (2.15 mAh cm^{-2}) anodes containing 0 %, 1.5 %, 2.8 % and 4.5 % SBR after cutting with a paper guillotine.

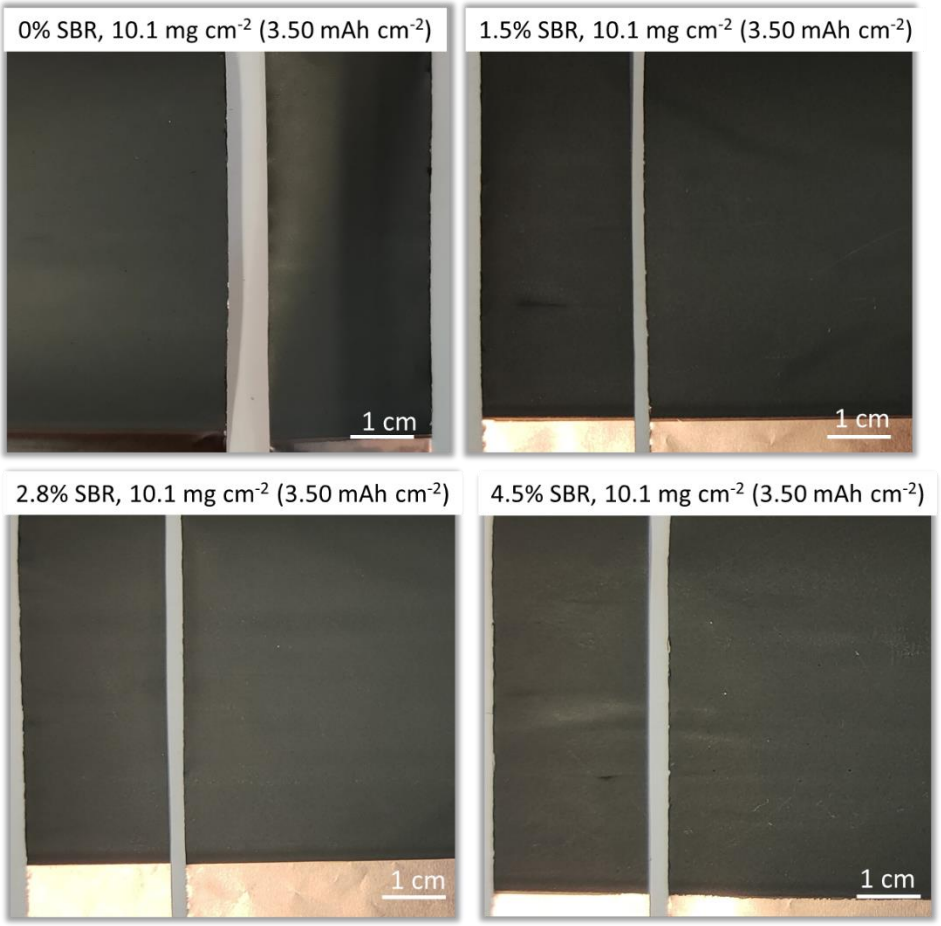

Figure S3.6. Calendered 10.1 mg cm^{-2} (3.50 mAh cm^{-2}) anodes containing 0 %, 1.5 %, 2.8 % and 4.5 % SBR after cutting with a paper guillotine.

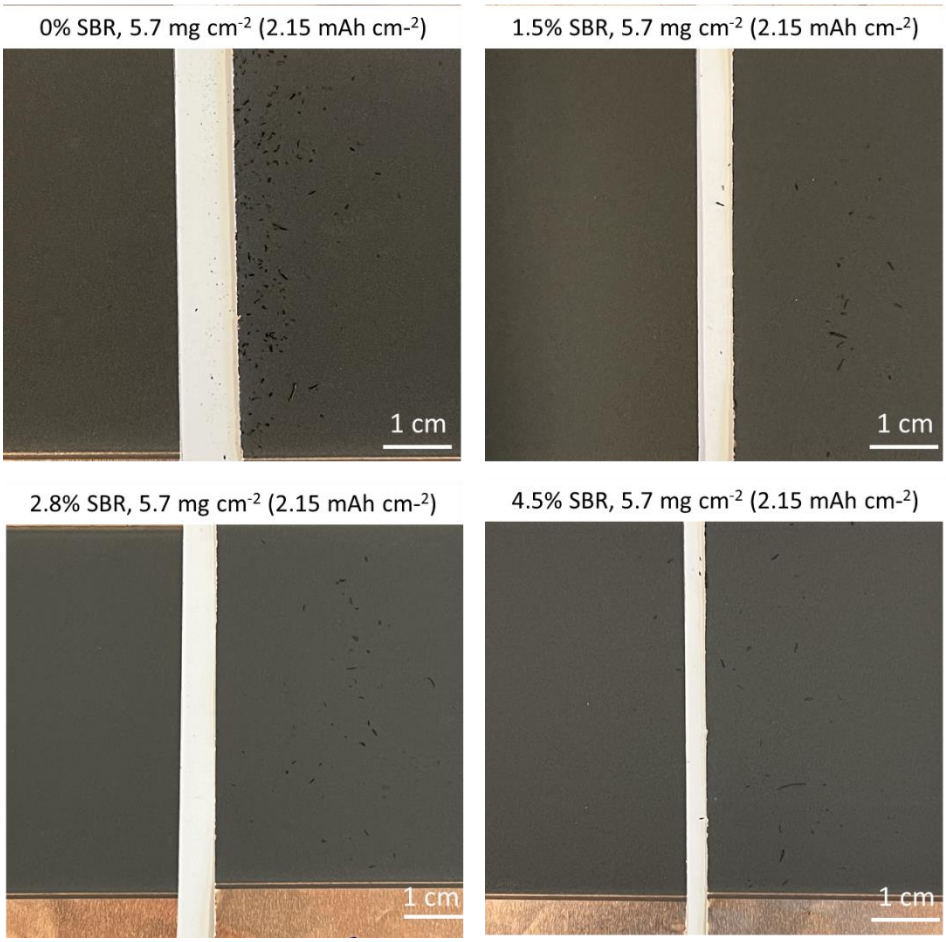

Figure S3.7. Non-calendered 5.7 mg cm^{-2} anodes with 0 %, 1.5 %, 2.8 % and 4.5 % SBR after cutting with a paper guillotine.

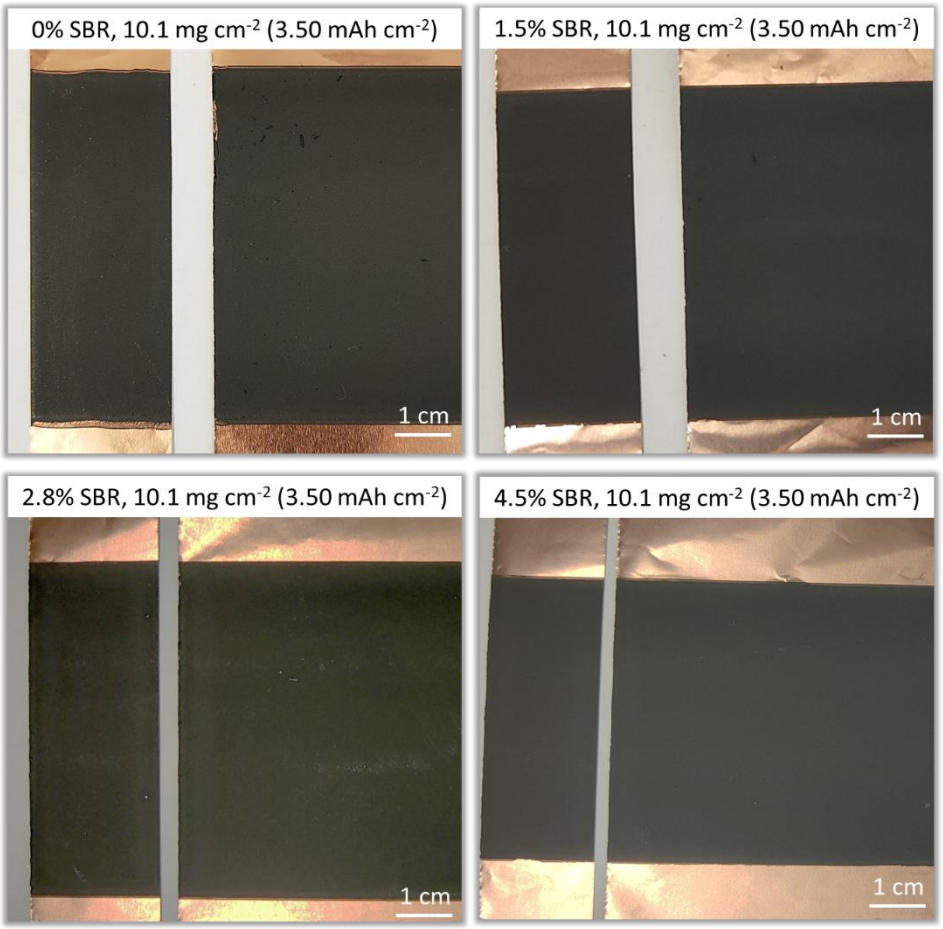

Figure S3.8. Non-calendered 10.1 mg cm^{-2} anodes with 0 %, 1.5 %, 2.8 % and 4.5 % SBR after cutting with a paper guillotine.

To obtain anodes with target areal capacities of 2.15 and 3.50 mAh cm^{-2}, anodes with different coating thicknesses were produced. Since the drying conditions were constant for all produced anodes, the coating gap directly correlates with the anode thickness after drying. Figure S3.9 displays the practical capacities of anodes with varying SBR concentration and the set coating gap determined in half-cell tests within coin cells. The capacity readings obtained from two half-coin cells of each anode composition were fitted with a linear fit.

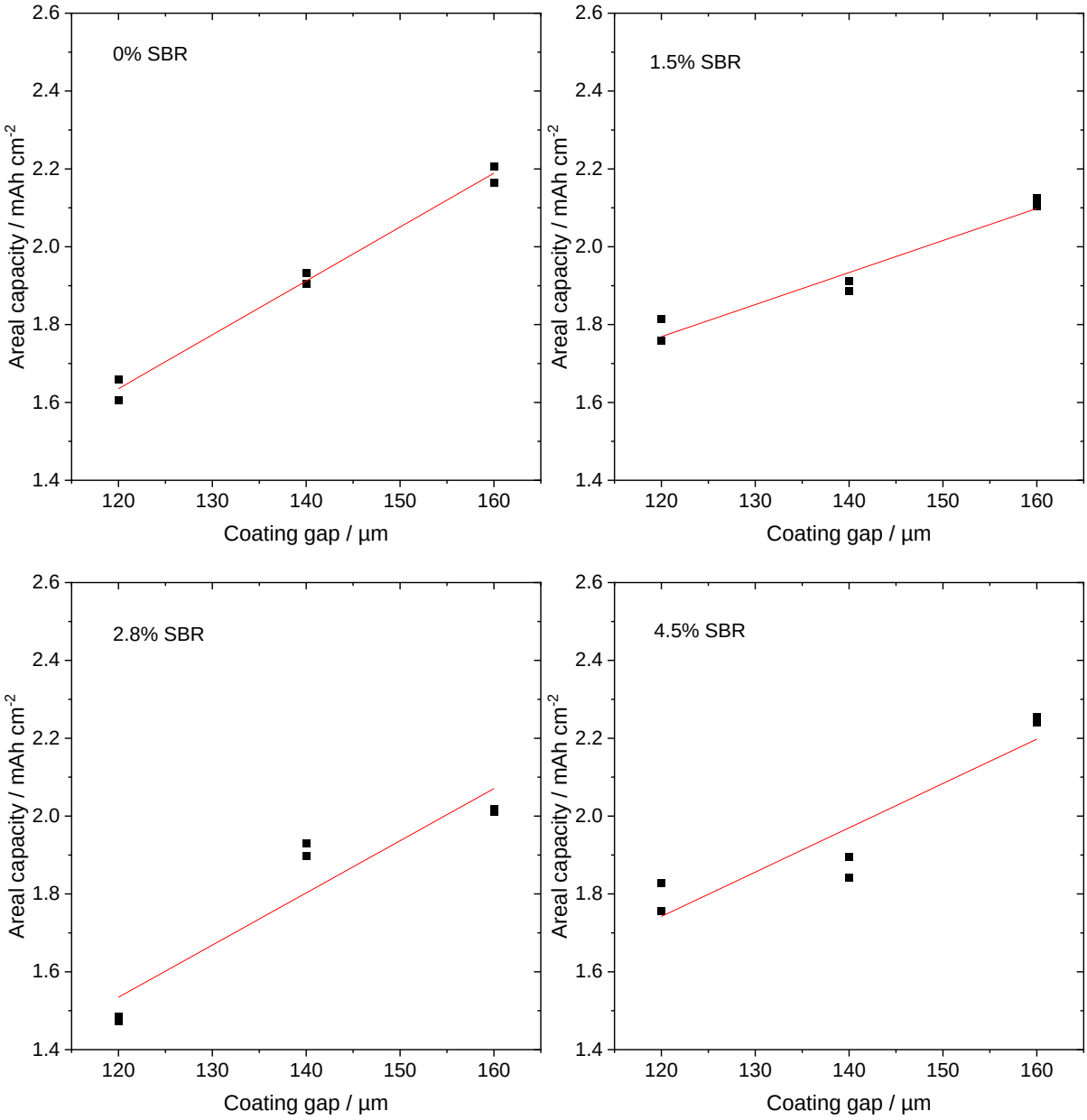

Figure S3.9. Practical areal capacity of anodes with varying SBR content as a function of coating gap. For each anode formulation, two half-coin cells were assembled and tested. The areal capacity increases almost linearly with coating gap, linear fits are shown as solid lines.

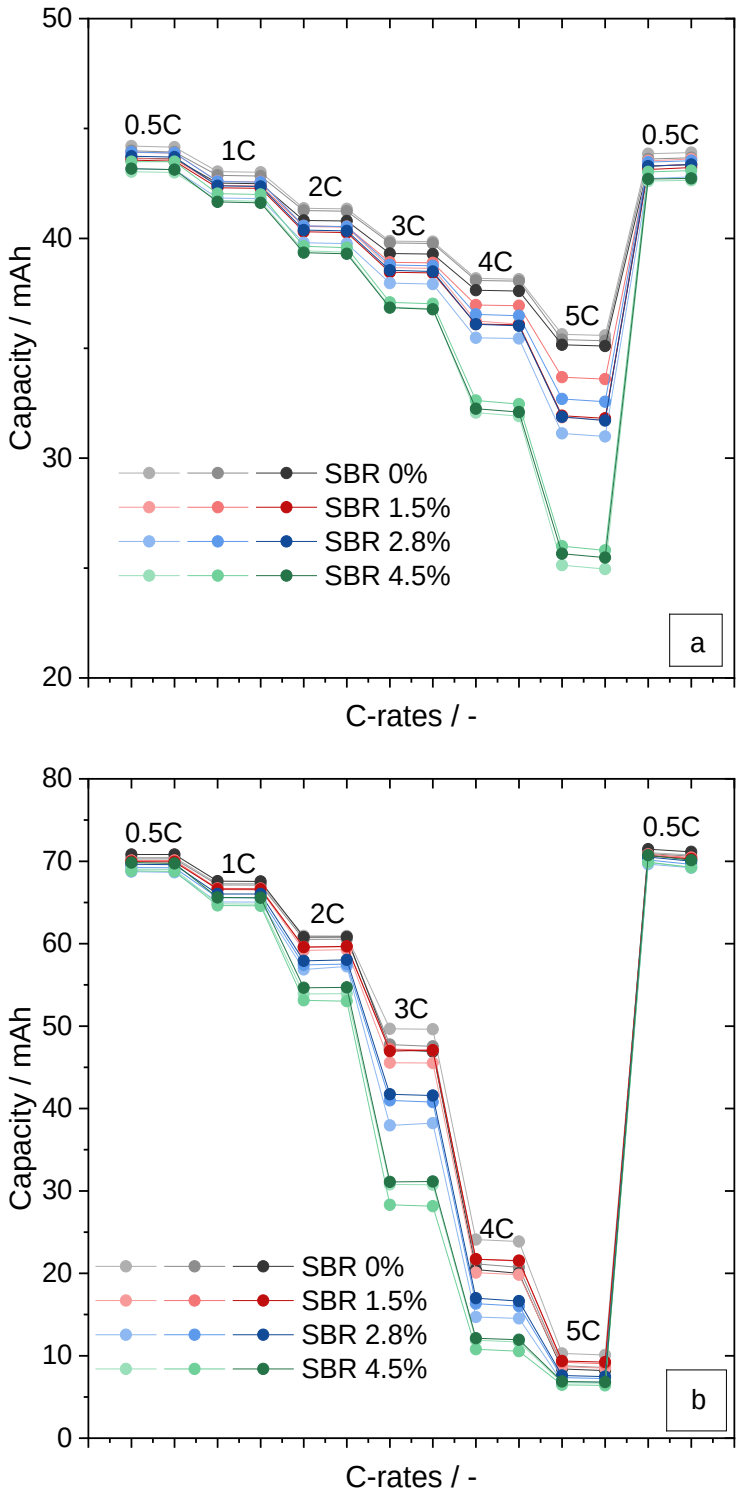

Figure S3.10. Rate capability test of pouch cells containing 5.7 mg cm^{-2} (a) and 10.1 mg cm^{-2} (b) anodes with 0 %, 1.5 %, 2.8 % and 4.5 % SBR. Absolute discharge capacity of the pouch cell against C-rate.

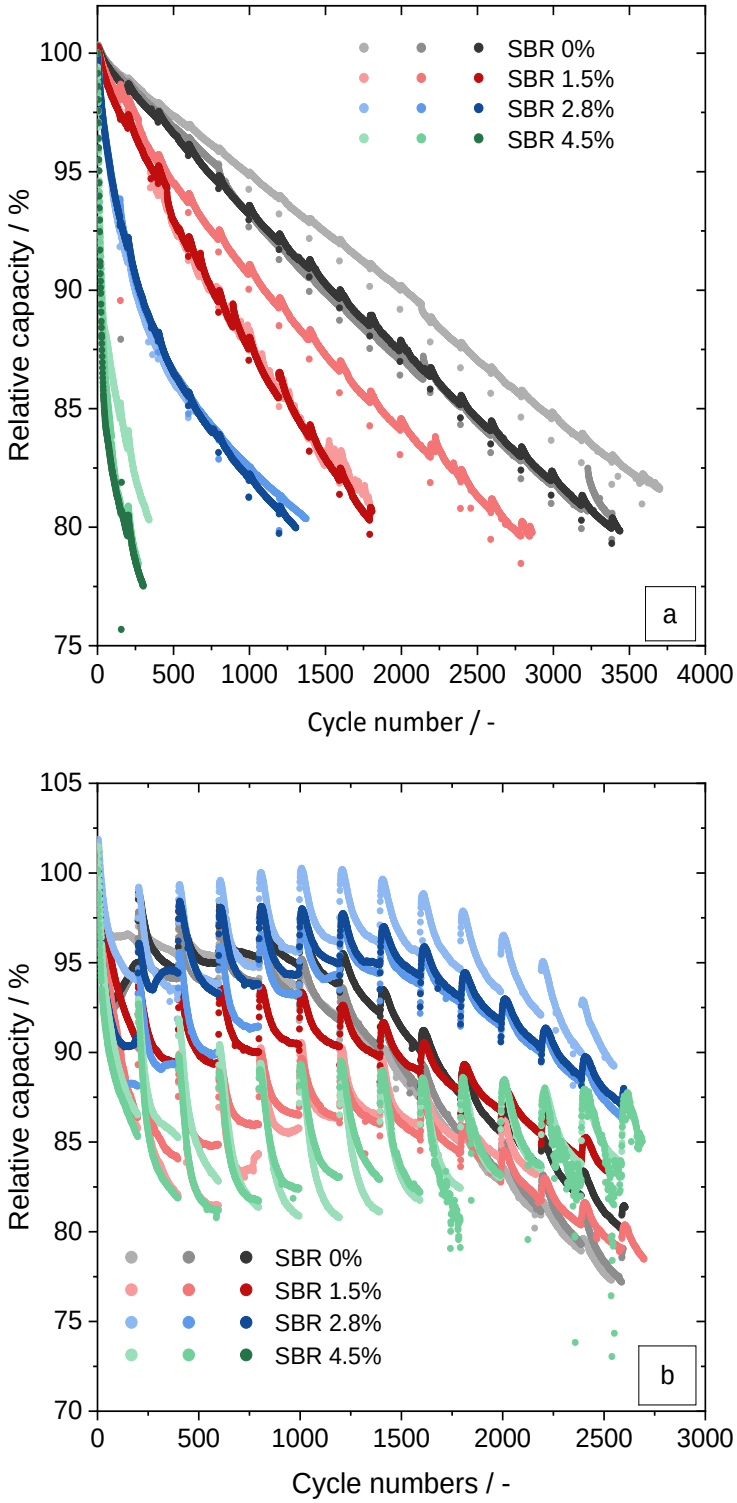

Figure S3.11. Relative capacity as a function of cycle number for pouch cells containing 5.7 mg cm^{-2} (a) and 10.7 mg cm^{-2} (b) anodes with different SBR concentrations; Three cells were tested for each anode composition.

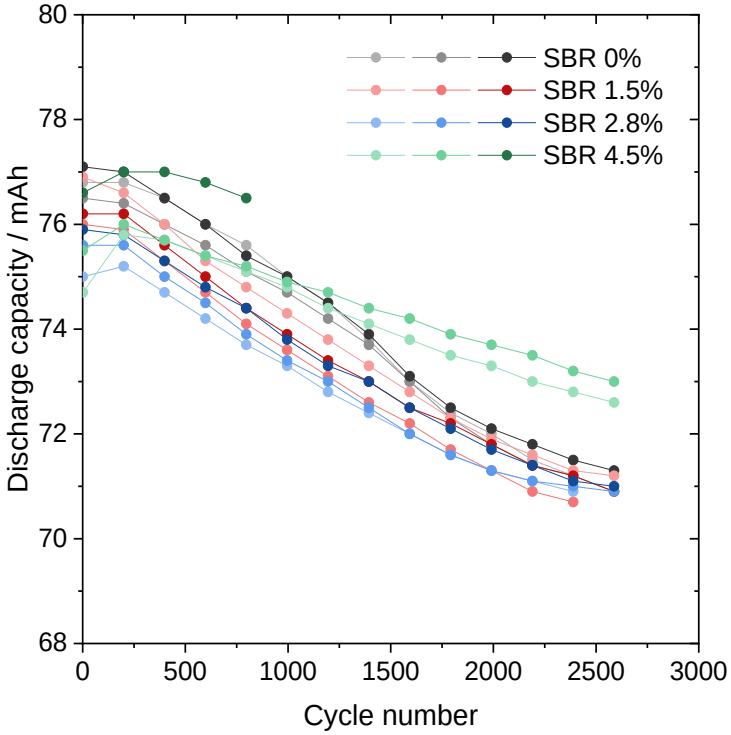

Figure S3.12. 0.1C check-up discharge capacity for pouch cells containing 10.1 mg cm^{-2} anodes with different SBR concentrations as a function of cycle number.

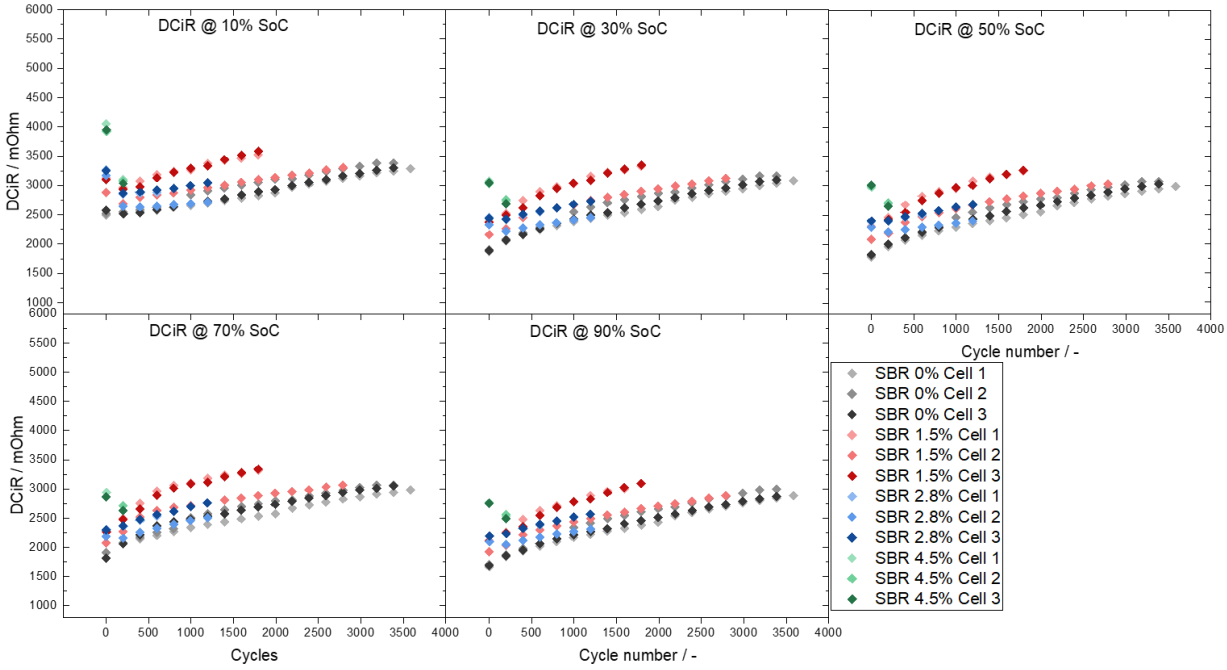

Figure S3.13. DCIR vs. cycle number at 10 %, 30 %, 50 %, 70 % and 90 % SOC for pouch cells containing 5.7 mg cm^{-2} anodes with 0 %, 1.5 %, 2.8 % and 4.5 % SBR.

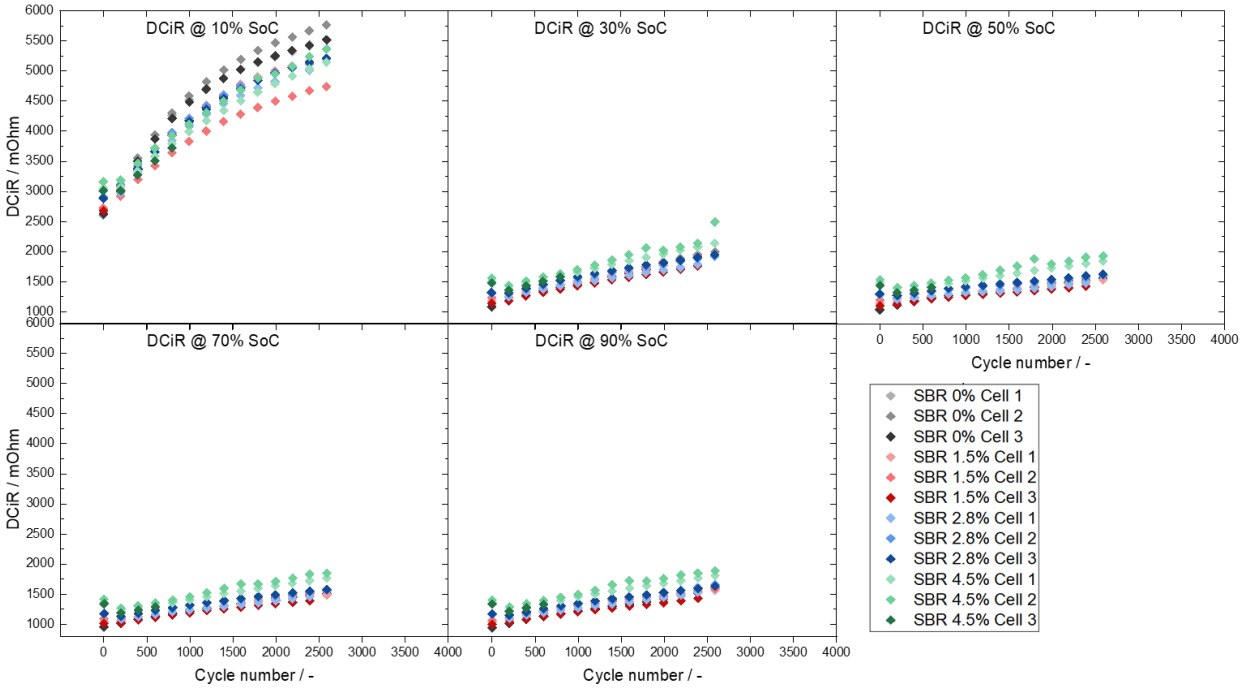

Figure S3.14. DCIR vs. cycle number at 10 %, 30 %, 50 %, 70 % and 90 % SOC for pouch cells containing 10.1 mg cm^{-2} anodes with 0 %, 1.5 %, 2.8 % and 4.5 % SBR.

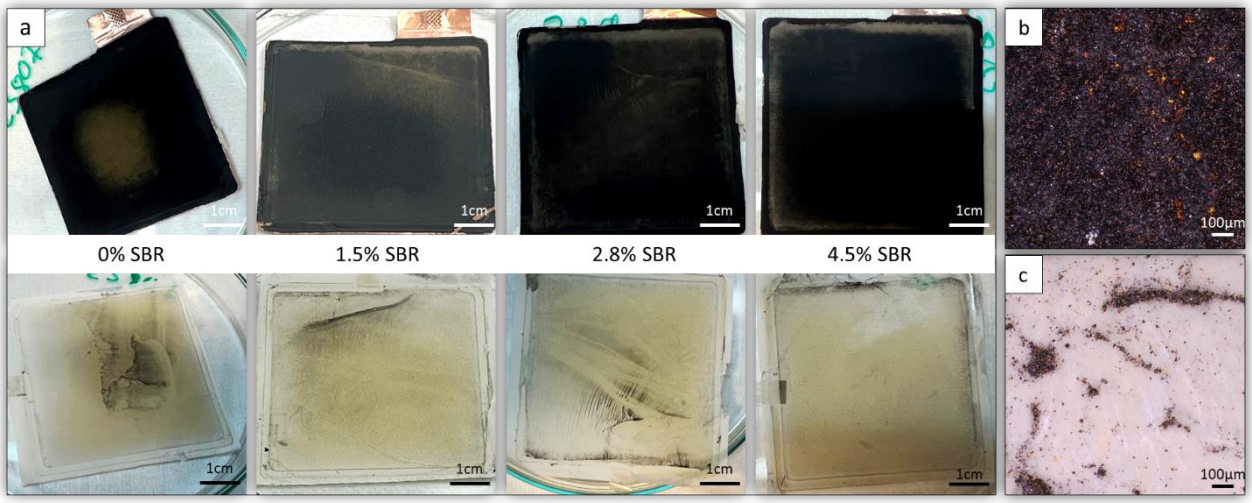

Figure S3.15. (a) Disassembled 10.1 mg cm^{-2} anodes (upper row) and separators (bottom row) with different SBR concentrations; microscopic images of anode (b) and separator (c) with lithium plating.

Figure S3.15 shows 10.1 mg cm^{-2} anodes with varying SBR concentration and separators disassembled from pouch cells after undergoing 2500 cycles. On the surface of anodes and separators we observed lithium plating, which does not seem

to correlate directly with SBR content. In the case of anodes with 4.5 % SBR, lithium deposition is not as strong as on anodes with lower SBR content, which is probably due to milder discharge conditions, as described in section 3.3.7.

The microstructure of 5.7 mg cm^{-2} anodes after long-term cycling is shown in Figure S3.16. As in the case of anodes with higher mass loading, morphological changes caused by long-term cycling are visible. Globular structures on the surface of the active material particles can be attributed as the SEI layer. With increasing SBR concentration, the SEI layer becomes inhomogeneous and more pronounced.

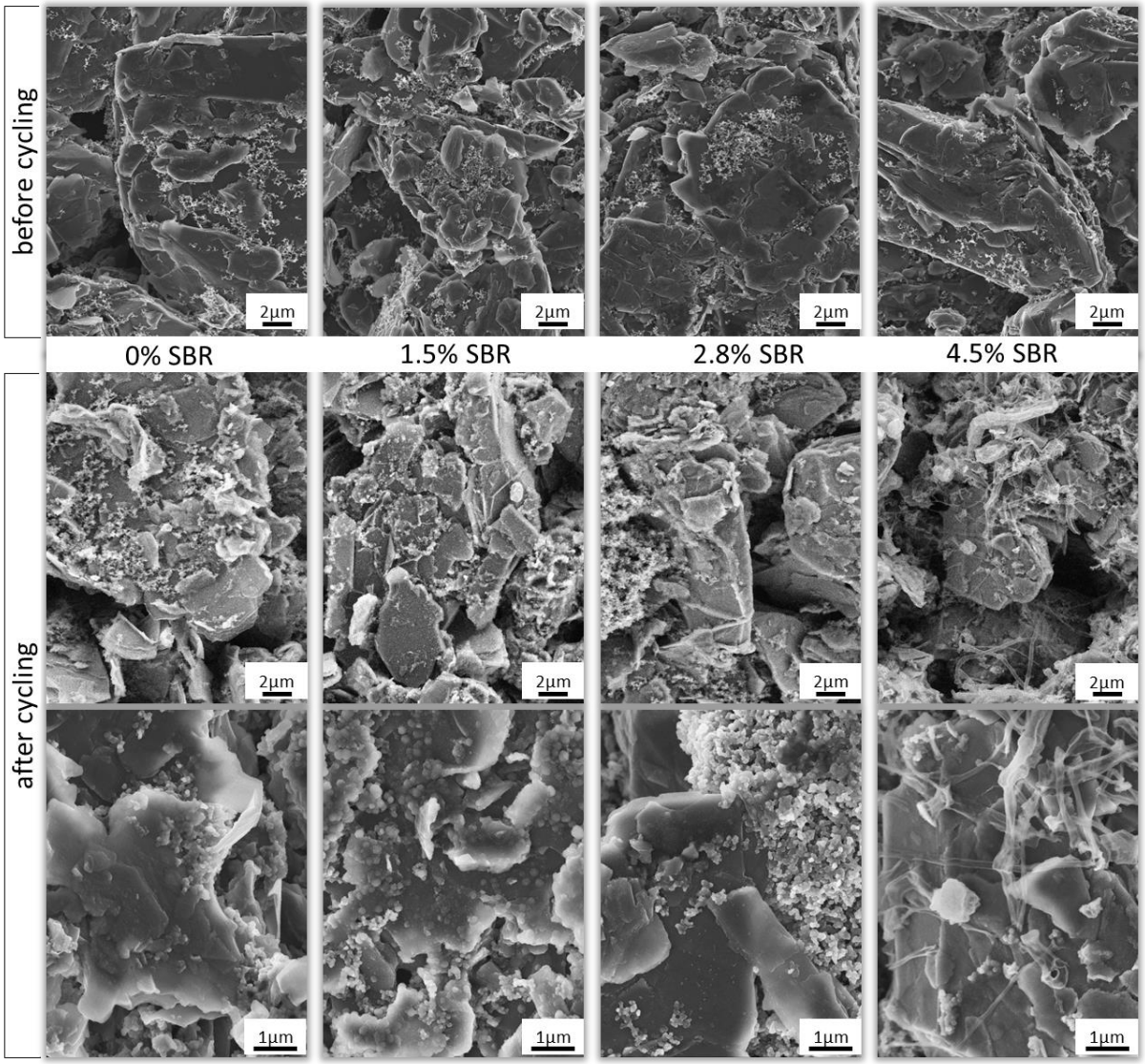

Figure S3.16. SEM images of 5.7 mg cm^{-2} anodes with 0 %, 1.5 %, 2.8 % and 4.5 % SBR before and after cycling.

4. How carboxymethylcellulose adsorption and porous active material particles diminish the adhesion of graphite-silicon anodes in lithium-ion batteries

Full title:	How carboxymethylcellulose adsorption and porous active material particles diminish the adhesion of graphite-silicon anodes in lithium-ion batteries
Authors:	Katarzyna Hofmann, Norbert Willenbacher
Status:	Published
Bibliographic data:	Energy Materials 2025, 5, 500092; DOI: 10.20517/energymater.2024.281

Abstract

Due to its adsorption on graphite and superior thickening properties, carboxymethylcellulose (CMC) is widely used as a dispersant and rheology modifier in water-based anode slurries for lithium-ion batteries. CMC also provides cohesion to the dry anode layer but exhibits poor adhesion to the copper foil necessitating the addition of styrene-butadiene rubber (SBR) as an adhesion promoter. High adhesion between the electrode layer and the current collector is crucial in electrode fabrication, especially for electrodes with higher mass loadings. In this work, we investigate how a polymeric binder, originally intended as a thickening and dispersing agent, can significantly affect the adhesive strength between the anode layer and the current collector. Our results reveal that CMC, by adsorbing onto active material particles (graphite, micro-silicon or nano-silicon), indirectly influences the anode adhesion. The adsorbed CMC layer hinders the direct binding of SBR to the active material particles, thereby creating the weakest link between the active layer and the current collector. This effect is more pronounced the higher the CMC molecular weight. Moreover, we could show that graphite-nano-silicon composite anodes exhibit a significantly reduced adhesion to the copper foil despite a low adsorption of CMC on nano-silicon, since a large fraction of SBR particles are trapped in the porous, micron-sized nano-silicon aggregates. Our findings highlight the importance of considering thickener adsorption on active material particles within electrode design, as a factor that exerts an indirect, albeit significant, influence on anode adhesion.

4.1. Introduction

By the year 2035, more than one in four vehicles is expected to be electric [139]. The leading battery energy storage technology for electric vehicles is currently the lithium-ion battery (LIB) [140]. Although this technology has been described as the key to green transformation, there are still some environmental concerns associated with the use of rare earth metals, energy-intensive production, and unresolved recycling issues. In terms of sustainability and production efficiency improvements, aqueous processing represents the state-of-the-art in anode manufacturing. Using water as a non-toxic solvent is more environmentally friendly, reduces energy consumption during the drying process, and consequently lowers manufacturing costs compared to conventional anodes formulated with organic solvents [55,71,113].

The most commonly used polymeric binder in water-based anode slurries is sodium carboxymethylcellulose (CMC), an anionic water-soluble polyelectrolyte derived from cellulose. It consists of β-glucopyranose monomers, with some hydroxyl groups replaced by carboxymethyl groups. The average number of substituted hydroxyl groups per glucose unit is defined as the degree of substitution (DS) and typically ranges from 0.6 to 1.2. A higher DS generally improves the water solubility of CMC [141,142]. CMC adsorbs onto graphite and acts as a dispersant, sterically stabilizing the active material particles [57,143]. Due to the superior thickening properties in aqueous solutions, CMC allows modulation of slurry viscosity across a wide range at relatively low concentrations, compared to other binders such as linear polyacrylic acid (PAA). Furthermore, depending on the shape of the active material particles, CMC can promote their alignment in a single direction, thereby enhancing the cohesion of the dry anode layers [62]. However, poor adhesion of CMC to the copper current collector necessitates the addition of a second polymer, most commonly styrene-butadiene rubber (SBR), which acts as an adhesion promoter, thereby ensuring a robust connection between the anode active layer and the current collector.

In an aqueous environment, such as a water-based electrode slurry, polymers may either exist as free chains dissolved in a liquid phase or undergo adsorption onto the surface of dispersed particles. In the case of unbound binders, an unfavorable migration phenomenon may occur during the drying process, resulting in binder segregation [75,76,143,144], which, in turn, directly affects the mechanical (adhesion and cohesion) and electrochemical properties of electrodes [75].

There are many theories describing the phenomenon of adhesion but the most common are mechanical interlocking, adsorption theory, and chemical bonding mechanisms [145,146]. Mechanical bonding is typical for porous materials and relies on the binder embedding into the pores of the substrate [147]. Furthermore, according to adsorption theory, adhesion occurs due to molecular contact and the resulting van der Waals forces between adhesive molecules and the substrate. Additionally, in some cases, adhesive reacts with the substrate, forming chemical bonds [145].

In our previous study [148], we demonstrated that a stable electrode layer that strongly adheres to the current collector foil and maintains high cohesion between particles plays a vital role in the electrode fabrication process, especially at higher mass loadings. This is because such anodes can withstand the stresses that occur during manufacturing steps such as winding, bending, and cutting or punching. However, the impact of adhesion on electrochemical performance is less significant, as even low adhesion levels are sufficient to maintain mechanical and electrical integrity during cell cycling. Therefore, optimizing a binder system is challenging, as it requires a comprehensive understanding of the interactions between the binder and the particles, as well as between the binders themselves.

In recent years, a significant amount of scientific effort has been dedicated to the development of multifunctional polymeric binders, particularly for silicon anodes [149–152]. These polymers have been shown to facilitate robust connection between active material particles and the current collector, while at the same time providing a flexible bond between the silicon particles. The self-healing properties of these binders enable silicon-containing anodes to withstand substantial volume changes during cycling [145], thereby contributing to their superior electrochemical performance. Xiang et al. [153] recently introduced a three-dimensional (3D) AGE binder, synthesized from guar gum (GG), gum arabic (GA) and epichlorohydrin (ECH). The formation of hydrogen bonds between the GG, GA and silicon particles strengthens the bond between the binder and the silicon active material. In addition, the spiderweb-like structure of the binder reinforces the electrode, providing structural stability and preventing degradation during cycling. Meanwhile, alternative approaches, such as multilayer coatings, are being developed to facilitate the production of electrodes with superior mechanical and electrochemical properties [154–156]. This method enhances the effective utilization of polymeric binders, simultaneously enabling a reduction in their content. The present study investigates the combination of commercially available CMC and SBR binders, which, with their distinct functionalities, represent a state-of-the-art binder system for aqueous-processed graphite and silicon-containing anodes.

It has been demonstrated that CMC is incapable of enhancing electrode adhesion. Gordon et al. [62] showed that for graphite electrodes with CMC as binder only, the adhesion strength is weak, independent of CMC concentration, DS, and molecular weight (M_w). There are studies in the literature investigating the adsorption behavior of CMC on both graphite [57,125,157] and silicon [59,158–160] active materials. Several groups have reported a correlation between the amount of CMC adsorbed on active material particles and the adhesion strength of anodes. Kim et al. [161] in their investigation into the use of different binders for silicon anode slurries demonstrate that there is an inverse correlation between the polymer adsorption and adhesion strength of anodes prepared with CMC and SBR at pH 7. Haberzettl et al. [162] examined the impact of the energy input within the mixing process of silicon-graphite anode slurries. Similarly, it was observed that corresponding electrodes with the highest amount of CMC adsorbed on the active material particles exhibited the

lowest adhesion. Nevertheless, neither study attempted to provide an explanation for this phenomenon.

In this work, we elucidate how a polymeric binder, originally intended as a thickening and dispersing agent, can have a significant impact on the strength of electrode adhesion. The main objective of this study is to understand how the adsorption behavior of CMC on active material particles affects the adhesive strength of aqueous-processed LIB anodes. This investigation is conducted for graphite and silicon-graphite electrodes to identify potential formulation improvements, ultimately contributing to more efficient and durable energy storage solutions.

4.2. Experimental

4.2.1. Materials

Surface-modified natural graphite (Gr, SMG A5, Showa Denko Materials Co, Ltd., Japan) and two different types of silicon powder: micron-sized crystalline silicon (Silgrain® e-Si 410, Elkem, Norway) and nano-sized polycrystalline silicon (Nanostructured & Amorphous Materials Inc., USA) were used as anode active materials (AMs) in this study (Figure S4.1). A volume-based average diameter and a Brunauer-Emmett-Teller (BET) surface area are 17.8 µm and 3.0 $m^2 g^{-1}$ for graphite, 3.3 µm and 3.2 $m^2 g^{-1}$ for micro-silicon, 100 nm and 56.4 $m^2 g^{-1}$ for nano-silicon. Carbon black (CB, C-Nergy Super C65, Imerys Graphite & Carbon, Switzerland) with an average primary particle size of 32 nm was used as a conductive additive in anode slurries. Both nano-Si and CB particles in aqueous suspensions tend to form agglomerates with an average size of approximately 5 µm.

Three polymers were used for the study: sodium CMC (TEXTURECEL, DuPont, USA) with a DS of 0.7 and three different M_w of about 150 kDa, 700 kDa and 1200 kDa, polyethylene oxide (PEO, Sigma Aldrich, Germany) with a M_w of 1000 kDa, and styrene butadiene rubber (SBR) in the form of 48 wt% (TRD 2001, JSR, Japan) aqueous dispersion of nanoparticles.

4.2.2. Sample preparation

SBR adhesion

The adhesion of SBR to four different substrates was examined. For this purpose, a polished graphite plate with the dimensions of 100 × 50 × 10 mm (EXC, Graphite24.com GbR, Germany) and a polished quartz glass plate measuring 139 × 102 × 3 mm (EN08NB, GVB GmbH, Germany) were used as equivalent surfaces for the carbon-based anode components and silicon active material, respectively. Three-dimensional-printed frames (40 × 80 mm) were attached to the

substrates using double-sided adhesive tape. Subsequently, SBR suspension was poured in and left to dry at room temperature for at least 14 days. Once the samples were dry, the frames were removed. To suppress the elongation of the polymer film during the peel test, duct tape (4615, tesa SE, Germany) was applied to the SBR surface and the samples were cut to a width of 25 mm. To determine the adhesion between SBR and CMC, SBR suspension was poured onto glass plates with 3D-printed frames (125 × 60 mm) and left to dry at room temperature for approximately 14 days. The dry SBR film was then cut into samples of 29 mm in width and removed from the glass plate. In the next step, a 2.4 wt% CMC solution (700 kDa) was poured onto glass plates with 3D-printed frames (125 × 60 mm) and dried in an oven at 40 °C for approximately three days. Lastly, when the CMC film was only slightly damp, the cut SBR film was positioned on top of the CMC film and weighed down. The sample was then left to dry at room temperature until it was completely dry according to gravimetric verification. Finally, the duct tape was applied to the SBR surface and the sample was then cut to a width of 25 mm. In order to ascertain the adhesive strength between SBR and copper foil, an SBR emulsion was coated with a doctor blade (ZUA 2000, Zehntner GmbH, Switzerland) on a copper foil with a thickness of 10 µm. The coating gap was set at 300 µm resulting in a dry SBR film of about 120 µm thickness. The samples were allowed to dry for approximately four days at room temperature.

CMC adsorption

The CMC powder was dissolved in distilled water by stirring with a propeller at 800 rpm for 30 min to prepare CMC solutions. The particle suspensions were prepared by dispersing an appropriate quantity of AM powder in 0.1 vol% CMC solution. Graphite and micro-Si particles were dispersed using a SpeedMixer (DAC 150.1 FVZ, Hauschild, Germany) at 2000 rpm for 2 min, followed by a further 10 min in an ultrasonic bath (RK106, Bandelin Electronics, Germany). As the nano-Si particles could not be sufficiently dispersed using the aforementioned method, a dissolver stirrer was applied at 1200 rpm for 10 min. The pH of the CMC/particle suspensions was observed to range from 7 to 8. After about 30 min, the samples were centrifuged (Eppendorf 5430, Germany) until a transparent supernatant was obtained. In addition, a blank sample was included for each CMC/particle combination to assess whether the sample preparation, including mixing and centrifugation, influenced the properties of the CMC solution (e.g., potential breaking of polymer chains). Following centrifugation, a transparent supernatant was carefully separated from the sediment and taken for further investigation.

Anode preparation

In the first step, a CMC or PEO solution was prepared by dissolving CMC or PEO powder in 95 % of the total amount of distilled water by stirring with a propeller (55 mm in diameter) at 1200 rpm for 30 min. The final concentrations of CMC and PEO

solutions were 1.2 wt% (0.8 vol%) and 2.9 wt% (2.6 vol%), respectively. In the subsequent step, the propeller was replaced with a dissolver (50 mm in diameter) and CB was added to the polymer solution. Subsequently, the mixture was stirred at 2000 rpm for 5 min. In the case of silicon-containing slurries in which 20 % of the mass of graphite was replaced with silicon, the silicon was added initially, followed by the graphite. The mixture was then stirred for 5 min for each component. For slurries comprising solely graphite, the graphite powder was stirred for 10 min, thus ensuring uniformity in the total stirring time across all slurries. Subsequently, the SBR suspension was introduced, followed by the addition of the remaining 5 % of distilled water and stirred for 5 min each. All slurries had a solids content of 42 wt% (25 vol%). Following the mixing process, the slurries were degassed in a desiccator and coated on a 10 µm thick copper foil (SE-Cu, Schlenk Metallfolien GmbH & Co. KG, Germany) using a doctor blade (ZUA 2000, Zehntner GmbH, Switzerland). The coating velocity was set at 10 mm s^{-1} and the coating gap at 100 µm. Subsequently, the anodes were subjected to a drying process at 70 °C for 30 minutes. The dry electrodes, comprising CMC/SBR, contain 93.5 wt% of active material, 1.9 wt% CB, 1.7 wt% CMC and 2.9 wt% SBR. The dry electrodes comprising PEO consist of 91 wt% active material, 1.9 wt% CB, 4 wt% PEO and 2.8 wt% SBR. The anode thickness after drying was approximately 65 ± 2 µm.

4.2.3. Methods

CMC adsorption

A rheological approach was employed to investigate the adsorption of CMC on three distinct types of active material across a series of volume ratios (R) of AM to CMC (R = 1, 3, 5, 7, 10, 15). The initial CMC concentration was maintained at 0.1 vol% for all suspensions, while the particle amount was varied. Initially, the zero-shear viscosities of CMC solutions with volume concentrations of 0.01 vol%, 0.02 vol%, 0.04 vol%, 0.06 vol%, 0.08 vol%, and 0.10 vol% were determined to establish calibration curves, illustrating the relationship between zero-shear viscosity and CMC concentration for each M_w of CMC. Subsequently, the zero-shear viscosities of the mother CMC solutions used to prepare the polymer-particle suspensions, and CMC solutions after adsorption (supernatants) were determined. This enabled the calculation of corresponding CMC concentrations. By comparing the CMC concentration before and after adsorption, the volume of adsorbed CMC was quantified. The flow curves were measured with a stress-controlled rotational rheometer (Physica, MCR 501, Anton Paar GmbH, Germany) with a concentric cylinder geometry (C-CC27/ T200/SS) in a logarithmic shear rate ramp (10 points per decade) in the range $\dot{\gamma} = 1 – 1000$ s^{-1} and in a logarithmic time scale t = 30 – 10 s. All measurements were conducted at a constant temperature of 20 °C.

Adhesion

We performed 90°-peel tests to determine the adhesive strength of electrode samples (prepared as described in the section 4.2.2 *Anode preparation*) and SBR films coated on various substrates (prepared as described in the section 4.2.2 *SBR adhesion*). A universal testing machine (Texture Analyser TA.XT plus, Stable Micro Systems, UK) with a load cell of 5 kg (for electrode samples) and 50 kg (for SBR films-substrate samples) was utilized. The specimens were affixed to the movable plate using a double-sided adhesive tape and peeled off at a constant velocity of 5 mm s^{-1}. The recorded force was normalized to the sample width to obtain the line load, which was used as a measure of adhesion. At least ten electrode samples of a single formulation and three SBR-substrate samples for each combination were tested. The measured forces for each set of samples were then averaged, and the resulting mean and the standard deviation were calculated. These latter values were then represented graphically as error bars.

Determination of the amount of SBR residue in Si sediment

Nano-Si and micro-Si powders were added to a dilute SBR emulsion and dispersed in an ultrasonic bath for 15 min. The suspensions with a particle concentration of 1.6 wt% and a silicon-to-SBR mass ratio of 5 were subjected to centrifugation. The sediment was then washed three times with distilled water and dried at 60 °C until it was completely dry according to gravimetric verification. The same procedure was carried out on silicon suspensions without SBR to estimate the mass of the oxidation layer. The dried sediments were weighed and the percentage of SBR retained in the sediment was calculated.

4.3. Results and discussion

4.3.1. Adhesion of SBR films to anode components

This section presents an examination of the adhesive strength between SBR films and substrates representing anode components. The results were obtained from 90°-peel tests conducted on samples of bulk materials. For this purpose, a quartz glass plate served as an equivalent surface for the silicon active material, whereas a graphite plate represented the carbon-based anode components, including both graphite and CB.

Figure 4.1 illustrates that SBR adheres with varying strengths to different materials, exhibiting the highest adhesion to graphite (SBR@Gr: 7738 ± 781 N m^{-1}) and quartz glass (SBR@SiO_2: 1963 ± 466 N m^{-1}) surface. The lowest interfacial strength, by far, occurs between SBR and CMC at just 291 ± 86 N m^{-1}, which is

approximately 37 % of the adhesion strength between SBR and copper foil (SBR@Cu: 819 ± 47 N m^{-1}).

The results of the peel tests can be interpreted considering the surface energy of the involved materials. Adhesion failure is governed by the energy per unit area required to create a new surface and hence induce separation [163]. The low adhesion between SBR and CMC is attributed to the significantly lower surface energies of polymers, typically ranging between 20 mJ m^{-2} and 40 mJ m^{-2} , in comparison to the considerably higher values exhibited by copper (1,360 mJ m^{-2}), graphite (1,250 mJ m^{-2}), and quartz glass (980 mJ m^{-2}) [164,165]. Consequently, a substantially lower peel force is required to remove the SBR film from a CMC surface compared to the other high-energy surfaces analyzed in this study.

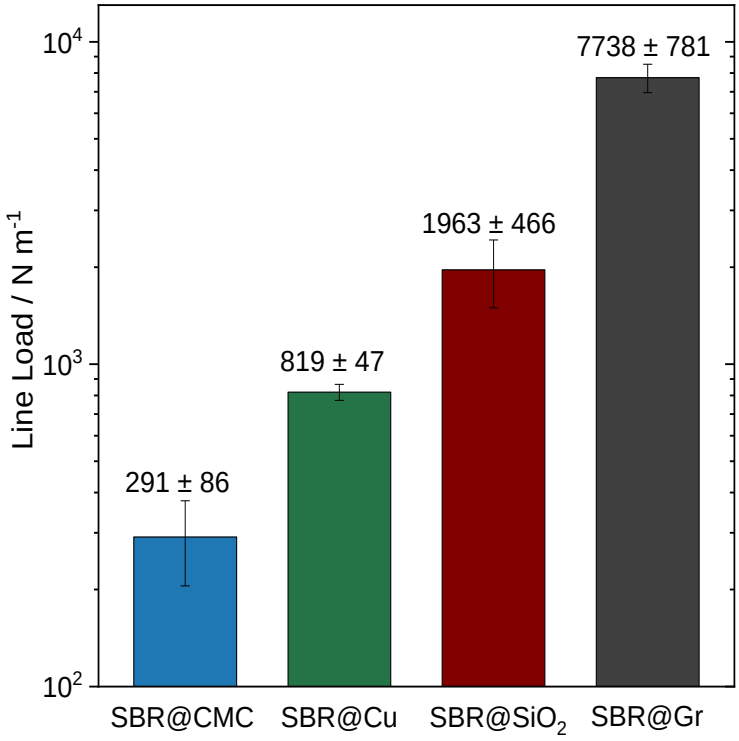

Figure 4.1. Line load as a measure of adhesion strength for SBR film on CMC film (SBR@CMC), copper foil (SBR@Cu), quartz glass (SBR@SiO_2), and graphite plate (SBR@Gr). Error bars in black represent the standard deviation calculated from measurements with at least three SBR-substrate samples.

Despite the highest surface energy values of copper of all substrates tested, the adhesion of SBR to copper is lower than to graphite and quartz glass. This finding may presumably be ascribed to the porosity of the graphite plate, which allows additional mechanical interlocking of the SBR molecules, resulting in high adhesion values. Whereas, the lower SBR adhesion to copper than to quartz glass may be attributed to possible impurities present on the surface of copper foil and lowering its surface energy [166].

The implementation of these results at the electrode level reveals two key insights. Firstly, adding SBR is essential for ensuring a strong connection between the anode active layer and the current collector, since CMC exhibits even two orders of magnitude lower adhesion to the copper foil (2.3 ± 0.7 N m^{-1} [149]) compared to SBR. Secondly, given that the interfacial strength between SBR and CMC is significantly inferior to that of the bond between SBR and copper foil, it is highly probable that delamination of the anode layer will occur at the SBR-CMC interface. The data from the existing literature demonstrate that the CMC adsorbs on both graphite [125,157,167] and silicon [159–161] surfaces. Given the poor bonding between CMC and SBR, we postulate that the adsorbed CMC layer on active material particles may act as a barrier, thereby reducing the overall electrode adhesion.

4.3.2. CMC adsorption on active materials

To further investigate the impact of the adsorbed CMC layer on the electrode adhesive strength, measurements were conducted to characterize the CMC adsorption behavior on the AM. The polymer adsorption from a solution depends on a multitude of variables, including the concentration and chemical composition of both the polymer and adsorbent, the conformation and M_w of the polymer chains, temperature, or pH and ionic strength [168]. Since the viscosity of a polymer solution is highly sensitive to even slight variations in polymer concentration (Supplementary Figure S4.2), a rheological approach was employed in order to assess the CMC adsorption capacities of two different silicon materials in comparison to graphite. The active material particles were dispersed in a polymer solution of a known concentration, subjected to centrifugation, and the viscosity of the resulting supernatant was measured in order to determine the concentration of the CMC solution after adsorption. In commercial anodes, CMC with M_w ranging from 150 to 700 kDa is typically utilized. In the present study, the scope of adsorption investigations on active material particles was broadened by extending this range to include CMC with a M_w of 1200 Da to show the influence of this additive more clearly. Industry-relevant silicon-to-CMC volume ratios were investigated. Given the laboratory-scale volumes, the concentration of polymer mother solutions was set at 0.1 vol% (based on water), while the particle concentration was varied. The amount of CMC adsorbed from the solution is expected to increase as more particles are added to the AM/CMC suspension, due to the corresponding rise in the adsorbent's surface area. Consequently, as the *R* of AM to CMC increases, the viscosity of the supernatants converges towards the viscosity of water. This trend is observed to varying degrees for all active materials investigated in this study (Supplementary Figure S4.3). In order to facilitate a comparison of the adsorption data obtained for particles differing in surface area, the adsorbed volume of CMC was calculated and related to the area of AM, as follows:

$$v_{ads} = \frac{\left(\varphi_{CMC,0} - \varphi_{CMC}\right) \cdot V_{solvent}}{S_m \cdot m_{AM}}, \tag{4.1}$$

where v_{ads} represents the specific volume of adsorbed CMC, $\varphi_{CMC,0}$ and φ_{CMC} are volume concentrations of CMC (based on solvent) before and after adsorption, $V_{solvent}$ is the volume of water in CMC solution, and m_{AM} and S_m are mass and specific surface area (BET) of the active material.

Figure 4.2A-C depicts the specific adsorption volumes of CMC plotted against the *R* of active material to CMC. It should be noted that the adsorption data were obtained in dilute polymer solutions, and thus may not precisely reflect the quantity of CMC adsorbed in a concentrated regime, as would occur in an anode slurry. Nevertheless, as all adsorption experiments were performed in the same polymer concentration regime (dilute), the adsorption capacities of the active materials can be compared. This allows qualitative conclusions to be drawn about the adsorption behavior that would be observed in a concentrated regime.

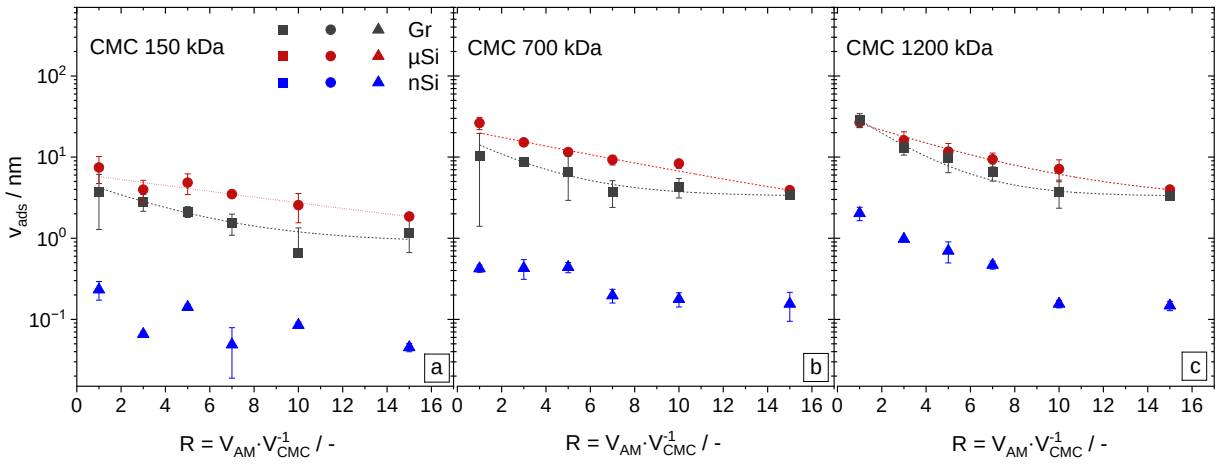

Figure 4.2. Adsorbed amounts of CMC of 150 kDa (a), 700 kDa (b), and 1200 kDa (c) on three anode active materials: graphite (Gr), micro- (µSi) and nano- (nSi) silicon as a function of the volume ratio *R* of active material to CMC. Error bars represent the standard deviation calculated from measurements with at least three supernatant samples of one formulation.

The adsorbed amount of CMC is shown to be dependent on its M_w, the type of active material, and the particle-to-polymer *R*. All active materials exhibit similar trends in CMC adsorption. First, as *R* increases, the specific amount of adsorbed CMC decreases exponentially, until it reaches a plateau. This outcome was expected as an increase in *R* correlates with an increased surface area of the adsorbent. Consequently, while the total amount of adsorbed CMC grows, the polymer density on the surface area decreases. The second trend observed is that an increase in CMC M_w correlates with a greater amount of adsorbed polymer, which was anticipated since a monolayer of absorbed molecules has a higher mass at a higher M_w. Furthermore, the results indicate that CMC exhibits a greater affinity for the micro-Si surface than for graphite. This can be attributed to the variations in surface properties of the active

materials, which have a predominant influence on the adsorption mechanism and, consequently, on the quantity of adsorbed polymer. The CMC adsorption on graphite is due to the hydrophobic attraction between the cyclic structure of CMC and the hydrophobic graphite basal planes [58,157]. However, on a silicon surface covered by a partially hydrolyzed native silicon oxide layer [169], adsorption can occur through either covalent or hydrogen bonding, depending on the pH [59–61]. This process occurs via the interaction of the carboxyl groups of the CMC and the silanol groups present on the silicon surface.

Interestingly, while CMC exhibits the strongest affinity for micro-Si among all the materials studied, its interaction with nano-Si is notably poor, irrespective of the CMC M_w and R. The additional thermogravimetric analysis (TGA) (Supplementary Figure S4.4) of the powders reveals a greater mass loss of the nano-Si sample compared to micro-Si, which may be attributed to the presence of a greater quantity of surface modifiers on the nano-Si particles. Further confirmation of the differences in surface properties of the silicon powders could be obtained through zeta potential measurements (Supplementary Figure S4.5). The zeta potential of both materials displays the typical trend characteristic of silicon powders. The oxidized silicon surface undergoes hydrolysis in water, forming silanol (SiOH) groups [170]. As the pH rises, the SiOH groups on the silicon surface undergo deprotonation, resulting in a surface dominated by SiO^-, causing the zeta potential to decrease. However, in aqueous media with a pH below 4, the SiOH groups interact with H^+, forming $SiOH_2^+$, which leads to an increase in zeta potential [168]. The overall higher zeta potential of nano-Si can be ascribed to the lower number of SiOH groups. Since these sites function as centers for CMC adsorption [171], their reduced quantity may result in significantly lower polymer adsorption. We did not consider the adsorption of CMC on CB here, since the fraction of CB is much smaller than that of the active materials and hence does not contribute significantly to the adhesion of anode layers to the current collector.

4.3.3. Adhesion of anodes

The active anode layer is bonded to the copper current collector via polymeric binders. A series of negative electrode samples were produced and subjected to a 90°-peel test to investigate how the adhesion between SBR and three potential attachment surfaces on the electrode active layer side (active material particles, CB, and CMC) affects the adhesive strength between the anode layer and copper current collector. While the peel area in macroscopic adhesion experiments (as described in section 4.3.1 *Adhesion of SBR films to anode components*) is larger than the particle/particle or particle/current collector contact area in electrodes, the surface energy governing adhesion failure remains a material constant. Therefore, the findings from macroscopic adhesion experiments can be applied to point-like adhesion present in electrodes.

As illustrated in Figure 4.3, the line load of the graphite anodes exhibits a decline with an increase in CMC M_w. Given that higher M_w corresponds to a greater uptake of

CMC onto the particle surface, as demonstrated in Figure 4.2, the adsorbed CMC layer may act as a barrier, inhibiting direct and significantly stronger SBR-particle bonding, thereby reducing the overall adhesion of the anode layer to the current collector. To verify this hypothesis, graphite electrodes with a non-adsorbing PEO binder [172] were fabricated, both with and without the addition of SBR. In contrast to anodes with CMC, the use of PEO ensures that graphite particles are free from adsorbed polymeric thickener layers, thereby eliminating its negative effect on anode adhesion. Consequently, the line load of the PEO anodes (Supplementary Figure S4.6) is approximately twice as high as the adhesive force of the graphite anodes with adsorbing CMC and the same concentration of SBR. As PEO does not contribute to the adhesion strength of the anodes (Supplementary Figure S4.6), it becomes evident that when SBR can directly dock to the active particle surface, the adhesion strength significantly increases. Nevertheless, even with a non-adsorbing thickener ensuring direct contact between SBR molecules and particles, the measured line loads are found to be significantly lower than those observed between bulk materials (Figure 4.1). This discrepancy is attributed to the higher contact surface area between SBR films and substrates in comparison to a single-point interface between anode components, which is a characteristic of SBR as a point-to-surface contact binder [54].

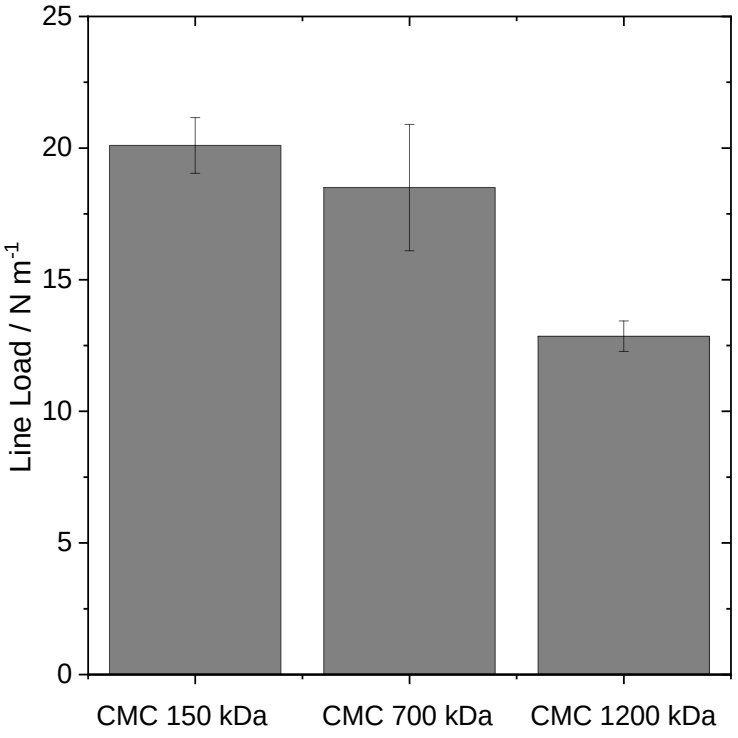

Figure 4.3. Line loads of graphite anodes prepared with CMC of varying molecular weight of 150 kDa, 700 kDa and 1200 kDa. Error bars represent the standard deviation calculated from measurements with at least ten electrode samples.

Thus, the line load can be considered as a function of the amount of polymeric thickener adsorbed on the particle surface. This correlation is depicted for graphite and

graphite-silicon composite anodes in Figure 4.4. In composite anodes, 20 wt% of graphite was substituted with micro-Si or nano-Si, and the active material to polymer *R* was 39 and 7 for graphite and silicon, respectively. The adsorbed polymer amount refers to the amount of polymer (CMC or PEO) adsorbed on graphite or silicon active material, and it varies due to CMC M_w. Graphite anodes with non-adsorbing PEO demonstrate the highest adhesion to the copper foil. In the case of anodes comprising an adsorbing polymeric thickener, it was found that the adhesion strength declines with increasing amount of adsorbed polymer. This suggests that the likelihood of SBR directly adhering to active material particles is reduced when a greater quantity of polymer is adsorbed. As the SBR-CMC bond is the weakest, as demonstrated in section 4.3.1 *Adhesion of SBR films to anode components*, it can be concluded that the electrode adhesion to the copper foil is directly affected by the adsorbed CMC layer.

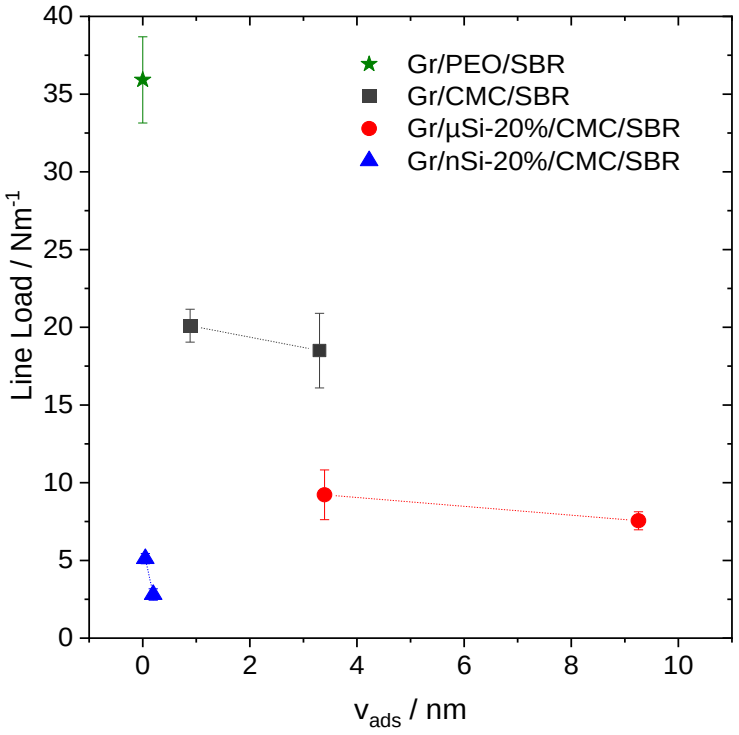

Figure 4.4. Line loads of graphite and graphite-silicon anodes prepared with CMC/SBR or PEO/SBR binder system as a function of specific volume of adsorbed polymeric thickener (CMC or PEO). The adsorbed polymer amount refers to the data obtained from the adsorption measurements conducted with particles dispersed in a dilute polymer solution (see Figure 4.2). Error bars represent the standard deviation calculated from measurements with at least ten electrode samples.

Notably, the line load of nano-Si-graphite anodes is significantly reduced compared to the other investigated electrodes, although the CMC adsorption on nano-Si is more than an order of magnitude lower than on graphite or micro-Si. This phenomenon can be attributed to structural effects. In an aqueous environment, silicon nanoparticles

tend to agglomerate. The diameter of these agglomerates ranges from 0.77 µm ($x_{10,3}$) to 22 µm ($x_{90,3}$) with an average value of 5.55 µm ($x_{50,3}$). SBR molecules with a diameter of up to 170 nm are capable of diffusing into the porous structure of these nano-Si agglomerates (Figure 4.5A and B) and becoming trapped. As a result, a markedly reduced amount of SBR is able to come into contact with the copper interface and bond the particles to the current collector foil, thereby reducing the overall adhesion strength of the electrode. This hypothesis could be confirmed through a simple experimental procedure involving the preparation of a nano-Si/water/SBR suspension, followed by centrifugation. Subsequently, the mass increase of the dry sediment due to the oxidation of the silicon surface, and the remaining SBR within the silicon agglomerates was determined. The results demonstrated that 40.3 ± 7.3 % of the initial quantity of SBR was trapped in the nano-Si sediment. For comparison, the same experiment was conducted with micro-Si particles, which yielded a considerably lower percentage of the initial SBR quantity of 9.1 ± 3.6 % remaining in the sediment. These findings indicate that while using nanoparticles as an active material, electrode adhesion is influenced by both thickener adsorption and the structural effect described above. The latter leads to a reduction in the overall amount of SBR available to bond with the copper foil, thus exerting a pronounced negative impact on the anode adhesion.

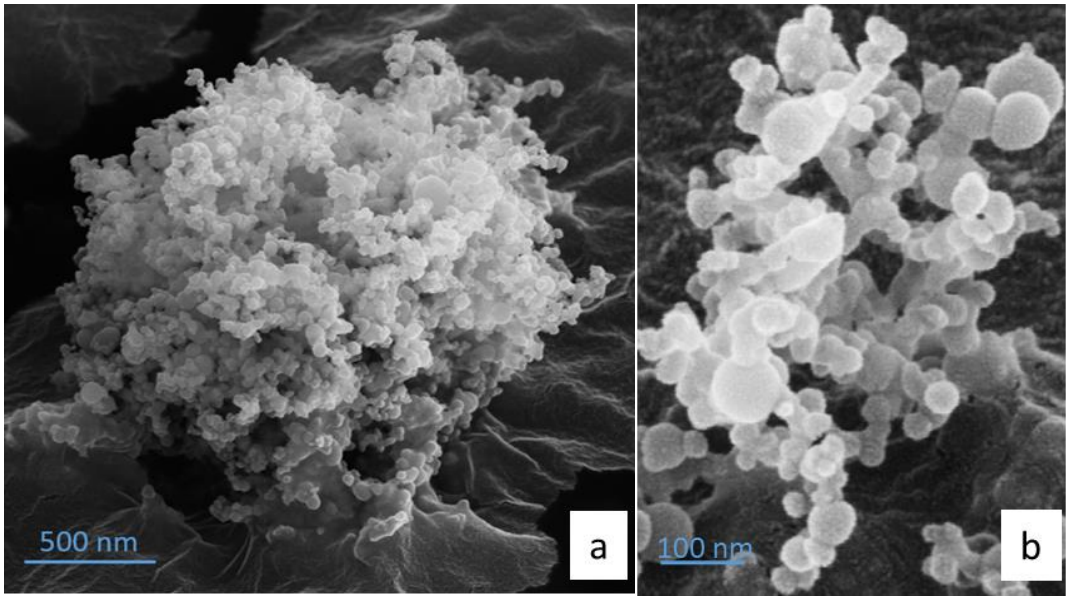

Figure 4.5. SEM images of a nano-Si agglomerate at magnifications 100,000x (a) and 200,000x (b) (Zeiss Leo 1530, 10 kV).

4.4. Conclusions

In summary, the present study investigates how the adsorption of CMC on active material particles exerts a negative impact on the adhesion of graphite and graphite-silicon anodes, despite the fact that, in the absence of SBR, it does not affect electrode adhesion and is added to the anode slurries as a thickener and stabilizer. As SBR

represents the component of the slurry responsible for maintaining the robust connection between the copper current collector and the anode layer constituents (active material particles, CB, CMC), we conducted 90°-peel tests to ascertain the adhesion strength between the SBR films and the individual anode components. The results demonstrate that the highest interfacial strength is observed between SBR and graphite, followed by adhesion between SBR and quartz glass (served as an equivalent surface for the silicon active material). The weakest bonding occurs between SBR and CMC, and given that this adhesion value is significantly lower than the adhesion between SBR and copper foil, delamination of the anode active layer from the copper current collector will occur most probably at the SBR-CMC interface. Therefore, we proposed that the adsorbed CMC layer may act as a barrier, impeding the strong adhesion of the active material particles to the copper foil. Furthermore, the CMC adsorption behavior was determined as a function of molecular mass for three different AMs: graphite, micro- and nano-silicon. The results indicate that CMC exhibits the highest affinity for the micro-silicon surface, followed by graphite, and the lowest affinity for the nano-silicon. In the last section, we demonstrate how the adhesion between the SBR and individual anode components is reflected in the complex polymer/particle system that constitutes the anode. An increase in CMC M_w, corresponding to greater uptake of the polymer on the active material surface, has been observed to result in a decline in the line load of the graphite and graphite-micro-Si composite anodes. Moreover, the utilization of a non-adsorbing polymer as a thickener has been shown to significantly enhance the adhesion of the graphite anode, which can be attributed to the direct interconnection between the particle and the SBR polymer. In addition, the adhesion of electrodes can be affected by the structure of the active materials. We showed that SBR particles can diffuse inside nano-silicon agglomerates and become trapped. Consequently, graphite-nano-silicon composite anodes exhibit markedly low adhesion even though the nano-silicon particles adsorb only a very low amount of CMC.

As demonstrated in our previous research [148], sufficiently high adhesion of the anodes is crucial for their manufacturing process. At the same time, considering that high SBR content impedes electrochemical cell performance and reduces cyclic stability, high adhesion and cohesion with low SBR amount is desired to improve LIB quality and lifespan. This can be achieved by implementing the findings of the present study. For optimizing a commercial CMC/SBR binder system, choosing appropriate CMC grades with lower M_w or DS to reduce adsorption can enhance the mechanical performance of anodes.

Moreover, other potential strategies to mitigate the negative effects of binder adsorption on anode adhesion can include surface modifications of active material particles to ensure particle stabilization without thickener adsorption, or the use of binders with strong thickening properties but minimal or no adsorption on active material particles. The investigation of the latter approach is the focus of our ongoing research.

4.5. Supplementary materials

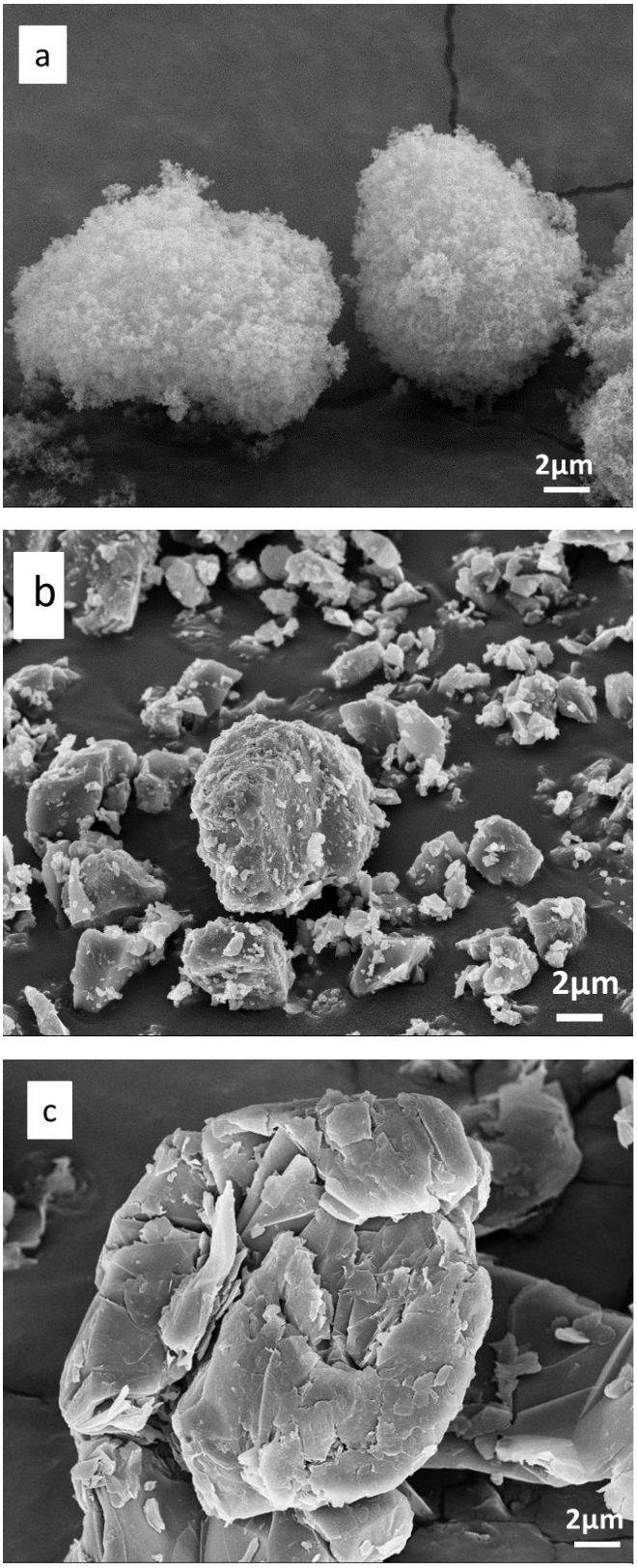

Figure S4.1. SEM images of nano-silicon ($x_{50,3}$ = 100 nm, Nanostructured & Amorphous Materials Inc., USA) (a), micro-silicon ($x_{50,3}$ = 3.3 µm, Silgrain® e-Si 410, Elkem, Norway) (b) and graphite ($x_{50,3}$ = 17.8 µm, SMG A5, Showa Denko Materials Co, Ltd., Japan) (c) particles.

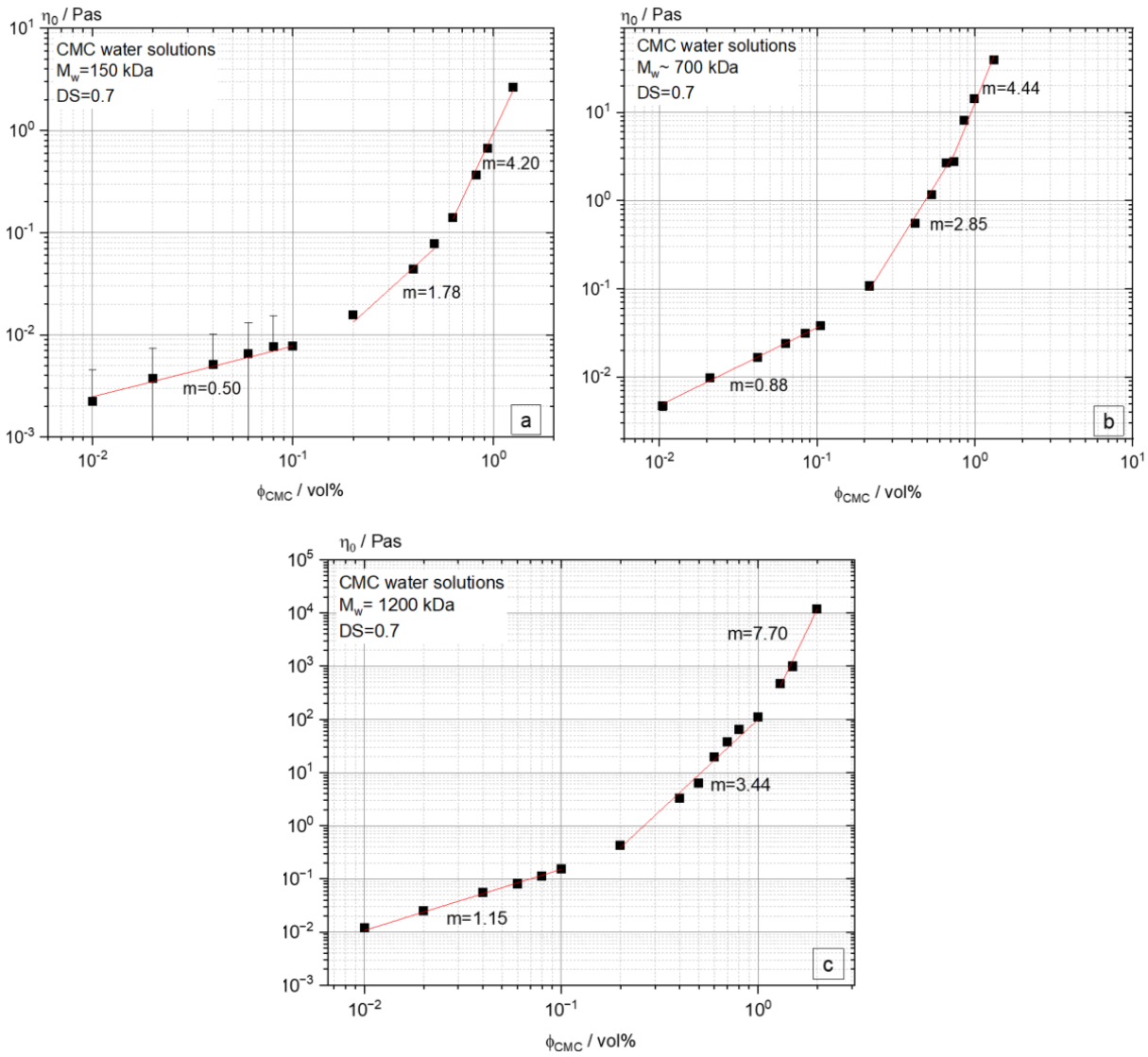

Figure S4.2. Zero-shear viscosity vs. polymer volume fraction for aqueous solutions of CMC with DS = 0.7 and M_w of 150 kDa (a), 700 kDa (b) and 1200 kDa (c).

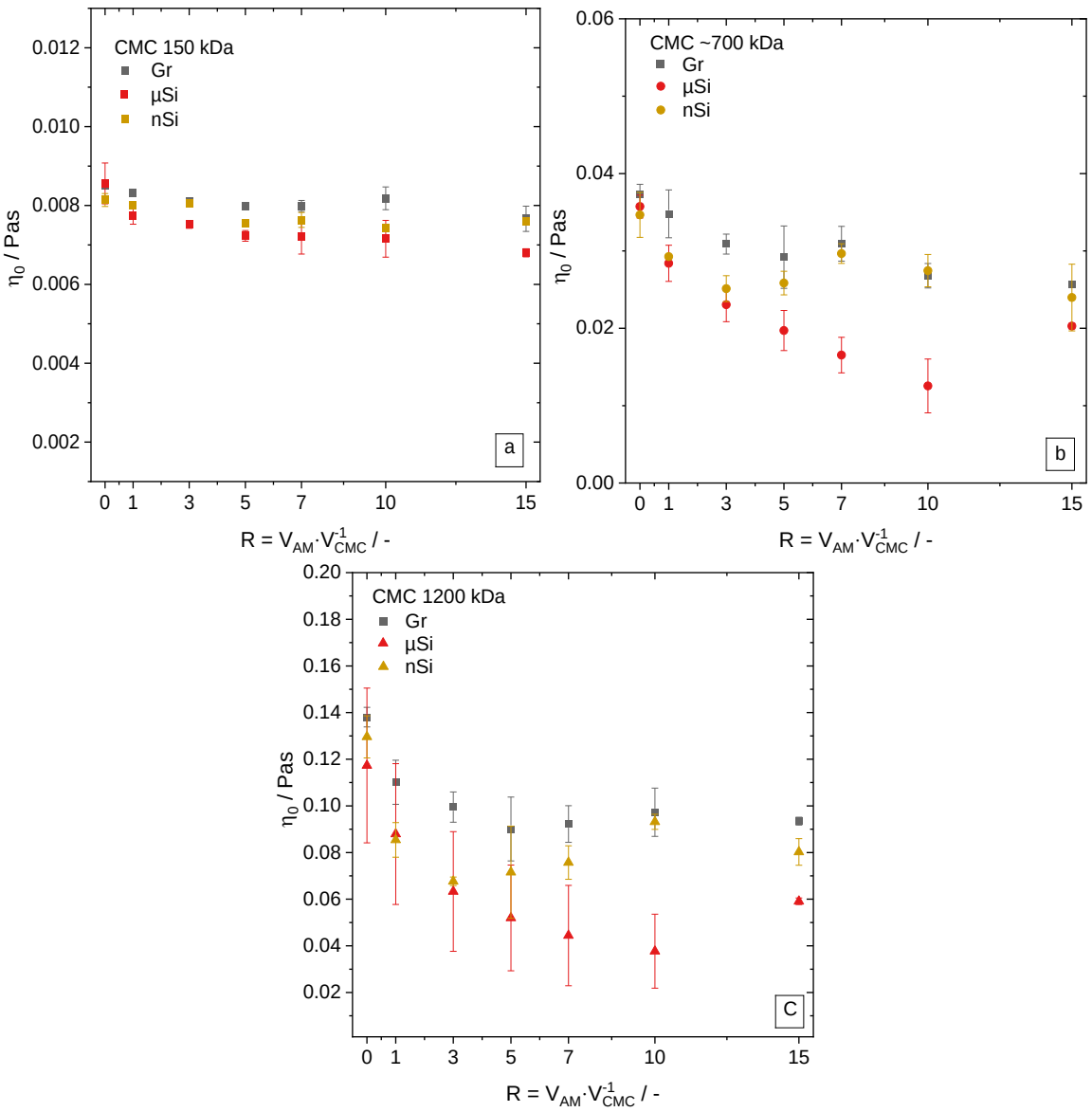

Figure S4.3. Zero-shear viscosity versus volume ratio *R* of active material and CMC for the supernatants obtained from centrifugation of suspensions of active material particles in aqueous CMC solutions with DS = 0.7 and M_w = 150 kDa (a), 700 kDa (b), and 1200 kDa (c).

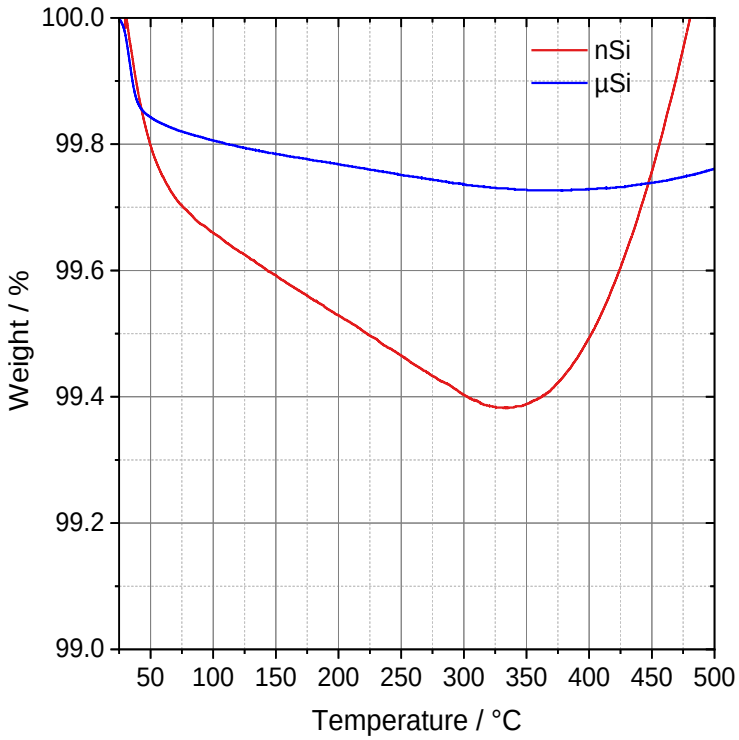

Figure S4.4. Thermogravimetric analysis (TGA) of nano-silicon (nSi) and micro-silicon (µSi) powder under N_2 atmosphere.

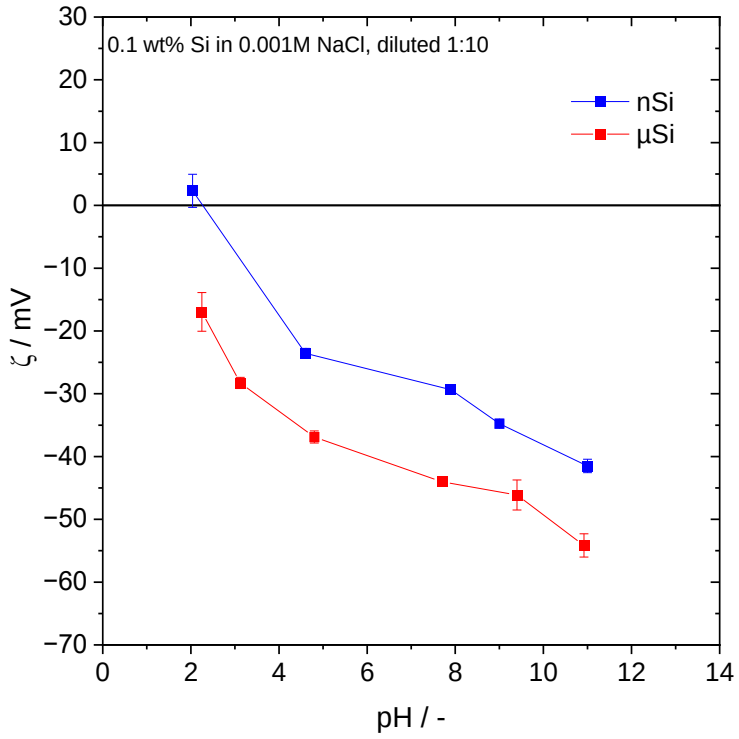

Figure S4.5. Zeta potential of aqueous suspensions of nano-silicon (nSi) and micro-silicon (µSi) particles vs. pH.

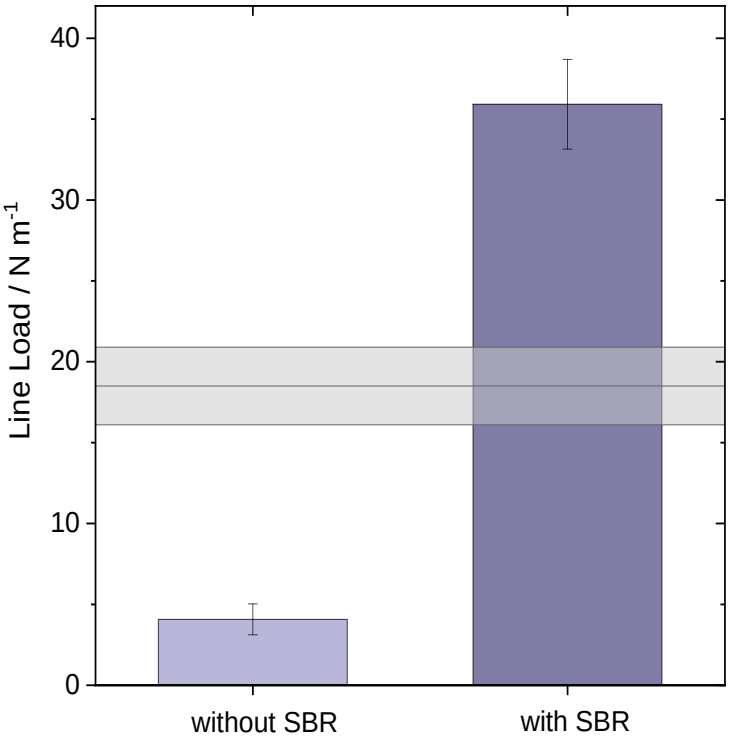

Figure S4.6. Line load of graphite anodes including PEO (M_w = 1000 kDa) with and without SBR. The grey reference line represents the line load of the graphite anode with CMC 700 kDa and the same amount of SBR as in the PEO anode.

5. Cross-linked acrylate binder for high-rate graphite anodes

Full title:	Cross-linked acrylate binder for high-rate graphite anodes
Authors:	Katarzyna Hofmann, Anna Smith, Norbert Willenbacher
Status:	Published
Bibliographic data:	Battery Energy 2025, e70054; DOI: 10.1002/bte2.20250059

Abstract

Sodium carboxymethyl cellulose (CMC) and polyacrylic acid (PAA) are state-of-the-art binders in aqueous-processed anodes for lithium-ion batteries. Binders act as dispersing agents and rheology modifiers in aqueous slurries, while also providing mechanical integrity of dry electrodes during battery fabrication and operation. However, despite their low concentration, they may have detrimental effects on the conductivity and electrochemical performance of batteries, e.g., due to their adsorption on active material particles, which is supposed to limit Li^+ insertion and extraction, but also affect electrode microstructure and adhesion to the current collector. Here, a commercially available, cross-linked acrylate binder (Carbopol® Ultrez 10, x-PAA) with high thickening efficiency is applied for graphite anodes. At lower polymer content, anode slurries based on x-PAA exhibit high-shear viscosities similar to those of the CMC reference and provide a yield stress, which is advantageous for slurry stability. Furthermore, SBR content could be reduced without loss of adhesion strength compared to the CMC reference, since x-PAA does not adsorb onto graphite. Thus, the total binder content could be lowered by about 40 % in comparison to reference anodes comprising CMC. The substantial reduction in total binder amount resulted in slightly lower long-term stability compared to the reference cell including CMC. Cells incorporating x-PAA, however, outperformed references under fast-charging conditions (up to 5C) presumably since x-PAA does not adsorb on graphite, thus enabling more effective Li+ insertion and extraction. Further refinement of crosslinking microstructure may enable fabrication of electrodes with higher energy density and higher capacity retention during cycling, irrespective of cycling rate.

5.1. Introduction

Aqueous processing represents the state-of-the-art in anode production for lithium-ion batteries (LIBs). The primary advantage of this method is its environmental friendliness and cost-effectiveness, as it does not require the use of hazardous and expensive organic solvents or the subsequent solvent recovery equipment during electrode manufacturing [173,174]. To guarantee the adequate dispersion of all electrode slurry components while maintaining suitable flow properties for the coating process, polymeric binders are incorporated into the formulation. Additionally, they facilitate the mechanical integrity of electrodes during both fabrication and operation [55,113,175].

Carboxymethyl cellulose (CMC), polyacrylic acid (PAA), and styrene butadiene rubber (SBR) are among the most commonly used water-based binders for LiB anodes. CMC and PAA primarily act as dispersing agents and rheology modifiers, facilitating uniform particle distribution in the slurry and providing the flow behavior demanded for high-quality uniform coating. At higher molecular weights, these polymers can also improve cohesion of the electrode layer [62,176]. According to the literature, both linear PAA and CMC adsorb onto active material particles, and the underlying adsorption mechanisms depend, among other factors, on the type of active material. For natural graphite, which possesses a relatively smooth surface, linear PAA and CMC predominantly adsorb onto the basal planes through hydrophobic interactions [58,157,167]. In contrast, for artificial graphite, natural graphite with defective surfaces, or silicon, adsorption occurs primarily via interactions of the polymers´ carboxylic groups with surface functionalities of the active material particles [57,58,167,177]. PAA's advantageous properties as an electrode binder include its higher carboxylic group density compared to that of CMC, which facilitates enhanced interaction with active material particles such as silicon, as well as low swelling in carbonate-based electrolytes [176,178,179].

To increase the energy density of a LIB, it is desirable to minimize the binder content, as it constitutes an electrochemically inactive component of an electrode. However, even more importantly, despite their low concentration, binders may have a detrimental effect on the conductivity and electrochemical performance of battery electrodes. CMC adsorbs onto graphite, which reduces the adhesion between the anode and the current collector, and also affects the electrode microstructure depending on molecular weight and degree of substitution [62,180]. Linear PAA poses significant limitations regarding the control of rheological properties. Specifically, the thickening efficiency of this polymer at the molecular weights typically used in LIB applications (250–450 kDa) is poor. Consequently, elevated binder concentrations are necessary to attain a slurry with adequate flow properties for coating processes. Moreover, the viscosity of PAA solutions is highly pH-dependent [181], in contrast to CMC, which offers more stable behavior [182]. In addition, the glass transition temperature of both PAA and CMC exceeds 100 °C [183,184], which is far above the typical operating temperature range of LIBs (–20 to 55 °C) [185]. Consequently, these

polymers remain brittle under the conditions experienced during battery operation [186]. This brittleness limits the potential for binder content reduction, as an additional adhesion promoter is still necessary to ensure adequate bonding between the electrode layer and the current collector foil. Accordingly, SBR with a glass temperature typically ranging between –10 °C and 10 °C is mainly employed as an adhesion promoter, but also enhances anode cohesion [148].

Numerous examples of the application of linear PAA as a binder, particularly for silicon-containing anodes, can be found in the literature [176,178,187,188]. However, as previously stated, due to the low viscosity of PAA, it is necessary to employ a binder amount exceeding 10 wt% or to incorporate an additional thickener, for example, sodium alginate [189], to achieve the desired dispersion properties. To enhance the mechanical properties of PAA and introduce new functionalities such as ionic and electronic conductivity, next-generation PAA binders are designed with two-dimensional (2D) or three-dimensional (3D) architectures [190]. These structures are achieved through grafting or cross-linking with other polymers, including carboxymethyl cellulose (CMC) [68], poly(vinyl alcohol) (PVA) [69], chitosan [191,192], sodium alginate [70], gum arabic [193], and others.

For example, Preman et al. [194] recently introduced a novel binder for silicon anodes, x-PAA/PSUOH, formed by crosslinking PAA with a synthesized copolymer of poly(sodium 4-styrenesulfonate-co-ureido-pyrimidinone methacrylate-co-hydroxyethyl methacrylate). Anodes incorporating the x-PAA/PSUOH binder exhibit enhanced mechanical integrity and ionic conductivity, achieving an initial capacity of 3572 mAh g^{-1} and a capacity retention of 71 % over 300 cycles. Jeong et al. [195] cross-linked highly elastic poly(urea-urethane) (PUU) with rigid PAA and employed the resulting copolymer as an anode binder for Si electrodes. By combining the distinct mechanical properties of both polymers, the structural integrity of the Si anode was maintained despite its large volume expansion during cycling. Consequently, the cells exhibited enhanced cycling performance compared with those using the neat PAA binder. Similarly, Wang et al. [196] designed a self-healing PCI binder through chemical cross-linking of PAA, polyethyleneimide (PEI), and citric acid (CA). The binder, rich in carboxyl and amide groups, strongly interacts with Si nanoparticles and exhibits excellent elasticity along with high adhesive strength. As another example, Lv et al. [197] synthesized a cross-linked network binder based on ultraviolet (UV)-cured waterborne polyurethane acrylate (WPA) for Si/C anodes. The high cross-link density enhanced mechanical strength and significantly reduced electrolyte swelling. Combined with the binder´s high electronic and ionic conductivity, this resulted in improved cycling stability compared with PAA-based cells.

Despite these promising properties, such modified PAA binders have not yet reached commercialization. This is primarily due to the complexity of the synthesis process, which involves multiple steps, yields limited quantities, finally resulting in high production costs.

Recently, we demonstrated that polymer adsorption on graphite and silicon active material impedes strong SBR-particle bonding, thereby reducing the overall adhesion of the anode to the copper current collector [180]. Building on these findings, the present work explores the application of a commercially available, highly cross-linked acrylate thickener Carbopol® Ultrez 10, which, in combination with SBR, forms an efficient binder system for graphite anodes.

Carbopol® Ultrez 10 is a highly cross-linked polyacrylic acid polymer (Figure 5.1) composed of acrylic acid homopolymers and copolymers with alkyl acrylates, with crosslinking provided by allyl ether derivatives of polyalcohols. As a commercially available rheology modifier and thickener, it is widely used, e.g., in cosmetics, pharmaceutical formulations, or coatings [198,199]. When dispersed in water, Ultrez 10, even at low concentrations, forms gels with a very high elasticity, which strongly depends on the pH [200]. At concentrations relevant for technical applications (0.1–0.5 wt%), Ultrez 10 exhibits a highly heterogeneous microstructure composed of agglomerates of primary gel particles, forming a percolated network in the neutralized state. The crosslink density of these gel agglomerates is non-uniform, and they are surrounded by loosely associated polymer chains that extend outward. A comprehensive study of the microstructure of Ultrez 10 is provided in [199].

In this study, we demonstrate that graphite electrodes based on Ultrez 10 and SBR binder exhibit excellent rate capability and stable long-term cycling performance. Moreover, due to the very high thickening efficiency of Ultrez 10 and the lack of adsorption on graphite particles, a 38 % reduction in total binder content could be achieved compared to a reference electrode including a conventional CMC/SBR binder system.

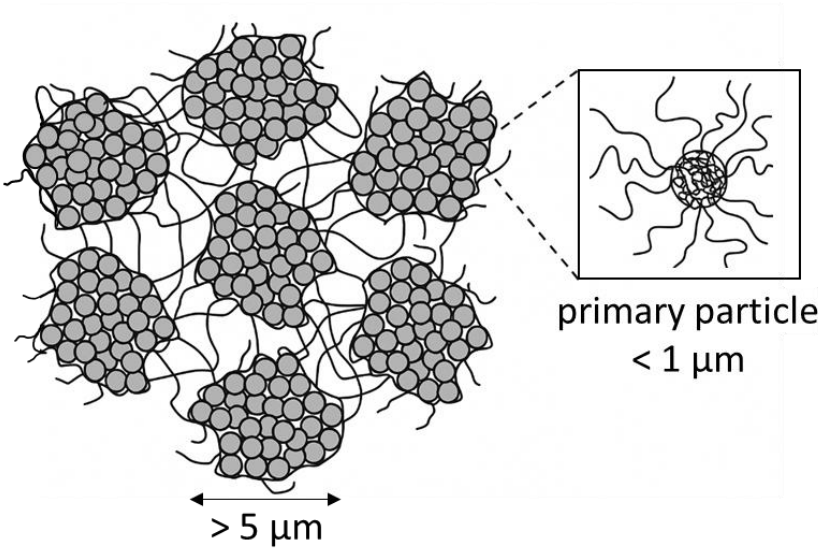

Figure 5.1. Schematic illustration of the x-PAA binder microstructure. The inset shows a primary particle with a highly cross-linked core and dangling ends. Edited from [199].

5.2. Experimental

5.2.1. Electrode preparation

The preparation of water-based anode slurries always began with the formulation of a binder solution. Three different polymers were used: highly cross-linked polyacrylic acid x-PAA Carbopol® Ultrez 10 (Lubrizol, USA), linear polyacrylic acid (l-PAA) with molecular weight M_w = 250 kDa, Sigma-Aldrich, Germany), and sodium carboxymethylcellulose (CMC) with Mw = 150 kDa and degree of substitution DS = 0.7 (TEXTURECELL CRT 2000PA07, DuPont, USA). x-PAA, and CMC were utilized in powder form, while the l-PAA was employed as a 35 % aqueous solution.

For x-PAA, the first step of solution preparation was to produce a stock solution of 1 wt% by gradually introducing the polymer powder into a beaker containing distilled water, with continuous gentle agitation applied throughout the process. Stirring was performed using a propeller with a diameter *d* of 50 mm, operating at 400 rpm for 30 minutes, followed by 100 rpm for an additional 30 minutes. Subsequently, the polymer solution was subjected to continuous stirring using a magnetic stirrer for approximately 12 hours. Then, the final binder solution (0.5 wt% and 0.7 wt%) for a slurry was prepared by first diluting the stock solution with distilled water and subsequently neutralizing it with NaOH. The initial pH of the x-PAA solution was approximately 2, and after neutralization, it increased to around 6.

Similarly, a l-PAA solution was prepared by first diluting a specific amount of a 35 wt% aqueous l-PAA solution with distilled water, followed by stirring with a 50 mm diameter propeller at 1200 rpm for 30 minutes. The initial pH value of the resulting solution was approximately 2, and was subsequently modified to a value of about 6 using NaOH.

A CMC solution was prepared by dissolving CMC powder in a beaker containing distilled water. The components were stirred using a 50 mm diameter propeller at 1200 rpm for 30 minutes until complete powder dissolution. The resulting CMC solution had a pH value of about 7.

All final binder solutions were formulated to contain 95 % of the total amount of distilled water required for slurry preparation. In the subsequent steps, the powder components were admixed to the binder solution: carbon black (C-Nergy Super C65, Imerys Graphite & Carbon, Switzerland) was added first, followed by graphite (SMG A5, Showa Denko Materials Co, Ltd., Japan). The mixture was then stirred using a dissolver (d = 50 mm) at 2000 rpm for 5 and 10 minutes, respectively. Next, styrene butadiene rubber (SBR, BM-451B, Zeon, Japan) as 40 wt% aqueous dispersion was introduced and stirred at 2000 rpm for 5 minutes. Finally, the remaining 5 % of distilled water was added and the slurry was mixed at 2000 rpm for another 5 minutes. All slurries maintained a constant solids content of 42 wt% (corresponding to 25 vol%).

After the mixing process, slurries were degassed in a desiccator and subsequently coated on a 10 µm thick copper foil (SE-Cu, Schlenk Metallfolien GmbH & Co. KG, Germany) using a doctor blade (ZUA 2000, Zehntner GmbH, Switzerland). The coating was performed at a velocity of 10 mm s^{-1}, with a coating gap of 160 µm for anodes with x-PAA, and 180 µm for anodes with CMC and l-PAA. The thickness of the dried electrodes was found to range from 69 to 72 µm, with porosity measuring approximately 60 %. Some of the dried anodes were calendered with a roll-to-roll calendar (GKL, Saueressig GmbH, Germany) with a roll width of 400 mm and a working speed of 1 m min^{-1} to achieve a target porosity of 40 %.

5.2.2. Rheological characterization of anode slurries

The rheological properties of anode slurries were characterized using a rotational rheometer (Physica, MCR 501, Anton Paar 201 GmbH, Germany) equipped with a plate-plate measuring system (PP25TG, diameter d = 25 mm, gap height h = 1 mm). Steady shear measurements were performed in a logarithmic shear stress ramp mode, covering the stress range from 0.01 to 1000 Pa with 10 points per decade and a logarithmic decreasing measuring time from 60 s to 10 s. Measurements were performed at 20 °C.

5.2.3. Mechanical properties of anodes

Anodes, both before and after the calendering process, as well as after electrochemical cycling, underwent 90°-peel tests using a universal testing machine (Texture Analyser TA.XT plus, Stable Micro Systems, UK) equipped with a 5 kg load cell. For testing, anodes were first cut into 2.5 cm wide strips and affixed to a movable test plate using double-sided adhesive tape. The free end of a sample was attached to the machine arm at a 90° angle and subsequently peeled off at a constant velocity of 5 mm s^{-1}. To ensure reproducibility, at least 10 samples of each anode formulation were tested. The peel force was recorded for each sample, normalized to the sample width, and averaged to obtain the line load.

Furthermore, to determine the cohesion of anode layers, degassed slurries were cast into silicone moulds and dried at 50 °C for approximately 18 hours. The dried samples were then cut and ground into cubes measuring 5 mm x 5 mm using sandpaper. These samples were subsequently subjected to compression tests in accordance with the DIN 51104 standard, employing a universal testing machine (Texture Analyzer TA.XT plus, Stable Micro Systems, UK) equipped with a 50 kg load cell.

5.2.4. Electrochemical characterization of anodes

Pouch cell assembly

Calendered anodes with a target capacity of 2.1 mAh cm^{-2} were punched with size of 5.4 x 5.4 cm and paired with one-sided coated commercial NMC111 ($LiNi_{0.33}Mn_{0.33}Co_{0.33}O_2$) cathodes with an areal capacity of 1.9 mAh cm^{-2} punched with size 5.0 x 5.0 cm. Electrodes and 5.9 x 5.9 cm PET-based separators with a ceramic coating were dried under vacuum for 24 h at 130 °C and 180 °C, respectively. Subsequently, the assembly of lab-scale pouch cells was conducted using a semi-automated manufacturing line under dry room conditions. The cells were filled with 450 µl electrolyte (1 M $LiPF_6$ in 50/50 (w/w) ethylene carbonate (EC) and dimethyl carbonate (DMC) with 3 wt% of vinylene carbonate (VC) as an additive (already mixed, purchased from Gotion)) and sealed under reduced pressure. Subsequently, the cells were stored over night at 40 °C for sufficient wetting of the separator and electrodes.

For each anode formulation, two cells were built and after formation subjected to the rate capability test in discharge direction, followed by the cycling test including RiDCs. Additionally, two cells containing CMC anodes and two cells with x-PAA anodes were assembled, formatted and tested in the rate capability test in charging direction.

Data Acquisition

Electrochemical testing was performed using BaSyTec CTS LAB instruments while cells were stored in a climate chamber at 25 °C (±0.1 °C).

Formation

For the formation step four cycles were applied, where charging was performed with constant current (CC) at C/10 until a voltage of 4.2 V was reached with subsequent charging at constant voltage (CV) until the current dropped below C/20. The discharge was performed using CC of C/10. Finally, the cells where charged to 3.7 V using C/10 CC for storage until the next cell test was performed.

Rate capability test

An asymmetric rate test was performed in probing either discharge or charge capability. For discharge testing charging was done with a C-rate of C/2 CC including a CV phase at 4.2 V (until I<C/20) and rates in discharge direction were varied from C/2 to 5 C until a cut-off voltage of 3.0 V. To check for degradation due to the rate testing C/2 discharge was included at the end of the test procedure. For each C-rate two full cycles were applied.

For charge capability same rates were used, however, now the discharge current was kept constant applying C/2 CC and charging was varied from C/2 CC to 5C CC and back to C/2 (each two cycles). All charging steps ended with CV-phases (until I<C/20). For the rate testing in charge direction values from the CC-charging phase are plotted as they represent the true power capability of the battery cell.

Cycling test including Direct Current Internal Resistances (RiDCs)

For long term cycling, all cells were cycled applying 1 C CC with CV until I<C/20 and 1C CC discharge current. The voltage window was 3.0–4.2 V. “Check-up cycles” were used every 100 cycles meaning measurements were made at five states of charge (SOCs), namely 10 %, 30 %, 50 %, 70 % and 90 %, based on the determined cell capacity just before the test. For all SOCs direct current internal resistances (RiDC) were determined by use of current pulses of 1C in discharge direction for 20 s. Applying Ohm's law, the DC internal resistances were determined using the potential drop (difference between the potential at the end of the pulse and the potential in rest state before the pulse) and the applied current for the respective pulses.

5.2.5. Post-mortem analysis

After electrochemical testing, cells were discharged to minimal voltage of 3.0 V and held for 4 h using a CV-phase. Under dry-room atmosphere pouch bag cells were then opened to examine the surfaces of the electrodes and separators by optical analysis using a light microscope (OLYMPUS BX53 M, Japan).

5.3. Results and discussion

5.3.1. Slurry rheology

This section highlights the superior thickening properties of x-PAA. The objective was to adjust the flow behavior of the x-PAA slurry, particularly at high-shear rates, which are relevant for the coating process, to that of the CMC reference slurry.

The x-PAA solutions were neutralized to a pH of approximately 6, that is, close to that of the CMC solution to avoid additional electrochemical effects. At this point, Carbopol® agglomerates undergo swelling, resulting in the formation of a sample spanning network, which is responsible for the observed superior thickening properties [199] and the gel-like texture.

Anode slurries with two different x-PAA concentrations (0.27 vol% and 0.37 vol%, which correspond to 0.29 wt% and 0.40 wt%, respectively) were prepared, and Figure 5.2 illustrates their viscosity as a function of shear rate. Due to the network

provided by the x-PAA binder, these slurries exhibit a yield stress of about 4 Pa and 29 Pa, respectively, and shear thinning behavior at higher stresses. In contrast, the reference slurry with 0.58 vol% (0.72 wt%) CMC does not exhibit a yield stress and shows shear thinning throughout the whole investigated shear stress range, as expected since the CMC itself does not form a gel and, moreover, partially adsorbs onto the graphite particles thus providing steric stabilization of the dispersed particles. The non-adsorbing CMC fraction, however, thickens the continuous phase and controls the viscosity of the slurry [57,64,64]. Note that, in contrast to CMC and l-PAA, x-PAA does not adsorb onto graphite particles, as confirmed by IR spectroscopy (Figure S5.1, Supporting Information), and therefore cannot contribute to their steric stabilization. The absolute value of the yield stress is thus determined not only by the strength of the x-PAA network, but also by the particle network created due to prevailing van der Waals attraction. The high shear viscosity of the slurry containing 0.40 wt% x-PAA closely matches that of the reference slurry and was thus selected for fabrication and characterization of electrodes, which will be discussed below. This result demonstrates that equivalent rheological performance can be achieved with up to 36 % less polymer, highlighting the superior efficiency of the x-PAA as an anode binder.

Moreover, the x-PAA slurry exhibits a significant yield stress, which prevents or slows down sedimentation of graphite particles in the water-based slurry, thus providing an extended shelf-life, and facilitates efficient pumping [98,201–203]. It further enables the formation of well-defined coating edges [204] and also reduces crack formation during fast drying of thick electrode layers. Another advantage is that the yield stress significantly suppresses binder migration – a major concern under high-rate drying conditions that can lead to uneven binder distribution and, as a consequence, to inferior mechanical, electrical, and electrochemical properties of the electrode [144,154,205].

For comparison, the flow behavior of a second, l-PAA based reference slurry was also investigated (see Figure 5.2). The l-PAA slurry comprises 3.10 vol% (3.41 wt%) of polymer, which is considerably higher than the polymer content in both the CMC and x-PAA slurries. Despite its high polymer content, the l-PAA slurry exhibits a markedly lower yield stress of only 1.3 ± 0.3 Pa compared to the x-PAA slurry including 0.37 vol% polymer. Beyond this critical stress, the shear viscosity is nearly Newtonian (i.e., independent of the applied shear stress) and much lower than for the CMC and higher concentrated x-PAA slurry (0.37 vol%). Consequently, the particles in the l-PAA slurry are not sufficiently stabilized over time, which is supposed to result in detrimental effects during technical scale storage and processing operations.

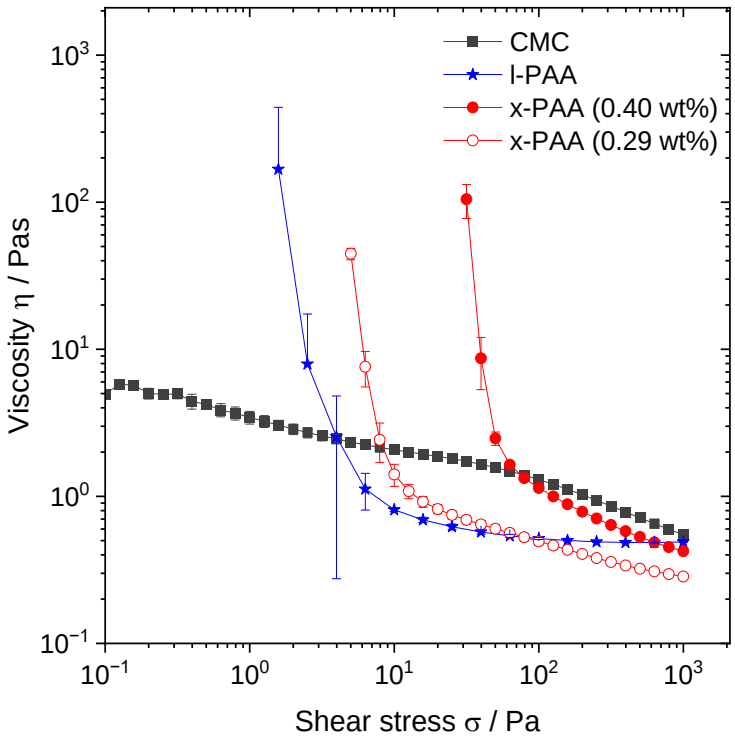

Figure 5.2. Viscosity η as a function of shear stress σ for graphite slurries with solids volume fraction φ = 25 vol% and different binders: CMC/SBR (black squares), l-PAA/SBR (blue stars), and x-PAA/SBR with 0.40 wt% x-PAA and 0.29 wt% x-PAA (red closed and open circles, respectively).

5.3.2. Mechanical properties of anodes

The second approach to reduce the total binder content is based on previous investigations demonstrating the fraction of CMC binder adsorbed on the active material particles diminishes the adhesion between these particles and the current collector [180]. Accordingly, a non-adsorbing polymer binder should allow for a reduced addition of SBR without loss in adhesion.

As expected, using non-adsorbing x-PAA as an anode binder, while maintaining a SBR concentration (2.87 wt% in the dry anode layer) similar as in the CMC reference anode, results in a substantial improvement of adhesion strength (Figure 5.3). Accordingly, the SBR content in the x-PAA slurry was reduced to 1.87 wt% in dry anode layer, the amount at which the line load of the anode layer prepared from the x-PAA slurry was similar to that of the CMC reference. However, the comparison of the absolute line load values has to be treated carefully. The pictures of corresponding electrode samples after peeling, reveal that the CMC-based electrode exhibits purely adhesive failure, whereas the presence of numerous particle residues on the peeled x-PAA anode samples indicates that in this case cohesive failure dominates (Figure S5.2, Supporting Information). Finally, we have prepared an l-PAA-based electrode including 8.28 wt% linear PAA and 1.87 wt% SBR, which exhibits similar line load as the CMC-based electrode.

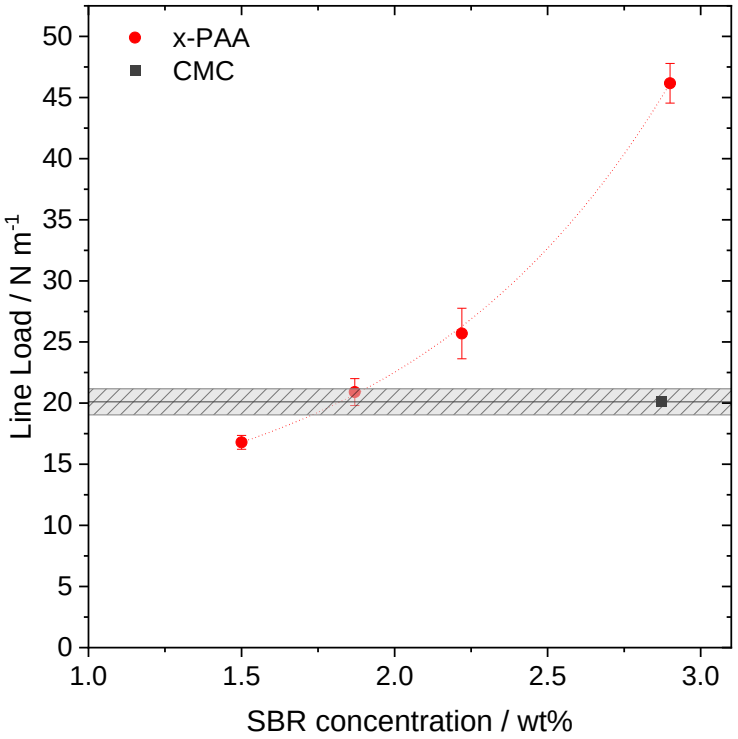

Figure 5.3. Line load of non-calendered anodes with 0.98 wt% x-PAA and various amounts of SBR (red circles). The polymer concentrations refer to the dry anode layer. The black square and black hatched area indicate the line load of the non-calendered CMC reference anode. The thickness of all negative electrodes was about 65 µm.

The lower cohesion of x-PAA electrodes was confirmed via compression tests on dry anode layers; corresponding results are shown in Figure 5.4. As known from literature, an increased content of either thickening agent (e.g., CMC or PAA) [62] or adhesion promoter (e.g., SBR) [148] correlates with elevated electrode cohesion. Accordingly, the x-PAA anodes with the lowest total binder content of 2.86 wt% demonstrate the lowest level of cohesion, whereas the l-PAA samples with a more than three times higher binder content of 9.93 wt% exhibit the highest cohesive strength. Consequently, anodes that employ CMC as a binder, with a content of 4.62 %, show an intermediate degree of cohesion. The total amount of binder in the electrode layers directly correlates to their cohesive strength, which also affects the line load determined in peel experiments. In conclusion, a non-adsorbing binder with high thickening efficiency, such as x-PAA, allows for a reduction of the binder content itself, and additionally for the reduction of SBR without loss of adhesion, but this is limited by the corresponding loss in cohesion.

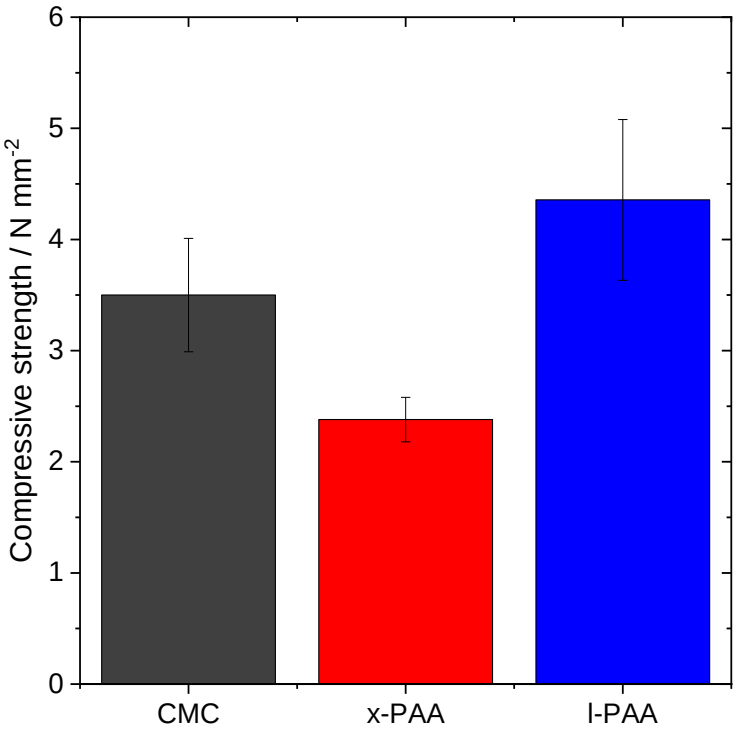

Figure 5.4. Compressive strength of thick anode layers comprising different binders: CMC, x-PAA, and l-PAA. Composition of the different dry anode samples is provided in Table 5.1.

Based on the rheological and mechanical characterization described above, we have prepared three slurries for electrode fabrication, including CMC, x-PAA, or l-PAA, as well as SBR as binders. The composition of the corresponding electrodes is provided in Table 5.1.

The dry anode made from the x-PAA slurry has a total binder content of 2.86 wt%, which is 38 % lower compared to the CMC reference anode.

Table 5.1. Composition of anodes containing CMC, l-PAA, and x-PAA binders selected for electrochemical performance tests. All concentrations refer to the dry anode layer.

Anode	**CMC**	**l-PAA**	**x-PAA**
Graphite, wt%	93.45	84.62	96.01
Carbon Black, wt%	1.93	1.75	1.98
Thickener, wt%	1.75	8.28	0.98
SBR, wt%	2.87	1.65	1.87
Total binder content, wt%	**4.62**	**9.93**	**2.86**

5.3.3. Anode performance within a full-cell battery configuration

To compare the anode performance in a full-cell configuration, CMC, x-PAA and l-PAA anodes were paired with commercial NMC111 cathodes with the areal capacity

of 1.9 mAh cm^{-2}. Due to the full-cell balancing aspects [134] the target areal capacity of anodes was approximately 2.1 mAh cm^{-2}. All electrochemical tests were carried out on two cells for each anode composition. After formation, which included 4 charging/discharging cycles with C/10, anodes with CMC and x-PAA exhibited very similar practical discharge capacities (4^{th} cycle) of about 44.5 mAh (Table 5.2), whereby anodes with l-PAA showed slightly lower capacity of 43.1 mAh.

Table 5.2. Absolute and areal practical capacities of full cells including anodes with CMC, l-PAA, and x-PAA binders after the fourth discharge formation cycle.

Cell properties	**CMC**	**l-PAA**	**x-PAA**
Absolute capacity, mAh	44.56 ± 0.13	43.11 ± 0.03	44.45 ± 0.07
Graphite mass loading, mg cm^{-2}	6.0	5.9	5.8
ICE, %	87.4	87.0	85.9

At first, asymmetric discharge rate capability tests of the pouch cells (delithiation capability of the anode) were performed using a constant charging rate of C/2, followed by a constant voltage phase with a current limit of I < C/20. Discharging was carried out at varying rates ranging from C/2 to 5C. Figure 5.5a illustrates the results in terms of absolute discharge capacity retention. The rate performance of anodes containing l-PAA is noticeably poor. From 2C onwards, a significant decrease in absolute capacity is observed with increasing C-rate, compared to CMC and x-PAA anodes. The retained cell capacity at 3C is 35.5 mAh (which is 84.5 % of the initial capacity), whereas for anodes with CMC and x-PAA 39.0 mAh and 39.8 mAh, which is 90.3 % and 91.6 % of the initial capacity, respectively. Also, at higher C-rates the difference between cells containing anodes with CMC and x-PAA becomes apparent. While at 3C CMC anodes exhibit 39 mAh and x-PAA anodes 39.8 mAh, at 4C the difference is significant: 36.6 mAh and 38.2 mAh, and at 5C 32.2 mAh and 35.6 mAh, which is 74.7 % and 82.0 % of the initial capacity, respectively. At the last C/2 step cells with CMC and x-PAA anodes demonstrate nearly 100 % of their initial capacity, indicating that no irreversible degradation occurred. In the case of anodes with l-PAA the retained capacity in the last C/2 step achieves 41.1 mAh, which is about 98 % of the initial capacity. These results were expected, since anodes with l-PAA contain the highest amount of electrochemically inactive binder material. This increases the resistance of the anode and consequently the internal resistance of the cell. Such an increase in internal resistances leads to voltage limits being reached more rapidly, which reduces the amount of usable charge during discharge and ultimately lowers the cell's effective capacity. Anodes containing x-PAA have the lowest binder content and thus the lowest internal resistance, resulting in an overall better rate capability compared to the CMC and l-PAA reference anodes. The correlation between rate capability and anode resistance is further supported by the shift of the voltage plateau, e.g., decrease of voltage values in the discharge direction with increasing resistance. A plot with selected voltage profiles for the C-rates C/2 and 5C for the CMC, x-PAA and l-PAA cells is shown in the Supporting Information. The same trends, which can be seen in

Figure 5.5a for rate capabilities, are also evident in the voltage shifts for all C-rates, with the most pronounced difference occurring at 5C, as expected (Figure S5.3, Supporting Information). Furthermore, direct current internal resistances (RiDC) values, which are presented in Figure 5.7b and will be discussed in detail below, support this trend.

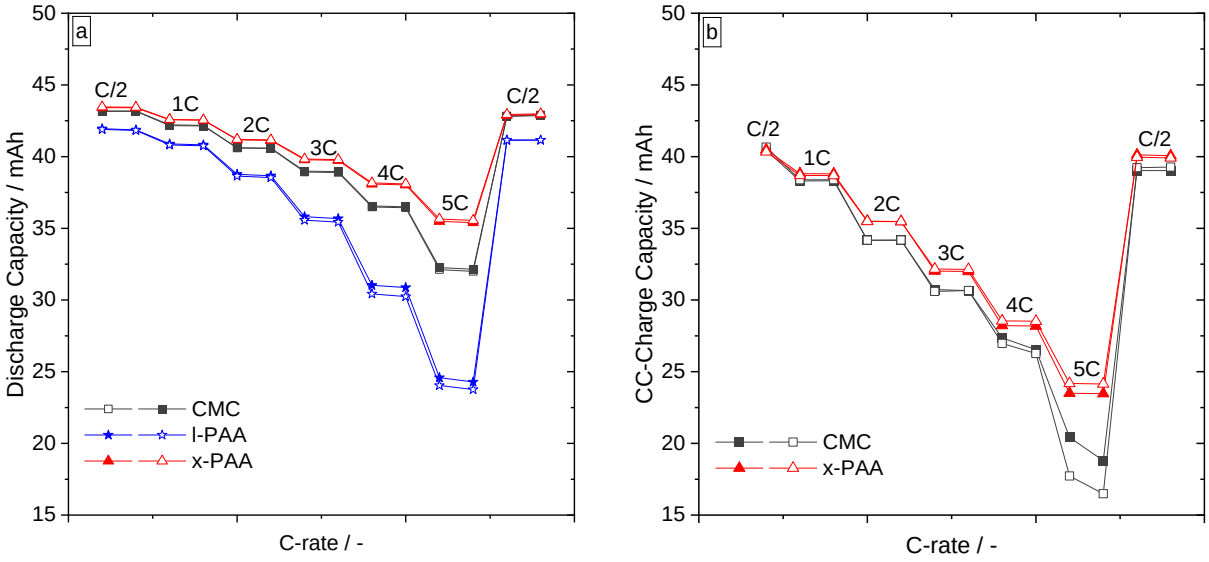

Figure 5.5. Absolute discharge (a) and CC-charge (b) cell capacities as a function of dis-/charge C-rate for pouch cells containing CMC, l-PAA and x-PAA anodes.

In the next step, x-PAA anodes were compared with CMC anodes in terms of rate capability in the charging direction. Therefore, another set of pristine anodes were assembled in pouch cells, and an asymmetric rate capability test was performed at a constant discharging rate of C/2 and varying charging rates ranging from C/2 to 5C. At lower C-rates, CMC and x-PAA anodes show no differences in capacity retention (Figure 5.5b). However, for higher currents starting from 2C, CMC anodes exhibit lower absolute constant current (CC) capacities in comparison to x-PAA anodes. At 5C the difference between absolute capacities is the highest, 23.5 mAh and about 19 mAh for x-PAA and CMC, respectively, which is 58 % and about 45 % of the relative capacity of x-PAA and CMC anodes, respectively. Also, it can be noted that at 4C and 5C CMC-based anode cells show some irreproducible behavior as the repeated charge test does not retain the capacity of the first cycle. This might already indicate some degradation. At the final step of the rate capability test, the cells were charged with C/2 again. It can be observed that cells with x-PAA anodes almost completely recover (99 % capacity retention), whereas cells with CMC anodes lost irreversibly about 3.5 % of their initial capacity. The superior charging rate capability of x-PAA anodes might originate from the absence of an adsorbed polymer layer on the graphite particles, which enables direct contact with the electrolyte. This results in minimal interfacial resistance, thereby facilitating more efficient Li^+ insertion and extraction as the graphite surface remains unobstructed [206]. In contrast, CMC anodes exhibit diminished rate

performance, likely due to the presence of a blocking polymer layer on the graphite surface.

Subsequently, the cells were disassembled in discharged state (delithiation of anode) and subjected to visual inspection to assess potential degradation effects. A substantial accumulation of particle residue can be observed on the separators, particularly in cells incorporating anodes with CMC (Figure 5.6). In contrast, separators from cells containing x-PAA exhibit considerably less residue. Examination under a light microscope reveals a distinct difference in the nature and extent of the deposits. Specifically, separators from CMC cells displayed evidence of lithium plating, characterized by silver-grey deposits [207]. In comparison, separators from x-PAA cells show no signs of lithium plating, with only minor particulate graphite and/or carbon black residue present.

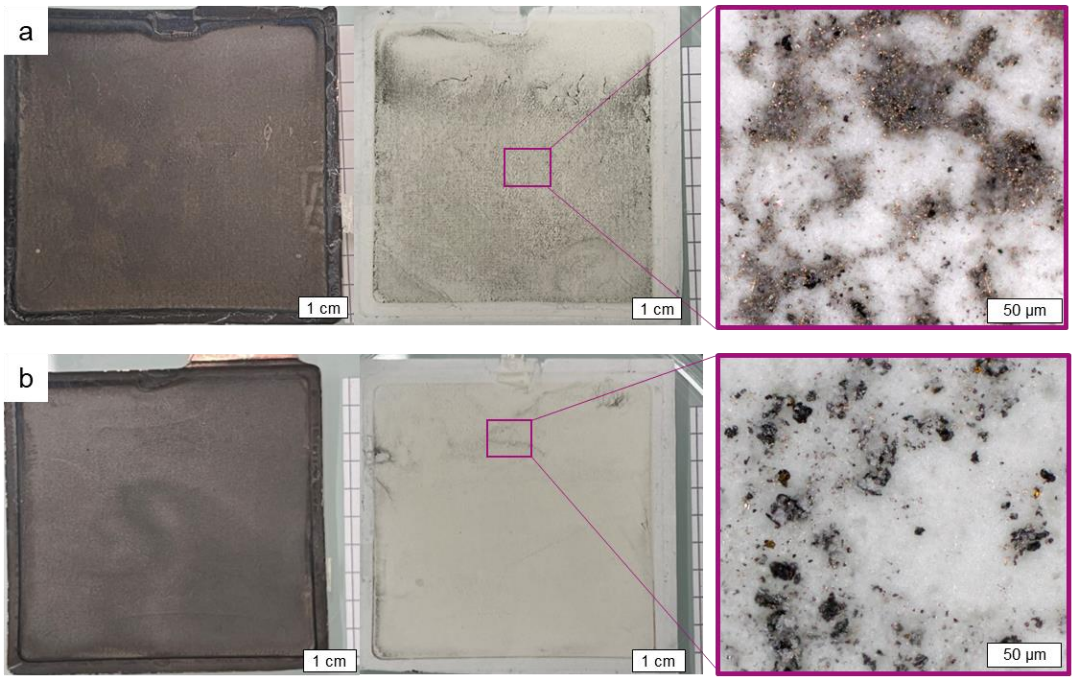

Figure 5.6. Anodes (left column) with CMC (a) and x-PAA (b) binder, and separators (middle and right columns) from the pouch cells disassembled after rate capability test in charge direction.

Long-term cycling was conducted on pouch cells following the rate capability test in the discharge direction, using a 1C charge and 1C discharge protocol. Every 100 cycles, a check-up cycle (C/10) was performed. Figure 5.7a illustrates the long-term cycling performance, displaying the capacity evolution over 1000 cycles for two cells of each anode formulation. The CMC anodes demonstrate superior electrochemical performance in terms of capacity retention, retaining approximately 92 % of their initial capacity after 1000 cycles at 1C. In contrast, anodes containing x-PAA degrade faster than the CMC reference, exhibiting about 87 % of the initial capacity at the same rate and after the same number of cycles. The initial coulombic

efficiencies (ICEs) are 86.2 %, 87.0 % and 87.1 % for cells containing x-PAA, l-PAA, and CMC, respectively. Despite the different molecular structure and molecular weight of the binders, the ICEs remain very similar. This is attributed to the fact that ICE is primarily governed by the active material, and, since both the graphite and electrolyte are identical in all cells, the ICE is largely unaffected by the binder. The binder does not alter the intrinsic electrolyte reduction reactions (SEI formation) but may slightly modulate the fraction of graphite surface exposed to the electrolyte, contributing to minor variations in ICE [208].

While the adsorbed polymer layer may hinder rate performance, it plays a beneficial role during prolonged cycling by shielding the graphite surface. In x-PAA anodes, the absence of such surface coverage increases the susceptibility of the active material to irreversible lithium loss due to ongoing SEI formation. This phenomenon is likely a contributing factor to the accelerated capacity degradation observed in x-PAA cells during long-term cycling. Other possible causes of capacity loss include lithium plating or electrically isolated active material.

Cells incorporating anodes with l-PAA show a significantly lower initial capacity, approximately 2 mAh less, than those utilizing CMC and x-PAA. Furthermore, these l-PAA cells exhibit a substantially stronger capacity decay during cycling, reaching 80 % of capacity retention already after 415 cycles at 1C rate. The data for C/10 (within the check-up every 100 cycles) (Figure 5.7a) shows a very similar trend in capacity decay as the continuous 1C cycling capacity fade, suggesting that the capacity decay is a true loss of active lithium and not an effect of overpotential. The internal resistance measurements are presented in Figure 5.7b at a state of charge (SOC) of 50 %. As expected, the RiDC increases for all cells throughout cycling. Due to the higher content of inactive materials, anodes with l-PAA exhibit the highest absolute internal resistance. In contrast, anodes based on x-PAA, which contain the lowest total binder content, demonstrate the lowest RiDC values.

To obtain a comprehensive understanding of the slightly diminished cycle stability in terms of capacity retention of cells containing x-PAA anodes compared to CMC reference cells, it is necessary to analyze the electrochemical data in conjunction with the post-mortem analysis data presented below.

After 1000 cycles, all cells were discharged and disassembled. The anodes and separators were then rinsed with DMC, dried, and optically inspected. The presence of lithium plating, characterized by silver-grey surface deposits on the anode surface and metallic particles on separators, can be identified only on anodes incorporating l-PAA (see Figure S5.4, Supporting Information). Furthermore, the separators from the cells containing x-PAA and CMC anodes exhibit only minor differences in the quantity of black particle residue, with those from the x-PAA cells exhibiting slightly higher particle accumulation than the CMC reference.

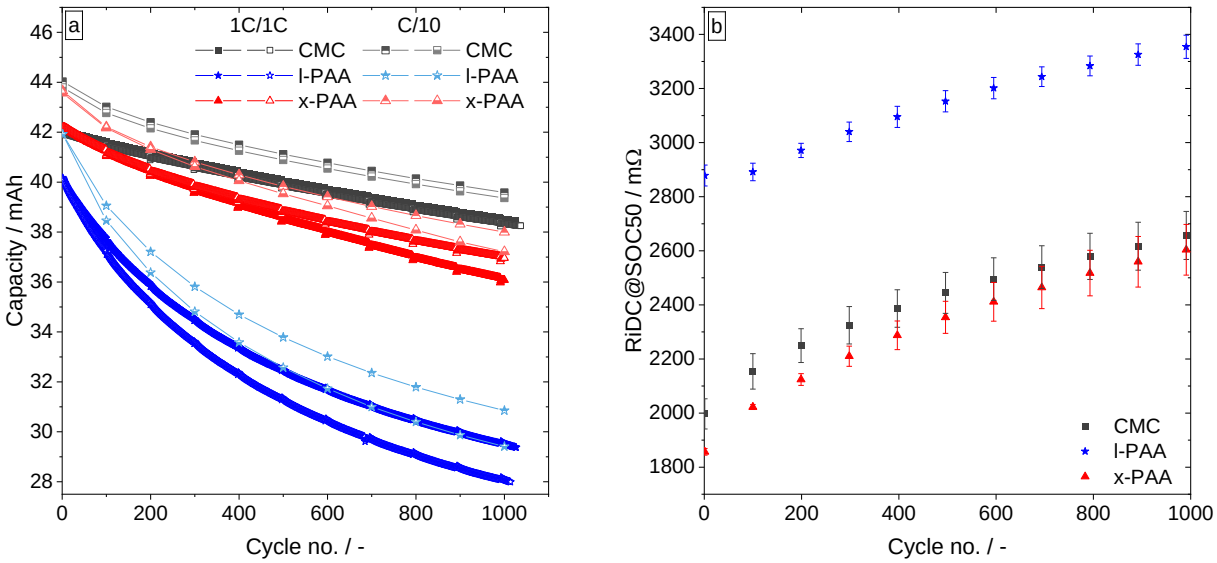

Figure 5.7. Discharge capacity over cycles during 1C/1C charge/discharge (dark colors) and C/10 check-up cycles (light colors) (a); evolution of internal resistance (RiDC) at 50 % SOC (b) for two pouch cells of each anode formulation. Each point in (b) is the average internal resistance value of two cells with anodes of one formulation.

Subsequently, cycled and washed anodes were dried overnight in an oven and subjected to 90°-peel test. A comparison of the pre- and post-cycle line loads of the anodes of each formulation is illustrated in Figure S5.5 (Supporting Information). A significant decline in line load was observed in all electrodes. However, this effect is more pronounced for the CMC anode than for the two PAA based anodes. An examination of the peeled foils again reveals that while the CMC reference indicates clear adhesive failure, cohesive failure is predominant in the case of the x-PAA anodes.

To summarize, electrochemical data obtained from prolonged cycling, when evaluated in conjunction with post-mortem analyses, suggest a consistent mechanism underlying the distinct long-term cycling performance of x-PAA cells compared with the CMC references. Both, post-mortem optical inspection and peel tests indicate that the reduced performance in terms of capacity retention of x-PAA anodes may be attributed to inadequate cohesion of the electrodes. The low amount of non-adsorbing x-PAA binder is unable to fully accommodate the volume changes of the graphite particles due to de-/lithiation. In alignment with the capacity fading being similar at C/10 and 1C, most likely, the greater loss of capacity during long-term cycling for x-PAA containing anodes is due to the electric contact loss of active material.

5.4. Conclusions

In this study, a highly cross-linked commercial acrylate polymer x-PAA Carbopol® Ultrez 10 (Lubrizol, USA) was utilized as a binder for aqueous-processed

graphite anodes. This allowed a substantial reduction of polymeric binder concentration in the anode slurry as well as in the dry electrode layer for two reasons:

i. Due to the high thickening efficiency of this acrylate polymer with its specific heterogeneous gel structure in neutralized aqueous slurries [199], the amount of polymer required for dispersing the active material particles and thickening of the slurry could be reduced without loss in high-shear viscosity. Additionally, x-PAA provides a significant yield stress, which is advantageous for both slurry stability and the formation of well-defined electrode edges during coating.
ii. In contrast to CMC, this acrylate polymer does not adsorb on the graphite particles and thus does not disturb the adhesion between the active material and current collector foil provided by the additionally included soft SBR rubber particles [180]. This resulted in similar line load values as those measured for CMC anode layers but at significantly lower SBR content.

Based on these approaches, the total binder concentration in the dry anode layer was reduced by almost 40 wt%. However, the reduced polymer content leads to a loss of cohesion. As a result, the failure mode in peel tests is pre-dominantly cohesive for the x-PAA anode, whereas adhesive failure dominates for CMC-based anodes, as well as for another reference anode including a much higher amount of linear polyacrylic acid (l-PAA), which was necessary to adjust the processability of the corresponding slurry.

The performance of graphite anodes utilizing x-PAA was evaluated in comparison to two reference formulations employing CMC and l-PAA, respectively. The x-PAA anode exhibited a faster capacity fading during prolonged cycling compared to the CMC reference. After 1000 cycles, cells with x-PAA demonstrate 87 % of their initial capacity, whereas reference cells with CMC show 92 % of capacity retention. This is attributed to the reduced cohesive strength of the anode layer. Pouch cells comprising anodes with l-PAA demonstrated the highest internal resistance due to their high binder content, and the worst cycling performance of all cells, reaching 80% of capacity retention already after 415 cycles. This phenomenon was attributed to the irreversible lithium loss resulting from plating, as revealed through post-mortem analysis.

Furthermore, anodes formulated with x-PAA binder exhibit superior charging rate performance, which is attributed to the absence of an adsorbed polymer layer on the graphite particles, enabling more effective Li^+ insertion and extraction, unlike in anodes incorporating CMC or l-PAA. Notably, CMC-based negative electrodes displayed significant lithium plating after the rate capability test in the charging direction, whereas no lithium deposits were observed in x-PAA-based anodes.

Conclusively, x-PAA proves to be a highly effective binder for graphite anodes, enabling significant reduction of inactive material content. Cells comprising anodes with x-PAA outperform those with CMC and l-PAA under fast-charging conditions. However, a trade-off with long-term cycling stability must be considered. The commercial availability of x-PAA may facilitate cost reduction and enable rapid scaling

up of electrode production in comparison to costly, synthetically produced, and non-commercialized polymers. Future efforts should focus on tailoring the molecular architecture of the binder system, including the degree and distribution of crosslinking, as well as fine-tuning the mechanical properties of the electrode layer in terms of adhesion and cohesion. Presumably, the cohesion-related deficit of the x-PAA anode investigated here could be remedied by using an acrylic acid co-polymer with optimized crosslink architecture, providing similar flow behavior at slightly higher polymer concentration.

5.5 Supporting information

To determine whether x-PAA adsorbs onto graphite, ATR-FTIR spectroscopy was performed on graphite and x-PAA powders, as well as on a dried sample from a graphite/x-PAA dispersion (prepared with the same volume ratio of graphite to x-PAA and pH as the slurry). FTIR Spectrometer (Bruker Tensor 27 FTIR spectrometer, Bruker Optics, Ettlingen GER) equipped with a “Platinum” -ATR internal reflection system (diamond crystal, single reflection) was used to carry out ATR-FTIR analysis in with a bandwidth of 4500–370 cm^{-1}, and the results are displayed in Figure S5.1.

For the x-PAA sample, an intense peak appears at approximately 1700 cm^{-1}, which is assigned as C=O stretching. At a wavenumber of 2932 cm^{-1} a peak corresponding to the C-H stretching of the CH_2 group can be observed. Additionally, a broader peak at around 3230 cm^{-1} is assigned to the hydroxyl group (OH). The absence of characteristic x-PAA peaks in the spectrum of the graphite + x-PAA sample indicates that this polymer does not adsorb onto graphite particles.

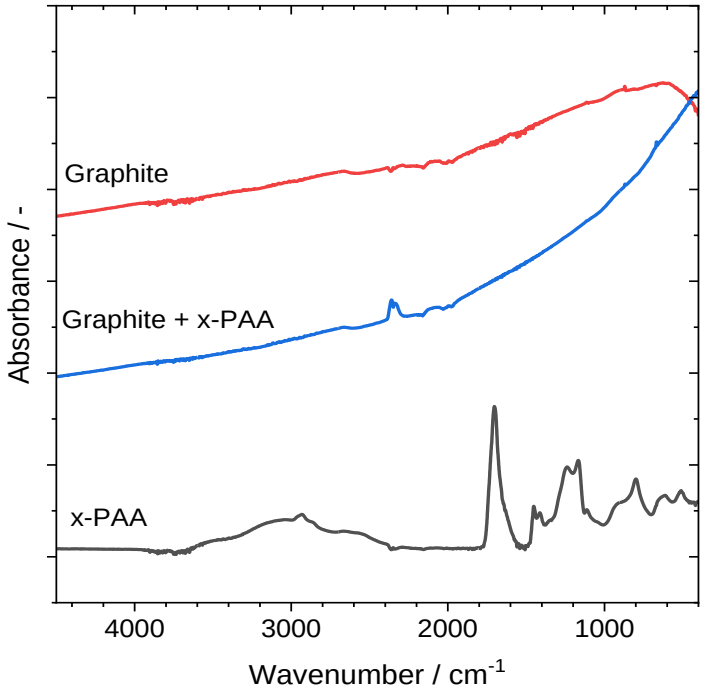

Figure S5.1. ATR-FTIR spectra of graphite, x-PAA, and graphite + x-PAA.

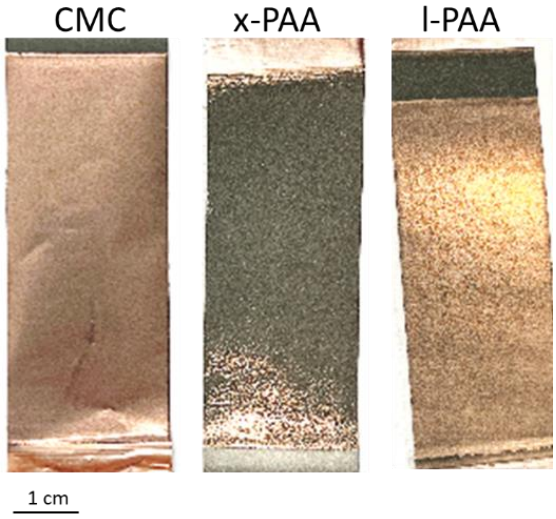

Figure S5.2. Anode samples containing CMC, x-PAA, and l-PAA binder after 90°-peel test. The composition of the anodes is provided in Table 5.1.

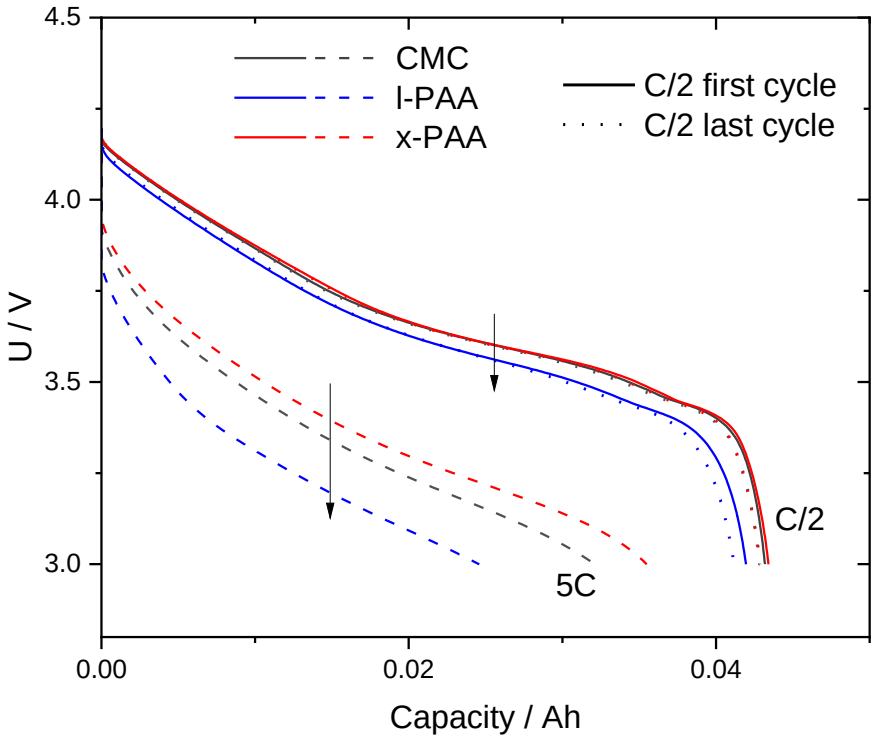

Figure S5.3. Discharge profiles for rates C/2 at first cycle, 5C and C/2 at last cycle for pouch cells containing CMC (black lines), l-PAA (blue lines) and x-PAA (red lines) anodes.

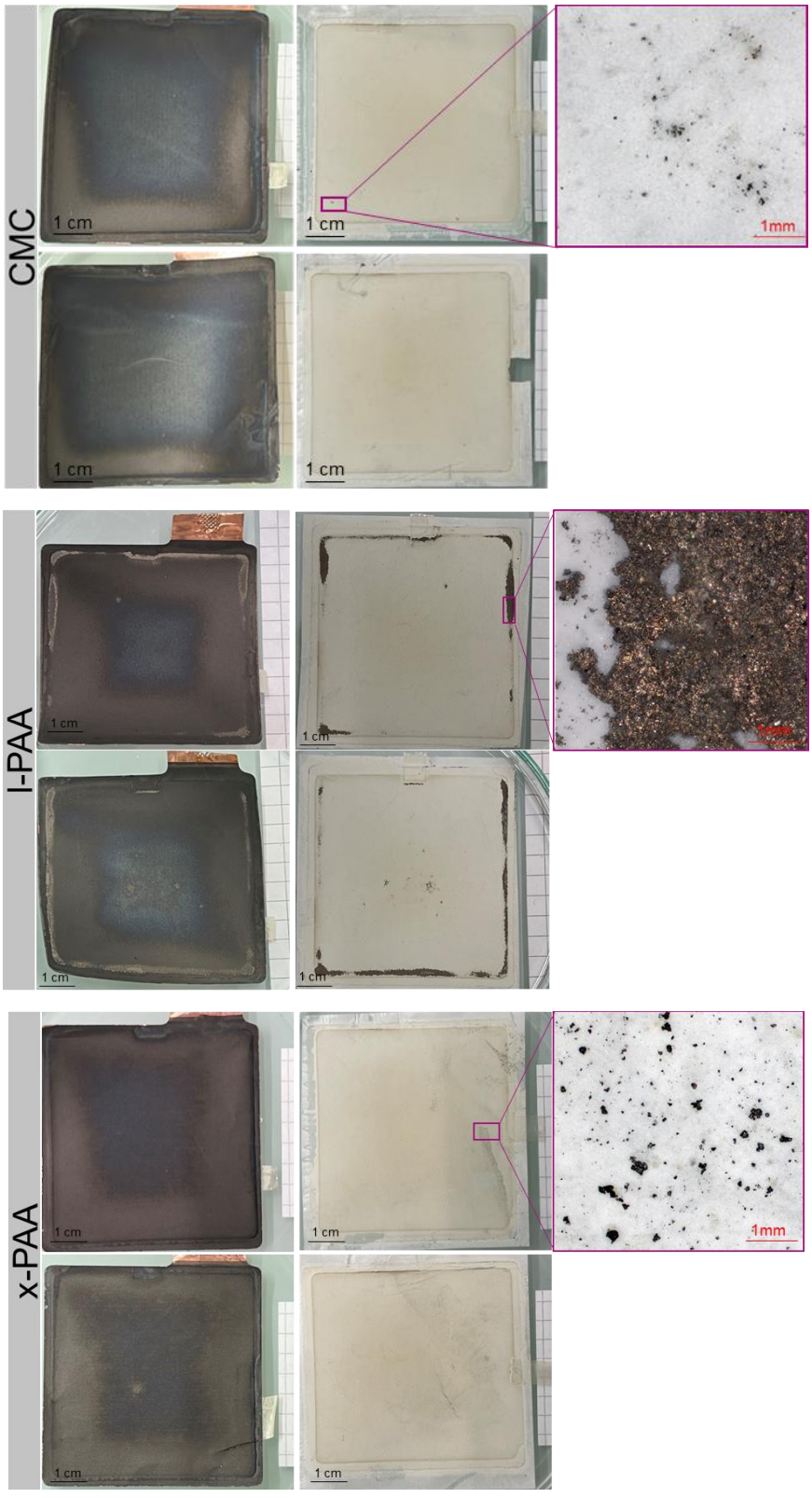

Figure S5.4. Anodes with CMC, l-PAA and x-PAA, and corresponding separators from the pouch cells disassembled after 1000 cycles.

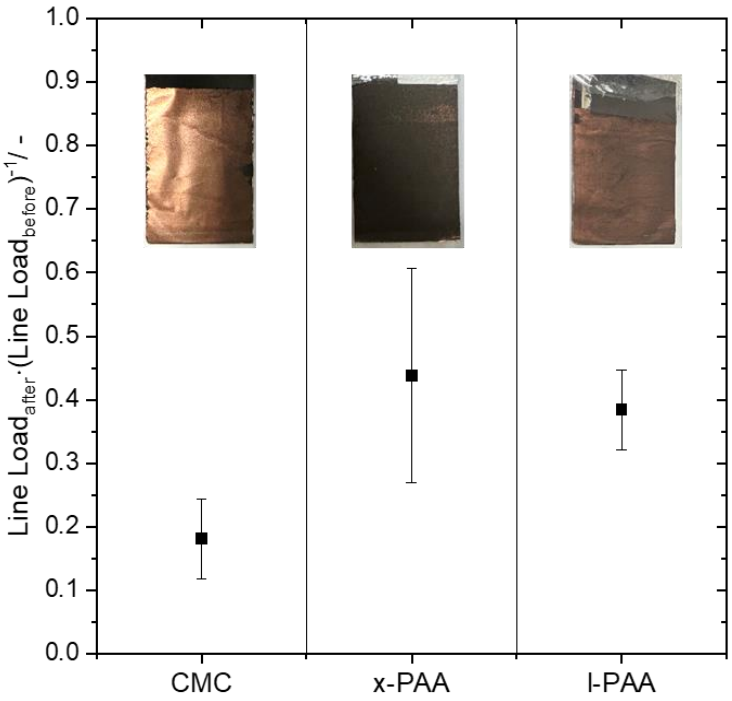

Figure S5.5. The ratio of the line load of cycled and calendered anodes before cycling comprising CMC, x-PAA, and l-PAA binders, and pictures of corresponding electrode samples after the 90°-peel test. The composition of the anodes is provided in Table 5.1.

6. Summary

Since the Industrial Revolution, modern civilization has become heavily reliant on fossil fuels, resulting in an urgent need to counteract global warming and its consequences. The energy transition, which involves transforming sectors such as transport, industry, and agriculture into more sustainable ones, largely relies on LIB technology. Since their commercialization by Sony in 1991, LIBs have revolutionized the world, powering almost everything, from consumer electronics to industrial, medical, and military systems. Their widespread use is largely due to their advantageous features, such as high energy density, long cycle life, and low self-discharge. Nevertheless, LIBs still face significant challenges, particularly with regard to safety, performance, production costs, reliance on critical raw materials, and recycling issues.

Battery efficiency depends greatly on electrode engineering. This thesis, therefore, contributes to develop a comprehensive understanding of the factors controlling binder functionalities in order to create a binder concept that yields anodes with improved processing behavior and electrochemical performance. The work focuses on technically relevant, water-based anode formulations. The main findings of this cumulative dissertation are organized into three sections, each corresponding to a peer-reviewed scientific paper.

The role of styrene butadiene rubber (SBR) in aqueous-processed graphite anodes and its influence on mechanical properties, processability, and electrochemical behavior was systematically studied in section 3. Graphite anodes with application-relevant mass loadings (5.7 and 10.1 mg cm^{-2}) were prepared with varying SBR contents (0–4.5 wt%) and subjected to comprehensive mechanical and electrochemical testing to determine the optimal adhesion level that ensures failure-free processing without compromising the electrochemical performance. The addition of SBR not only exponentially increases the adhesion of the anode layer to the copper current collector but also leads to a linear increase in layer cohesion. Bending tests revealed that crack formation occurred only in non-calendered, thick anode layers (10.1 mg cm^{-1}) without SBR, which exhibited the lowest cohesion and adhesion. During winding tests, which impose greater stresses on electrode layers compared to bending, crack formation occurred regardless of adhesion strength, with more pronounced cracking at higher mass loadings. A clear trend was observed during anode punching and cutting: higher adhesion directly correlates with reduced particle abrasion and coating delamination. Rate capability tests in full-cell pouch configuration showed the expected behavior, with cell capacity declining markedly at both lower and higher mass loadings as C-rate and SBR concentration increased. This effect is attributed to higher internal resistance caused by the greater fraction of electrochemically inactive SBR. Prolonged cycling revealed, contrary to expectations regarding an eventual roll-over effect, that anodes with low SBR contents and therefore very low adhesive strength exhibited remarkable cycling stability. This suggests that CMC alone or in combination

with minimal SBR content is sufficient to preserve the mechanical integrity of the electrode during operation. Furthermore, higher SBR amounts and greater anode mass loadings resulted in more severe capacity degradation and pronounced lithium plating. The adhesive strength of cycled anodes, measured in 90°-peel tests, showed a sharp decline to about 10–20 % of the initial value, irrespective of mass loading and SBR content, which may result from mechanical degradation and decomposition of SBR due to prolonged cycling. In this study, the optimal adhesion of non-calendered 5.7 and 10.1 mg cm^{-2} anodes, ensuring both reliable processability and stable cycling performance, was determined to be 4.6 and 5.8 N m^{-1}, respectively, corresponding to 1.5 wt% SBR in the anode layer.

In Section 4, the effect of CMC, actually included as a thickening and dispersing agent, on the adhesion strength of electrodes was examined. CMC itself does not provide adhesion, which is instead promoted by SBR. Adhesion strength between SBR and individual electrode components was assessed in 90°-peel tests. The strongest interfacial bonding was observed between SBR and graphite, followed by SBR and quartz glass (used as an equivalent surface for the silicon active material). The weakest bonding occurred between SBR and CMC, which was significantly lower than the adhesion between SBR and copper current collector. These results indicate that delamination of the active material layer from the current collector is likely to occur at the SBR–CMC interface, where CMC adsorbs onto active material surfaces. This suggests that the adsorbed CMC layer may act as a barrier, hindering strong adhesion between active particles and the copper foil. To investigate the adsorption behavior of CMC on three different anode active materials: graphite, micro-sized silicon, and nano-sized silicon particles, as a function of CMC M_w, a rheological approach was applied. CMC showed the highest affinity for micro-sized silicon surface, followed by graphite, and the lowest affinity for the nano-silicon. Based on the peel test results of SBR films with individual electrode components and the CMC adsorption data, graphite and silicon composite anodes were prepared using three different CMC molecular weights while maintaining constant SBR concentration, and their adhesion was evaluated using 90°-peel tests. Increasing CMC M_w, which correlates with greater adsorption on active material surfaces, led to reduced line load for both graphite and graphite–micro-silicon composite anodes. In contrast, replacing CMC with a non-adsorbing polymer thickener significantly improved graphite anode adhesion, attributable to the strong direct contact between active material particles and the SBR polymer. Furthermore, the microstructure of active material particles was found to strongly affect anode adhesion. SBR can diffuse into nano-silicon agglomerates and become trapped, resulting in very low adhesion for graphite–nano-silicon composite anodes despite minimal CMC adsorption on nano-silicon surfaces.

Building on these findings, a tailored binder system based on a highly cross-linked acrylate binder (Carbopol® Ultrez10, x-PAA) combined with SBR was evaluated (section 5) for high-performance graphite anodes. The commercial availability of x-PAA offers a cost-effective and scalable alternative to expensive, synthetically produced, and non-commercialized binder systems. Owing to the strong thickening properties of

x-PAA in neutralized water-based slurries, the polymer content required for homogeneous particle dispersion and thickening the slurry could be reduced by nearly 40 wt% (relative to the dry electrode layer) without compromising high-shear viscosity. Rheological measurements further revealed that x-PAA-based anode slurries exhibit a pronounced yield stress, beneficial for slurry stability. Unlike CMC and linear PAA (l-PAA), x-PAA does not adsorb onto graphite particles, as confirmed by ATR-FTIR spectroscopy. Consequently, x-PAA does not disturb the adhesion between the anode active layer and the copper current collector, provided by the additionally included SBR binder. As a result, line load values similar to those of CMC-based anodes were achieved, but at significantly lower SBR content. The electrochemical performance of x-PAA, CMC, and l-PAA anodes was evaluated in a full-cell pouch configuration. Cells with x-PAA anodes demonstrated superior charging rate capability, attributed to the absence of an adsorbed polymer layer on active material particles, which facilitates more efficient Li-ion insertion and extraction compared with CMC- or l-PAA-based anodes. CMC-based reference negative electrodes displayed significant lithium plating after the rate capability test in the charging direction, whereas no lithium deposits were observed in x-PAA anodes. Nevertheless, the substantially lower binder content of x-PAA anodes resulted in reduced cohesion, causing faster capacity fading during prolonged cycling relative to the CMC reference.

In summary, this thesis provides a basis for tailoring electrode processing behavior and optimizing the electrode mechanical and thus electrochemical properties through the targeted selection of polymeric binders. A comprehensive understanding of the interactions between binders and active particles, as well as among the binders themselves, is developed, and it is shown that these binder functionalities directly influence the electrochemical performance of the cell. On this basis, a binder formulation concept is proposed that enables the fabrication of anodes for lithium-ion batteries with enhanced electrochemical performance, thereby contributing to more efficient and durable energy storage solutions. The work is carried out under technically relevant conditions, employing commercially available polymeric binders rather than costly synthesis approaches, thus allowing for rapid scalability and cost reduction.

7. Outlook

Despite extensive study on the relationship between polymeric binder–controlled electrode properties and cell electrochemical performance, several open questions remain based on the findings presented here.

Adhesion measurements of cycled graphite anodes revealed a significant decline in electrode adhesion after prolonged cycling. However, it remains unclear whether this decrease is caused by chemical or mechanical degradation of the SBR binder. If SBR decomposition occurs, it is important to investigate how the resulting products interact with the electrolyte, influence SEI formation and/or composition, and ultimately affect cycling stability. Nuclear magnetic resonance (NMR) spectroscopy could serve as a potential method to study possible SBR degradation and its effects.

In the pursuit of higher battery capacities, silicon-based active materials are of particular interest. It would be valuable to assess how adhesion strength impacts the processability and electrochemical performance of silicon-containing anodes, and whether the findings obtained for graphite anodes are transferable to silicon-based systems.

Future work on binder design for graphite anodes should aim to enhance cohesion and overall electrode integrity. One possible approach is the use of an acrylic acid co-polymer with optimized cross-linking architecture, which could maintain favorable flow properties while allowing slightly higher polymer concentrations, thereby improving electrode stability and performance. Additionally, it will be interesting to evaluate how the proposed binder concept based on Carbopol polymer performs in silicon-containing anodes.

References

[1] Kennedy J, Trewin B, Betts R, Thorne P, Foster P, Siegmund P, et al. State of the Climate 2024. Update for COP29 2024.

[2] Copernicus Climate Change Service (C3S) and World Meteorological Organization (WMO). European State of the Climate 2024 2025. https://doi.org/doi.org/10.24381/14j9-s541.

[3] Change C. Synthesis Report Summary for Policymakers, IPCC. Intergov Panel Clim Chang Geneva IPCC 2014.

[4] Salah M, Murphy P, Hall C, Francis C, Kerr R, Fabretto M. Pure silicon thin-film anodes for lithium-ion batteries: A review. J Power Sources 2019;414:48–67. https://doi.org/10.1016/j.jpowsour.2018.12.068.

[5] Zhang Z, Wu Y, Mo Z, Lei X, Xie X, Xue X, et al. Research progress of silicon-based anode materials for lithium-ion batteries. RSC Adv 2025;15:10731–53. https://doi.org/10.1039/D5RA01268F.

[6] Xu B, Qian D, Wang Z, Meng YS. Recent progress in cathode materials research for advanced lithium ion batteries. Mater Sci Eng R Rep 2012;73:51–65. https://doi.org/10.1016/j.mser.2012.05.003.

[7] Weber M, Mayer JK, Kwade A. The Carbon Black Dispersion Index DI_{CB} : A Novel Approach Describing the Dispersion Progress of Carbon Black Containing Battery Slurries. Energy Technol 2023;11:2201299. https://doi.org/10.1002/ente.202201299.

[8] Entwistle J, Ge R, Pardikar K, Smith R, Cumming D. Carbon binder domain networks and electrical conductivity in lithium-ion battery electrodes: A critical review. Renew Sustain Energy Rev 2022;166:112624. https://doi.org/10.1016/j.rser.2022.112624.

[9] Bauer W, Nötzel D, Wenzel V, Nirschl H. Influence of dry mixing and distribution of conductive additives in cathodes for lithium ion batteries. J Power Sources 2015;288:359–67. https://doi.org/10.1016/j.jpowsour.2015.04.081.

[10] Spahr ME, Goers D, Leone A, Stallone S, Grivei E. Development of carbon conductive additives for advanced lithium ion batteries. J Power Sources 2011;196:3404–13. https://doi.org/10.1016/j.jpowsour.2010.07.002.

[11] Wypych G. 5 - Physical Properties of Fillers and Filled Materials. In: Wypych G, editor. Handb. Fill. Fourth Ed., ChemTec Publishing; 2016, p. 303–71. https://doi.org/10.1016/B978-1-895198-91-1.50007-5.

[12] Miyasaka K, Watanabe K, Jojima E, Aida H, Sumita M, Ishikawa K. Electrical conductivity of carbon-polymer composites as a function of carbon content. J Mater Sci 1982;17:1610–6. https://doi.org/10.1007/BF00540785.

[13] Wang C-W, Cook KA, Sastry AM. Conduction in Multiphase Particulate/Fibrous Networks : Simulations and Experiments on Li-ion Anodes. J Electrochem Soc 2003;150:A385. https://doi.org/10.1149/1.1543566.

[14] de Rijk TM, Lang W. Low-Cost and Highly Sensitive Pressure Sensor with Mold-Printed Multi-Walled Carbon Nanotubes Dispersed in Polydimethylsiloxane. Sensors 2021;21:5069. https://doi.org/10.3390/s21155069.

[15] Liu G, Zheng H, Kim S, Deng Y, Minor AM, Song X, et al. Effects of Various Conductive Additive and Polymeric Binder Contents on the Performance of a Lithium-Ion Composite Cathode. J Electrochem Soc 2008;155:A887. https://doi.org/10.1149/1.2976031.
[16] Meyer C, Weyhe M, Haselrieder W, Kwade A. Heated Calendering of Cathodes for Lithium-Ion Batteries with Varied Carbon Black and Binder Contents. Energy Technol 2020;8:1900175. https://doi.org/10.1002/ente.201900175.
[17] Qi X, Blizanac B, DuPasquier A, Oljaca M, Li J, Winter M. Understanding the influence of conductive carbon additives surface area on the rate performance of LiFePO4 cathodes for lithium ion batteries. Carbon 2013;64:334–40. https://doi.org/10.1016/j.carbon.2013.07.083.
[18] Bard AJ, Parsons R, Jordan J. Standard Potentials in Aqueous Solution. Routledge; 2017.
[19] Yamada M, Watanabe T, Gunji T, Wu J, Matsumoto F. Review of the Design of Current Collectors for Improving the Battery Performance in Lithium-Ion and Post-Lithium-Ion Batteries. Electrochem 2020;1:124–59. https://doi.org/10.3390/electrochem1020011.
[20] Koech AK, Mwandila G, Mulolani F, Mwaanga P. Lithium-ion battery fundamentals and exploration of cathode materials: A review. South Afr J Chem Eng 2024;50:321–39. https://doi.org/10.1016/j.sajce.2024.09.008.
[21] Wu Y. Lithium-Ion Batteries: Fundamentals and Applications. CRC Press; 2015.
[22] Korthauer R. Lithium-Ion Batteries: Basics and Applications. Springer; 2018.
[23] Nitta N, Yushin G. High-Capacity Anode Materials for Lithium-Ion Batteries: Choice of Elements and Structures for Active Particles. Part Part Syst Charact 2014;31:317–36. https://doi.org/10.1002/ppsc.201300231.
[24] Chung DDL. Review Graphite. J Mater Sci 2002;37:1475–89. https://doi.org/10.1023/A:1014915307738.
[25] Winter M, Besenhard JO, Spahr ME, Novák P. Insertion Electrode Materials for Rechargeable Lithium Batteries. Adv Mater 1998;10:725–63. https://doi.org/10.1002/(SICI)1521-4095(199807)10:10%253C725::AID-ADMA725%253E3.0.CO;2-Z.
[26] Velický M, Toth PS, Woods CR, Novoselov KS, Dryfe RAW. Electrochemistry of the Basal Plane versus Edge Plane of Graphite Revisited. J Phys Chem C 2019;123:11677–85. https://doi.org/10.1021/acs.jpcc.9b01010.
[27] Primak W, Fuchs LH. Electrical Conductivities of Natural Graphite Crystals. Phys Rev 1954;95:22–30. https://doi.org/10.1103/PhysRev.95.22.
[28] Tran T, Kinoshita K. Lithium intercalation/deintercalation behavior of basal and edge planes of highly oriented pyrolytic graphite and graphite powder. J Electroanal Chem 1995;386:221–4. https://doi.org/10.1016/0022-0728(95)03907-X.
[29] Dahn JR, Zheng T, Liu Y, Xue JS. Mechanisms for Lithium Insertion in Carbonaceous Materials. Science 1995;270:590–3. https://doi.org/10.1126/science.270.5236.590.

[30] Billaud D, McRae E, Hérold A. Synthesis and electrical resistivity of lithium-pyrographite intercalation compounds (stages I, II and III). Mater Res Bull 1979;14:857–64.
[31] Li H, Yamaguchi T, Matsumoto S, Hoshikawa H, Kumagai T, Okamoto NL, et al. Circumventing huge volume strain in alloy anodes of lithium batteries. Nat Commun 2020;11:1584. https://doi.org/10.1038/s41467-020-15452-0.
[32] Asenbauer J, Eisenmann T, Kuenzel M, Kazzazi A, Chen Z, Bresser D. The success story of graphite as a lithium-ion anode material – fundamentals, remaining challenges, and recent developments including silicon (oxide) composites. Sustain Energy Fuels 2020;4:5387–416. https://doi.org/10.1039/D0SE00175A.
[33] Wang R, Wang L, Liu R, Li X, Wu Y, Ran F. “Fast-Charging” Anode Materials for Lithium-Ion Batteries from Perspective of Ion Diffusion in Crystal Structure. ACS Nano 2024;18:2611–48. https://doi.org/10.1021/acsnano.3c08712.
[34] Gu M, He Y, Zheng J, Wang C. Nanoscale silicon as anode for Li-ion batteries: The fundamentals, promises, and challenges. Nano Energy 2015;17:366–83. https://doi.org/10.1016/j.nanoen.2015.08.025.
[35] Boukamp BA, Lesh GC, Huggins RA. All-Solid Lithium Electrodes with Mixed-Conductor Matrix. J Electrochem Soc 1981;128:725–9. https://doi.org/10.1149/1.2127495.
[36] Pollak E, Salitra G, Baranchugov V, Aurbach D. In Situ Conductivity, Impedance Spectroscopy, and Ex Situ Raman Spectra of Amorphous Silicon during the Insertion/Extraction of Lithium. J Phys Chem C 2007;111:11437–44. https://doi.org/10.1021/jp0729563.
[37] Xie J, Imanishi N, Zhang T, Hirano A, Takeda Y, Yamamoto O. Li-ion diffusion in amorphous Si films prepared by RF magnetron sputtering: A comparison of using liquid and polymer electrolytes. Mater Chem Phys 2010;120:421–5. https://doi.org/10.1016/j.matchemphys.2009.11.031.
[38] Beaulieu LY, Hatchard TD, Bonakdarpour A, Fleischauer MD, Dahn JR. Reaction of Li with Alloy Thin Films Studied by In Situ AFM. J Electrochem Soc 2003;150:A1457. https://doi.org/10.1149/1.1613668.
[39] Obrovac MN, Chevrier VL. Alloy Negative Electrodes for Li-Ion Batteries. Chem Rev 2014;114:11444–502. https://doi.org/10.1021/cr500207g.
[40] McDowell MT, Lee SW, Nix WD, Cui Y. 25th Anniversary Article: Understanding the Lithiation of Silicon and Other Alloying Anodes for Lithium-Ion Batteries. Adv Mater 2013;25:4966–85. https://doi.org/10.1002/adma.201301795.
[41] Rhodes K, Dudney N, Lara-Curzio E, Daniel C. Understanding the Degradation of Silicon Electrodes for Lithium-Ion Batteries Using Acoustic Emission. J Electrochem Soc 2010;157:A1354. https://doi.org/10.1149/1.3489374.
[42] Ge M, Rong J, Fang X, Zhang A, Lu Y, Zhou C. Scalable preparation of porous silicon nanoparticles and their application for lithium-ion battery anodes. Nano Res 2013;6:174–81. https://doi.org/10.1007/s12274-013-0293-y.

[43] Yang Y, Yuan W, Kang W, Ye Y, Yuan Y, Qiu Z, et al. Silicon-nanoparticle-based composites for advanced lithium-ion battery anodes. Nanoscale 2020;12:7461–84. https://doi.org/10.1039/C9NR10652A.
[44] Chan CK, Peng H, Liu G, McIlwrath K, Zhang XF, Huggins RA, et al. High-performance lithium battery anodes using silicon nanowires. Nat Nanotechnol 2008;3:31–5. https://doi.org/10.1038/nnano.2007.411.
[45] Jeong S, Lee J-P, Ko M, Kim G, Park S, Cho J. Etched Graphite with Internally Grown Si Nanowires from Pores as an Anode for High Density Li-Ion Batteries. Nano Lett 2013;13:3403–7. https://doi.org/10.1021/nl401836c.
[46] Park M-H, Kim MG, Joo J, Kim K, Kim J, Ahn S, et al. Silicon Nanotube Battery Anodes. Nano Lett 2009;9:3844–7. https://doi.org/10.1021/nl902058c.
[47] Cui L-F, Hu L, Choi JW, Cui Y. Light-Weight Free-Standing Carbon Nanotube-Silicon Films for Anodes of Lithium Ion Batteries. ACS Nano 2010;4:3671–8. https://doi.org/10.1021/nn100619m.
[48] Dimov N, Kugino S, Yoshio M. Carbon-coated silicon as anode material for lithium ion batteries: advantages and limitations. Electrochimica Acta 2003;48:1579–87. https://doi.org/10.1016/S0013-4686(03)00030-6.
[49] Chan CK, Patel RN, O'Connell MJ, Korgel BA, Cui Y. Solution-Grown Silicon Nanowires for Lithium-Ion Battery Anodes. ACS Nano 2010;4:1443–50. https://doi.org/10.1021/nn901409q.
[50] Zhang X, Wang D, Qiu X, Ma Y, Kong D, Müllen K, et al. Stable high-capacity and high-rate silicon-based lithium battery anodes upon two-dimensional covalent encapsulation. Nat Commun 2020;11:3826. https://doi.org/10.1038/s41467-020-17686-4.
[51] Shin H-J, Hwang J-Y, Kwon HJ, Kwak W-J, Kim S-O, Kim H-S, et al. Sustainable Encapsulation Strategy of Silicon Nanoparticles in Microcarbon Sphere for High-Performance Lithium-Ion Battery Anode. ACS Sustain Chem Eng 2020;8:14150–8. https://doi.org/10.1021/acssuschemeng.0c04828.
[52] Liu J, Yang Y, Lyu P, Nachtigall P, Xu Y. Few-Layer Silicene Nanosheets with Superior Lithium-Storage Properties. Adv Mater 2018;30:1800838. https://doi.org/10.1002/adma.201800838.
[53] Ryu J, Hong D, Choi S, Park S. Synthesis of Ultrathin Si Nanosheets from Natural Clays for Lithium-Ion Battery Anodes. ACS Nano 2016;10:2843–51. https://doi.org/10.1021/acsnano.5b07977.
[54] Salini PS, Gopinadh SV, Kalpakasseri A, John B, Thelakkattu Devassy M. Toward Greener and Sustainable Li-Ion Cells: An Overview of Aqueous-Based Binder Systems. ACS Sustain Chem Eng 2020;8:4003–25. https://doi.org/10.1021/acssuschemeng.9b07478.
[55] Cholewinski A, Si P, Uceda M, Pope M, Zhao B. Polymer Binders: Characterization and Development toward Aqueous Electrode Fabrication for Sustainability. Polymers 2021;13. https://doi.org/10.3390/polym13040631.
[56] Ma Y, Ma J, Cui G. Small things make big deal: Powerful binders of lithium batteries and post-lithium batteries. Energy Storage Mater 2019;20:146–75. https://doi.org/10.1016/j.ensm.2018.11.013.

[57] Jin-Hyon Lee, Ungyu Paik, Vincent A. Hackley, Young-Min Choi. Effect of carboxymethyl cellulose on aqueous processing of natural graphite negative electrodes and their electrochemical performance for lithium batteries. J Electrochem Soc 2005;152.9. https://doi.org/10.1149/1.1979214.
[58] Kwon T-W, Choi JW, Coskun A. The emerging era of supramolecular polymeric binders in silicon anodes. Chem Soc Rev 2018;47:2145–64. https://doi.org/10.1039/c7cs00858a.
[59] Bridel J-S, Azaïs T, Morcrette M, Tarascon J-M, Larcher D. In Situ Observation and Long-Term Reactivity of Si/C/CMC Composites Electrodes for Li-Ion Batteries. J Electrochem Soc 2011;158:750–9. https://doi.org/10.1149/1.3581024.
[60] N. S. Hochgatterer, M. R. Schweiger, S. Koller, P. R. Raimann, T. Wöhrle, C. Wurm, M. Winter. Silicon/graphite composite electrodes for high-capacity anodes: influence of binder chemistry on cycling stability. Electrochem Solid-State Lett 2008;11:76. https://doi.org/10.1149/1.2888173.
[61] D. Mazouzi, B. Lestriez, L.Roué, D.Guyomard. Silicon Composite Electrode with High Capacity and Long Cycle Life. Electrochem Solid-State Lett 2009:215. https://doi.org/10.1149/1.3212894.
[62] Gordon R, Orias R, Willenbacher N. Effect of carboxymethyl cellulose on the flow behavior of lithium-ion battery anode slurries and the electrical as well as mechanical properties of corresponding dry layers. J Mater Sci 2020;55:15867–81. https://doi.org/10.1007/s10853-020-05122-3.
[63] Kim KJ, Ahn KH. Effect of carboxymethyl cellulose on silicon dispersion and the performance of graphite/Si-based electrodes for lithium-ion batteries. Powder Technol 2025;452:120452. https://doi.org/10.1016/j.powtec.2024.120452.
[64] Park JH, Kim SH, Ahn KH. Role of carboxymethyl cellulose binder and its effect on the preparation process of anode slurries for Li-ion batteries. Colloids Surf Physicochem Eng Asp 2023;664:131130. https://doi.org/10.1016/j.colsurfa.2023.131130.
[65] Kim KJ, Ahn KH. The Effect of Molecular Weight of Carboxymethyl Cellulose on the Dispersion of Silicon Suspensions Investigated by the Ultrasonic Degradation Method. Nihon Reoroji Gakkaishi 2024;52:1–13. https://doi.org/10.1678/rheology.52.1.
[66] Lim S, Kim S, Ahn KH, Lee SJ. The effect of binders on the rheological properties and the microstructure formation of lithium-ion battery anode slurries. J Power Sources 2015;299:221–30. https://doi.org/10.1016/j.jpowsour.2015.09.009.
[67] Obrecht W, Lambert J, Happ M, Oppenheimer-Stix C, Dunn J, Krüger R. Rubber, 4. Emulsion Rubbers. In: Wiley-VCH, editor. Ullmanns Encycl. Ind. Chem. 1st ed., Wiley; 2011. https://doi.org/10.1002/14356007.o23_o01.
[68] Wei L, Chen C, Hou Z, Wei H. Poly (acrylic acid sodium) grafted carboxymethyl cellulose as a high performance polymer binder for silicon anode in lithium ion batteries. Sci Rep 2016;6:19583. https://doi.org/10.1038/srep19583.
[69] Huang Q, Wan C, Loveridge M, Bhagat R. Partially Neutralized Polyacrylic Acid/Poly(vinyl alcohol) Blends as Effective Binders for High-Performance

Silicon Anodes in Lithium-Ion Batteries. ACS Appl Energy Mater 2018;1:6890–8. https://doi.org/10.1021/acsaem.8b01277.

[70] Zhu L, Du F, Zhuang Y, Dai H, Cao H, Adkins J, et al. Effect of crosslinking binders on Li-storage behavior of silicon particles as anodes for lithium ion batteries. J Electroanal Chem 2019;845:22–30. https://doi.org/10.1016/j.jelechem.2019.05.019.

[71] Liu Y, Zhang R, Wang J, Wang Y. Current and future lithium-ion battery manufacturing. iScience 2021;24:102332. https://doi.org/10.1016/j.isci.2021.102332.

[72] Kwade A, Haselrieder W, Leithoff R, Modlinger A, Dietrich F, Droeder K. Current status and challenges for automotive battery production technologies. Nat Energy 2018;3:290–300. https://doi.org/10.1038/s41560-018-0130-3.

[73] Li J, Fleetwood J, Hawley WB, Kays W. From Materials to Cell: State-of-the-Art and Prospective Technologies for Lithium-Ion Battery Electrode Processing. Chem Rev 2022;122:903–56. https://doi.org/10.1021/acs.chemrev.1c00565.

[74] Eirich Machines, Inc. Innovative mixing technology in LiB electrode production [White paper] 2024. https://www.eirichusa.com/fileadmin/user_upload/Eirich_Machines/Brochures/Technical_Articles/Innovative_mixing_technology_in_LiB_electrode_production_June2024.pdf (accessed November 11, 2025).

[75] Jaiser S, Müller M, Baunach M, Bauer W, Scharfer P, Schabel W. Investigation of film solidification and binder migration during drying of Li-Ion battery anodes. J Power Sources 2016;318:210–9. https://doi.org/10.1016/j.jpowsour.2016.04.018.

[76] Jaiser S, Kumberg J, Klaver J, Urai JL, Schabel W, Schmatz J, et al. Microstructure formation of lithium-ion battery electrodes during drying – An ex-situ study using cryogenic broad ion beam slope-cutting and scanning electron microscopy (Cryo-BIB-SEM). J Power Sources 2017;345:97–107. https://doi.org/10.1016/j.jpowsour.2017.01.117.

[77] Müller M, Pfaffmann L, Jaiser S, Baunach M, Trouillet V, Scheiba F, et al. Investigation of binder distribution in graphite anodes for lithium-ion batteries. J Power Sources 2017;340:1–5. https://doi.org/10.1016/j.jpowsour.2016.11.051.

[78] Klemens J, Schneider L, Herbst EC, Bohn N, Müller M, Bauer W, et al. Drying of NCM Cathode Electrodes with Porous, Nanostructured Particles Versus Compact Solid Particles: Comparative Study of Binder Migration as a Function of Drying Conditions. Energy Technol 2022;10:2100985. https://doi.org/10.1002/ente.202100985.

[79] Kumano N, Yamaguchi Y, Akimoto Y, Ohshima A, Nakamura H, Yamamura M. Migration of binder and conductive agent during drying process of Li-ion battery cathodes. J Power Sources 2024;591:233883. https://doi.org/10.1016/j.jpowsour.2023.233883.

[80] Bryntesen SN, Strømman AH, Tolstorebrov I, Shearing PR, Lamb JJ, Stokke Burheim O. Opportunities for the State-of-the-Art Production of LIB Electrodes—A Review. Energies 2021;14:1406. https://doi.org/10.3390/en14051406.

[81] Tao R, Gu Y, Du Z, Lyu X, Li J. Advanced electrode processing for lithium-ion battery manufacturing. Nat Rev Clean Technol 2025;1:116–31. https://doi.org/10.1038/s44359-024-00018-w.
[82] Abdollahifar M, Cavers H, Scheffler S, Diener A, Lippke M, Kwade A. Insights into Influencing Electrode Calendering on the Battery Performance. Adv Energy Mater 2023;13:2300973. https://doi.org/10.1002/aenm.202300973.
[83] Rieder P, Furat O, Usseglio-Viretta FL, Allen J, Weddle PJ, Finegan DP, et al. Stochastic 3D reconstruction of cracked polycrystalline NMC particles using 2D SEM data. Npj Comput Mater 2025;11:232.
[84] Heimes HH, Kampker A, Lienemann C, Locke M, Offermanns C, Michaelis S, et al. Lithium-ion battery cell production process. Aachen: PEM der RWTH Aachen University; 2018.
[85] Beck D, Dechent P, Junker M, Sauer DU, Dubarry M. Inhomogeneities and Cell-to-Cell Variations in Lithium-Ion Batteries, a Review. Energies 2021;14:3276. https://doi.org/10.3390/en14113276.
[86] Liang Y, Zhao C, Yuan H, Chen Y, Zhang W, Huang J, et al. A review of rechargeable batteries for portable electronic devices. InfoMat 2019;1:6–32. https://doi.org/10.1002/inf2.12000.
[87] Birkl CR, McTurk E, Roberts MR, Bruce PG, Howey DA. A Parametric Open Circuit Voltage Model for Lithium Ion Batteries. J Electrochem Soc 2015;162:A2271–80. https://doi.org/10.1149/2.0331512jes.
[88] Park J-K. Principles and Applications of Lithium Secondary Batteries. John Wiley & Sons; 2012.
[89] Tomaszewska A, Chu Z, Feng X, O'Kane S, Liu X, Chen J, et al. Lithium-ion battery fast charging: A review. eTransportation 2019;1:100011. https://doi.org/10.1016/j.etran.2019.100011.
[90] Adejare AA, Okemakinde FE, Tingbari VM, Lee J, Kim J. Comparative Analysis of Charging Protocol for Degradation Reduction and Remaining-Useful-Life Enhancement of a Lithium-Ion Battery. Energy Technol 2024:2400584. https://doi.org/10.1002/ente.202400584.
[91] Heubner C, Nikolowski K, Reuber S, Schneider M, Wolter M, Michaelis A. Recent Insights into Rate Performance Limitations of Li-ion Batteries. Batter Supercaps 2021;4:268–85. https://doi.org/10.1002/batt.202000227.
[92] Passerini S, Bresser D, Moretti A, Varzi A. Batteries: Present and Future Energy Storage Challenges. John Wiley & Sons; 2020.
[93] Birkl CR, Roberts MR, McTurk E, Bruce PG, Howey DA. Degradation diagnostics for lithium ion cells. J Power Sources 2017;341:373–86. https://doi.org/10.1016/j.jpowsour.2016.12.011.
[94] Nagpure SC, Bhushan B, Babu SS. Multi-Scale Characterization Studies of Aged Li-Ion Large Format Cells for Improved Performance: An Overview. J Electrochem Soc 2013;160:A2111–54. https://doi.org/10.1149/2.001311jes.
[95] J. Comyn. Adhesion Science 1997.

[96] Benedek I, Feldstein MM, editors. Handbook of Pressure-Sensitive Adhesives and Products: - Three Volume Set. Boca Raton: CRC Press; 2019. https://doi.org/10.1201/9780429151699.
[97] Sköld F, Bergengren E. An investigation on thin film adhesion measurement methods n.d.
[98] Mewis J, Wagner NJ. Colloidal Suspension Rheology. Cambridge: Cambridge University Press; 2011. https://doi.org/10.1017/CBO9780511977978.
[99] Hiemenz PC, Rajagopalan R, editors. Principles of Colloid and Surface Chemistry, Revised and Expanded. 3rd ed. Boca Raton: CRC Press; 2016. https://doi.org/10.1201/9781315274287.
[100] Tadros T. General Principles of Colloid Stability and the Role of Surface Forces. Colloid Stab., John Wiley & Sons, Ltd; 2006, p. 1–22. https://doi.org/10.1002/9783527631070.ch1.
[101] Evans DF, Wennerström H. The colloidal domain: where physics, chemistry, biology, and technology meet 1999.
[102] Lekkerkerker HNW, Tuinier R, Vis M. Colloids and the Depletion Interaction. Springer Nature; 2024. https://doi.org/10.1007/978-3-031-52131-7.
[103] Welch D, Lettinga MP, Ripoll M, Dogic Z, Vliegenthart GA. Trains, tails and loops of partially adsorbed semi-flexible filaments. Soft Matter 2015;11:7507–14. https://doi.org/10.1039/C5SM01457C.
[104] Vincent B, Edwards J, Emmett S, Jones A. Depletion flocculation in dispersions of sterically-stabilised particles (“soft spheres”). Colloids Surf 1986;18:261–81. https://doi.org/10.1016/0166-6622(86)80317-1.
[105] Fritz G, Schädler V, Willenbacher N, Wagner NJ. Electrosteric Stabilization of Colloidal Dispersions. Langmuir 2002;18:6381–90. https://doi.org/10.1021/la015734j.
[106] Buqa H, Holzapfel M, Krumeich F, Veit C, Novák P. Study of styrene butadiene rubber and sodium methyl cellulose as binder for negative electrodes in lithium-ion batteries. J Power Sources 2006;161:617–22. https://doi.org/10.1016/j.jpowsour.2006.03.073.
[107] Zhao Y, Yue F, Li S, Zhang Y, Tian Z, Xu Q, et al. Advances of polymer binders for silicon-based anodes in high energy density lithium-ion batteries. InfoMat 2021;3:460–501. https://doi.org/10.1002/inf2.12185.
[108] Reynolds CD, Lam J, Yang L, Kendrick E. Extensional rheology of battery electrode slurries with water-based binders. Mater Des 2022;222:111104. https://doi.org/10.1016/j.matdes.2022.111104.
[109] Reynolds CD, Hare SD, Slater PR, Simmons MJH, Kendrick E. Rheology and Structure of Lithium-Ion Battery Electrode Slurries. Energy Technol 2022;10:2200545. https://doi.org/10.1002/ente.202200545.
[110] Zhang YS, Bailey JJ, Sun Y, Boyce AM, Dawson W, Reynolds CD, et al. Applications of advanced metrology for understanding the effects of drying temperature in the lithium-ion battery electrode manufacturing process. J Mater Chem A 2022;10:10593–603. https://doi.org/10.1039/D2TA00861K.

[111] Fischer S, Doose S, Müller J, Höfels C, Kwade A. Impact of Spheroidization of Natural Graphite on Fast-Charging Capability of Anodes for LIB. Batteries 2023;9:305. https://doi.org/10.3390/batteries9060305.
[112] Jeschull F, Brandell D, Wohlfahrt-Mehrens M, Memm M. Water-Soluble Binders for Lithium-Ion Battery Graphite Electrodes: Slurry Rheology, Coating Adhesion, and Electrochemical Performance. Energy Technol 2017;5:2108–18. https://doi.org/10.1002/ente.201700200.
[113] Lestriez B. Functions of polymers in composite electrodes of lithium ion batteries. Comptes Rendus Chim 2010;13:1341–50. https://doi.org/10.1016/j.crci.2010.01.018.
[114] Dominko R, Gaberscek M, Drofenik J, Bele M, Pejovnik S, Jamnik J. The role of carbon black distribution in cathodes for Li ion batteries. J Power Sources 2003;119–121:770–3. https://doi.org/10.1016/S0378-7753(03)00250-7.
[115] Günther T, Billot N, Schuster J, Schnell J, Spingler FB, Gasteiger HA. The Manufacturing of Electrodes: Key Process for the Future Success of Lithium-Ion Batteries. Adv Mater Res 2016;1140:304–11. https://doi.org/10.4028/www.scientific.net/AMR.1140.304.
[116] Heimes HH, Offermanns C, Mohsseni A, Laufen H, Westerhoff U, Hoffmann L, et al. The Effects of Mechanical and Thermal Loads during Lithium-Ion Pouch Cell Formation and Their Impacts on Process Time. Energy Technol 2020;8:1900118. https://doi.org/10.1002/ente.201900118.
[117] Günter FJ, Wassiliadis N. State of the Art of Lithium-Ion Pouch Cells in Automotive Applications: Cell Teardown and Characterization. J Electrochem Soc 2022;169:030515. https://doi.org/10.1149/1945-7111/ac4e11.
[118] Qi Y, Harris SJ. In Situ Observation of Strains during Lithiation of a Graphite Electrode. J Electrochem Soc 2010;157:A741. https://doi.org/10.1149/1.3377130.
[119] Billot N, Günther T, Schreiner D, Stahl R, Kranner J, Beyer M, et al. Investigation of the Adhesion Strength along the Electrode Manufacturing Process for Improved Lithium-Ion Anodes. Energy Technol 2020;8:1801136. https://doi.org/10.1002/ente.201801136.
[120] Jeong D, Lee J. Electrode design optimization of lithium secondary batteries to enhance adhesion and deformation capabilities. Energy 2014;75:525–33. https://doi.org/10.1016/j.energy.2014.08.013.
[121] Jolley MJ, Pathan TS, Jenkins C, Loveridge MJ. Investigating the effect of the degree of cross-linking in styrene butadiene rubber on the performance of graphite anodes for the use in lithium-ion batteries. J Appl Polym Sci 2024;141:e55135. https://doi.org/10.1002/app.55135.
[122] Lim S, Kim S, Ahn KH, Lee SJ. Stress Development of Li-Ion Battery Anode Slurries during the Drying Process. Ind Eng Chem Res 2015;54:6146–55. https://doi.org/10.1021/acs.iecr.5b00878.
[123] Mayer D, Wurba A-K, Bold B, Bernecker J, Smith A, Fleischer J. Investigation of the Mechanical Behavior of Electrodes after Calendering and Its Influence on

Singulation and Cell Performance. Processes 2021;9:2009. https://doi.org/10.3390/pr9112009.
[124] Haselrieder W, Westphal B, Bockholt H, Diener A, Höft S, Kwade A. Measuring the coating adhesion strength of electrodes for lithium-ion batteries. Int J Adhes Adhes 2015;60:1–8. https://doi.org/10.1016/j.ijadhadh.2015.03.002.
[125] Lee J-H, Paik U, Hackley VA, Choi Y-M. Effect of poly(acrylic acid) on adhesion strength and electrochemical performance of natural graphite negative electrode for lithium-ion batteries. J Power Sources 2006;161:612–6. https://doi.org/10.1016/j.jpowsour.2006.03.087.
[126] Chen J, Liu J, Qi Y, Sun T, Li X. Unveiling the Roles of Binder in the Mechanical Integrity of Electrodes for Lithium-Ion Batteries. J Electrochem Soc 2013;160:A1502–9. https://doi.org/10.1149/2.088309jes.
[127] Sisanth KS, Thomas MG, Abraham J, Thomas S. General introduction to rubber compounding. Prog. Rubber Nanocomposites, Elsevier; 2017, p. 1–39. https://doi.org/10.1016/B978-0-08-100409-8.00001-2.
[128] Son B, Ryou M-H, Choi J, Lee T, Yu HK, Kim JH, et al. Measurement and Analysis of Adhesion Property of Lithium-Ion Battery Electrodes with SAICAS. ACS Appl Mater Interfaces 2014;6:526–31. https://doi.org/10.1021/am404580f.
[129] Jaiser S, Sanchez Salach N, Baunach M, Scharfer P, Schabel W. Impact of drying conditions and wet film properties on adhesion and film solidification of lithium-ion battery anodes. Dry Technol 2017;35:1807–17. https://doi.org/10.1080/07373937.2016.1276584.
[130] Park J, Willenbacher N, Ahn KH. How the interaction between styrene-butadiene-rubber (SBR) binder and a secondary fluid affects the rheology, microstructure and adhesive properties of capillary-suspension-type graphite slurries used for Li-ion battery anodes. Colloids Surf Physicochem Eng Asp 2019;579:123692. https://doi.org/10.1016/j.colsurfa.2019.123692.
[131] Baunach M, Jaiser S, Schmelzle S, Nirschl H, Scharfer P, Schabel W. Delamination behavior of lithium-ion battery anodes: Influence of drying temperature during electrode processing. Dry Technol 2016;34:462–73. https://doi.org/10.1080/07373937.2015.1060497.
[132] Marks T, Trussler S, Smith AJ, Xiong D, Dahn JR. A Guide to Li-Ion Coin-Cell Electrode Making for Academic Researchers. J Electrochem Soc 2011;158:A51. https://doi.org/10.1149/1.3515072.
[133] Schilling A, Schmitt J, Dietrich F, Dröder K. Analyzing Bending Stresses on Lithium-Ion Battery Cathodes induced by the Assembly Process. Energy Technol 2016;4:1502–8. https://doi.org/10.1002/ente.201600131.
[134] Smith A, Stüble P, Leuthner L, Hofmann A, Jeschull F, Mereacre L. Potential and Limitations of Research Battery Cell Types for Electrochemical Data Acquisition. Batter Supercaps 2023;6:e202300080. https://doi.org/10.1002/batt.202300080.
[135] Agubra VA, Fergus JW. The formation and stability of the solid electrolyte interface on the graphite anode. J Power Sources 2014;268:153–62. https://doi.org/10.1016/j.jpowsour.2014.06.024.

[136] Jeschull F, Maibach J, Edström K, Brandell D. On the Electrochemical Properties and Interphase Composition of Graphite: PVdF-HFP Electrodes in Dependence of Binder Content. J Electrochem Soc 2017;164:A1765–72. https://doi.org/10.1149/2.0121709jes.
[137] Zou F, Manthiram A. A Review of the Design of Advanced Binders for High-Performance Batteries. Adv Energy Mater 2020;10:2002508. https://doi.org/10.1002/aenm.202002508.
[138] Dai C, Wang Z, Liu K, Zhu X, Liao X, Chen X, et al. Effects of cycle times and C-rate on mechanical properties of copper foil and adhesive strength of electrodes in commercial LiCoO2 LIBs. Eng Fail Anal 2019;101:193–205. https://doi.org/10.1016/j.engfailanal.2019.03.015.
[139] INTERNATIONAL ENERGY AGENCY. Global EV Outlook 2024 2024.
[140] Miao Y, Hynan P, Jouanne A, Yokochi A. Current Li-Ion Battery Technologies in Electric Vehicles and Opportunities for Advancements. Energies 2019;12:1074. https://doi.org/10.3390/en12061074.
[141] Lopez CG, Rogers SE, Colby RH, Graham P, Cabral JT. Structure of Sodium Carboxymethyl Cellulose Aqueous Solutions: A SANS and Rheology Study. J Polym Sci Part B Polym Phys 2015;53:492–501. https://doi.org/10.1002/polb.23657.
[142] Lopez CG, Colby RH, Cabral JT. Electrostatic and Hydrophobic Interactions in NaCMC Aqueous Solutions: Effect of Degree of Substitution. Macromolecules 2018;51:3165–75. https://doi.org/10.1021/acs.macromol.8b00178.
[143] Lim S, Ahn KH, Yamamura M. Latex migration in battery slurries during drying. Langmuir ACS J Surf Colloids 2013;29:8233–44. https://doi.org/10.1021/la4013685.
[144] Westphal BG, Kwade A. Critical electrode properties and drying conditions causing component segregation in graphitic anodes for lithium-ion batteries. J Energy Storage 2018;18:509–17. https://doi.org/10.1016/j.est.2018.06.009.
[145] Chen H, Ling M, Hencz L, Ling HY, Li G, Lin Z, et al. Exploring Chemical, Mechanical, and Electrical Functionalities of Binders for Advanced Energy-Storage Devices. Chem Rev 2018;118:8936–82. https://doi.org/10.1021/acs.chemrev.8b00241.
[146] Petrie EM. Adhesive bonding of textiles: principles, types of adhesive and methods of use. Join. Text., Elsevier; 2013, p. 225–274101533978085709396722 25. https://doi.org/10.1533/9780857093967.2.225.
[147] McBain JW, Hopkins DG. On Adhesives and Adhesive Action. J Phys Chem 1925;29:188–204. https://doi.org/10.1021/j150248a008.
[148] Hofmann K, Hegde AD, Liu-Theato X, Gordon R, Smith A, Willenbacher N. Effect of mechanical properties on processing behavior and electrochemical performance of aqueous processed graphite anodes for lithium-ion batteries. J Power Sources 2024;593:233996. https://doi.org/10.1016/j.jpowsour.2023.233996.

[149] Sunghun Choi, Tae-woo Kwon, Ali Coskun, Jang Wook Choi. Highly elastic binders integrating polyrotaxanes for silicon microparticle anodes in lithium ion batteries. Science 2017;357:279–83. https://doi.org/10.1126/science.aal4373.
[150] Ye R, Liu J, Tian J, Deng Y, Yang X, Chen Q, et al. Novel Binder with Cross-Linking Reconfiguration Functionality for Silicon Anodes of Lithium-Ion Batteries. ACS Appl Mater Interfaces 2024;16:16820–9. https://doi.org/10.1021/acsami.4c00590.
[151] Yuanyuan Yu, Chen Yang, Yan Jiang, Jiadeng Zhu, Junhua Zhang, Mengjin Jiang. Consecutive covalent bonds reconstruct robust dual-interfaces by carbonized binder to enable conductive-additive-free durable silicon anode. Nano Energy 2024;130:110108. https://doi.org/10.1016/j.nanoen.2024.110108.
[152] Ren W-F, Le J-B, Li J-T, Hu Y-Y, Pan S-Y, Deng L, et al. Improving the Electrochemical Property of Silicon Anodes through Hydrogen-Bonding Cross-Linked Thiourea-Based Polymeric Binders. ACS Appl Mater Interfaces 2021;13:639–49. https://doi.org/10.1021/acsami.0c18743.
[153] Xiang Y, Xu H, Deng J, Li J, Nazir MA, Bao S-J. Spiderweb-like Three-Dimensional Cross-Linked AGE Binder for High Performance Silicon-Based Lithium Battery. ACS Appl Energy Mater 2025;8:2973–81. https://doi.org/10.1021/acsaem.4c03098.
[154] Kumberg J, Bauer W, Schmatz J, Diehm R, Tönsmann M, Müller M, et al. Reduced Drying Time of Anodes for Lithium-Ion Batteries through Simultaneous Multilayer Coating. Energy Technol 2021;9:2100367. https://doi.org/10.1002/ente.202100367.
[155] Cheol Bak, Kyung-Geun Kim, Hyuntae Lee, Seoungwoo Byun, Minhong Lim, Hyeongguk An, et al. Advanced multilayer model electrode for binder distribution within composite electrodes of lithium batteries. Chem Eng J 2024;483:148913. https://doi.org/10.1016/j.cej.2024.148913.
[156] Burger D, Keim N, Shabbir J, Gao Y, Müller M, Bauer W, et al. Simultaneous Primer Coating for Fast Drying of Battery Electrodes. Energy Technol 2025;13.3:2401668. https://doi.org/10.1002/ente.202401668.
[157] Mori T, Kitamura K. Effect of adsorption behaviour of polyelectrolytes on fluidity and packing ability of aqueous graphite slurries. Adv Powder Technol 2017;28:280–7. https://doi.org/10.1016/j.apt.2016.10.005.
[158] Huang L-H, Di Chen, Li C-C, Chang Y-L, Lee J-T. Dispersion Homogeneity and Electrochemical Performance of Si Anodes with the Addition of Various Water-Based Binders. J Electrochem Soc 2018;165:2239–46. https://doi.org/10.1149/2.0991810jes.
[159] Kim KJ, Ahn KH. Effects of sodium carboxymethyl cellulose and poly (acrylic acid) on the agglomeration behavior of aqueous silicon suspensions. Colloids Surf Physicochem Eng Asp 2023;673:131801. https://doi.org/10.1016/j.colsurfa.2023.131801.
[160] Park JH, Ahn CH, Ahn KH. Rheological behavior and microstructure formation of Si/C anode slurries for Li-ion batteries. Korea-Aust Rheol J 2023;35:335–47. https://doi.org/10.1007/s13367-023-00067-w.

[161] Kim B, Song Y, Youn B, Lee D. Dispersion Homogeneity of Silicon Anode Slurries with Various Binders for Li-Ion Battery Anode Coating. Polymers 2023;15. https://doi.org/10.3390/polym15051152.
[162] Haberzettl P, Filipovic N, Vrankovic D, Willenbacher N. Processing of Aqueous Graphite–Silicon Oxide Slurries and Its Impact on Rheology, Coating Behavior, Microstructure, and Cell Performance. Batteries 2023;9:581. https://doi.org/10.3390/batteries9120581.
[163] Andrews EH, Kinloch AJ, Melville HW. Mechanics of adhesive failure. I. Proc R Soc Lond Math Phys Sci 1973;332:385–99. https://doi.org/10.1098/rspa.1973.0032.
[164] Kinloch AJ, editor. Adhesion and adhesives: science and technology. Springer Science & Business Media.; 2012. https://doi.org/10.1007/978-94-015-7764-9.
[165] Shchipalov YK. Surface Energy of Crystalline and Vitreous Silica. Glass Ceram 2000:374–7. https://doi.org/10.1023/A:1010900903019.
[166] Adrian T. Murdock, Christian D. van Engers, Jude Britton, Vitaliy Babenko, Seyyed Shayan Meysami, Hugh Bishop, et al. Targeted removal of copper foil surface impurities for improved synthesis of CVD graphene. Carbon 2017;122:207–16. https://doi.org/10.1016/j.carbon.2017.06.075.
[167] Chang WJ, Lee GH, Cheon YJ, Kim JT, Lee SI, Kim J, et al. Direct Observation of Carboxymethyl Cellulose and Styrene–Butadiene Rubber Binder Distribution in Practical Graphite Anodes for Li-Ion Batteries. ACS Appl Mater Interfaces 2019;11:41330–7. https://doi.org/10.1021/acsami.9b13803.
[168] Burdette-Trofimov MK, Armstrong BL, Rogers AM, Heroux L, Doucet M, Yang G, et al. Understanding Binder–Silicon Interactions during Slurry Processing. J Phys Chem C 2020;124:13479–94. https://doi.org/10.1021/acs.jpcc.0c03660.
[169] Lee YM, Lee JY, Shim H-T, Lee JK, Park J-K. SEI Layer Formation on Amorphous Si Thin Electrode during Precycling. J Electrochem Soc 2007;154:A515. https://doi.org/10.1149/1.2719644.
[170] Zhang Q, Li W, Gu M, Jin Y. Dispersion and rheological properties of concentrated silicon aqueous suspension. Powder Technol 2006;161:130–4. https://doi.org/10.1016/j.powtec.2005.10.005.
[171] Vogl US, Das PK, Weber AZ, Winter M, Kostecki R, Lux SF. Mechanism of interactions between CMC binder and Si single crystal facets. Langmuir ACS J Surf Colloids 2014;30:10299–307. https://doi.org/10.1021/la501791q.
[172] Bitsch B. Verwendung von Kapillarsuspensionen zur Prozessierung von Lithium-Ionen Batterieelektroden. PhD. Dissertation. 2017. https://doi.org/10.5445/IR/1000064637.
[173] Guerfi A, Kaneko M, Petitclerc M, Mori M, Zaghib K. LiFePO4 water-soluble binder electrode for Li-ion batteries. J Power Sources 2007;163:1047–52. https://doi.org/10.1016/j.jpowsour.2006.09.067.
[174] Lee J-H, Kim J-S, Kim YC, Zang DS, Choi Y-M, Park WI, et al. Effect of Carboxymethyl Cellulose on Aqueous Processing of LiFePO[sub 4] Cathodes and Their Electrochemical Performance. Electrochem Solid-State Lett 2008;11:A175. https://doi.org/10.1149/1.2966286.

[175] Loeffler N, Kopel T, Kim G-T, Passerini S. Polyurethane Binder for Aqueous Processing of Li-Ion Battery Electrodes. J Electrochem Soc 2015;162:A2692–8. https://doi.org/10.1149/2.0641514jes.
[176] Jolley MJ, Pathan TS, Jenkins C, Loveridge MJ. Exploration of High and Low Molecular Weight Polyacrylic Acids and Sodium Polyacrylates as Potential Binder System for Use in Silicon Graphite Anodes. ACS Appl Energy Mater 2025;8:1647–60. https://doi.org/10.1021/acsaem.4c02672.
[177] Qi X, Song W, Shi J. Density functional theory study the effects of oxygen-containing functional groups on oxygen molecules and oxygen atoms adsorbed on carbonaceous materials. PLOS ONE 2017;12:e0173864. https://doi.org/10.1371/journal.pone.0173864.
[178] Magasinski A, Zdyrko B, Kovalenko I, Hertzberg B, Burtovyy R, Huebner CF, et al. Toward Efficient Binders for Li-Ion Battery Si-Based Anodes: Polyacrylic Acid. ACS Appl Mater Interfaces 2010;2:3004–10. https://doi.org/10.1021/am100871y.
[179] Mazouzi D, Karkar Z, Reale Hernandez C, Jimenez Manero P, Guyomard D, Roué L, et al. Critical roles of binders and formulation at multiscales of silicon-based composite electrodes. J Power Sources 2015;280:533–49. https://doi.org/10.1016/j.jpowsour.2015.01.140.
[180] Hofmann K, Willenbacher N. How carboxymethylcellulose adsorption and porous active material particles diminish the adhesion of graphite-silicon anodes in lithium-ion batteries. Energy Mater 2025;5. https://doi.org/10.20517/energymater.2024.281.
[181] Mintis DG, Mavrantzas VG. Effect of pH and Molecular Length on the Structure and Dynamics of Short Poly(acrylic acid) in Dilute Solution: Detailed Molecular Dynamics Study. J Phys Chem B 2019;123:4204–19. https://doi.org/10.1021/acs.jpcb.9b01696.
[182] Martins D, Dourado F, Gama M. Effect of ionic strength, pH and temperature on the behaviour of re-dispersed BC:CMC - A comparative study with xanthan gum. Food Hydrocoll 2023;135:108163. https://doi.org/10.1016/j.foodhyd.2022.108163.
[183] Kobayashi S, Müllen K, editors. Encyclopedia of Polymeric Nanomaterials. Berlin, Heidelberg: Springer Berlin Heidelberg; 2015. https://doi.org/10.1007/978-3-642-29648-2.
[184] Kam W, Liew C-W, Lim JY, Ramesh S. Electrical, structural, and thermal studies of antimony trioxide-doped poly(acrylic acid)-based composite polymer electrolytes. Ionics 2014;20:665–74. https://doi.org/10.1007/s11581-013-1012-0.
[185] Wang J, Zheng Q, Fang M, Ko S, Yamada Y, Yamada A. Concentrated Electrolytes Widen the Operating Temperature Range of Lithium-Ion Batteries. Adv Sci 2021;8:2101646. https://doi.org/10.1002/advs.202101646.
[186] Xie R, Weisen AR, Lee Y, Aplan MA, Fenton AM, Masucci AE, et al. Glass transition temperature from the chemical structure of conjugated polymers. Nat Commun 2020;11:893. https://doi.org/10.1038/s41467-020-14656-8.

[187] Kasinathan R, Marinaro M, Axmann P, Wohlfahrt–Mehrens M. Influence of the Molecular Weight of Poly-Acrylic Acid Binder on Performance of Si-Alloy/Graphite Composite Anodes for Lithium-Ion Batteries. Energy Technol 2018;6:2256–63. https://doi.org/10.1002/ente.201800302.

[188] Parikh P, Sina M, Banerjee A, Wang X, D'Souza MS, Doux J-M, et al. Role of Polyacrylic Acid (PAA) Binder on the Solid Electrolyte Interphase in Silicon Anodes. Chem Mater 2019;31:2535–44. https://doi.org/10.1021/acs.chemmater.8b05020.

[189] Li C, Shi T, Yoshitake H, Wang H. Improved performance in micron-sized silicon anodes by in situ polymerization of acrylic acid-based slurry. J Mater Chem A 2016;4:16982–91. https://doi.org/10.1039/C6TA05650D.

[190] Yi W, Zhao T, Li D, Yuan Q, Zhao Z, Chen B, et al. Research Progress of Polyacrylate Binders for Silicon-Based Anodes in Lithium-Ion Batteries. Chem – Eur J 2025;31:e202500321. https://doi.org/10.1002/chem.202500321.

[191] Gao Y, Qiu X, Wang X, Gu A, Zhang L, Chen X, et al. Chitosan- *g* -Poly(acrylic acid) Copolymer and Its Sodium Salt as Stabilized Aqueous Binders for Silicon Anodes in Lithium-Ion Batteries. ACS Sustain Chem Eng 2019;7:16274–83. https://doi.org/10.1021/acssuschemeng.9b03307.

[192] Zhao X, Yim C-H, Du N, Abu-Lebdeh Y. Crosslinked Chitosan Networks as Binders for Silicon/Graphite Composite Electrodes in Li-Ion Batteries. J Electrochem Soc 2018;165:A1110–21. https://doi.org/10.1149/2.114805jes.

[193] Zhong H, He J, Zhang L. Crosslinkable aqueous binders containing Arabic gum-grafted-poly (acrylic acid) and branched polyols for Si anode of lithium-ion batteries. Polymer 2021;215:123377. https://doi.org/10.1016/j.polymer.2020.123377.

[194] Preman AN, Aswale S, Salunkhe TT, Lee S, Kim MC, Devaraju S, et al. Better together: integrating adhesion and ion conductivity in composite binders for high-performance silicon anodes. J Mater Chem A 2025;13:8355–67. https://doi.org/10.1039/D4TA07078J.

[195] Jeong D, Yook J, Kwon D, Shim J, Lee J. Interweaving Elastic and Hydrogen Bond-Forming Polymers into Highly Tough and Stress-Relaxable Binders for High-Performance Silicon Anode in Lithium-Ion Batteries. Adv Sci 2023;10:2302027. https://doi.org/10.1002/advs.202302027.

[196] Wang C, Wu S, Weng J. Integrating with a tough framework and efficient self-healing behavior based on a flexible polymer skeleton for Si anode binders in lithium-ion cells. J Energy Storage 2024;80:110314. https://doi.org/10.1016/j.est.2023.110314.

[197] Lv P, Liu H, Cui Z, An H, Yang M, Xie S, et al. Covalently cross-linked waterborne polyurethane acrylate network binder for low-expansion silicon / carbon anode. J Power Sources 2025;655:237985. https://doi.org/10.1016/j.jpowsour.2025.237985.

[198] Baudonnet L, Grossiord J -L., Rodriguez F. Effect of Dispersion Stirring Speed on the Particle Size Distribution and Rheological Properties of Three Carbomers. J Dispers Sci Technol 2004;25:183–92. https://doi.org/10.1081/DIS-120030665.

[199] Oelschlaeger C, Marten J, Péridont F, Willenbacher N. Imaging of the microstructure of Carbopol dispersions and correlation with their macroelasticity: A micro- and macrorheological study. J Rheol 2022;66:749–60. https://doi.org/10.1122/8.0000452.
[200] Kowalczyk A, Oelschlaeger C, Willenbacher N. Visualization of micro-scale inhomogeneities in acrylic thickener solutions: A multiple particle tracking study. Polymer 2015;58:170–9. https://doi.org/10.1016/j.polymer.2014.12.041.
[201] Dyhr K, Willenbacher N. Formulating Graphite-Filled PU Dispersions with Extended Shelf Life Using the Capillary Suspension Concept. Colloids Interfaces 2025;9:26. https://doi.org/10.3390/colloids9030026.
[202] Balmforth NJ, Frigaard IA, Ovarlez G. Yielding to Stress: Recent Developments in Viscoplastic Fluid Mechanics. Annu Rev Fluid Mech 2014;46:121–46. https://doi.org/10.1146/annurev-fluid-010313-141424.
[203] Beris AN, Tsamopoulos JA, Armstrong RC, Brown RA. Creeping motion of a sphere through a Bingham plastic. J Fluid Mech 1985;158:219–44. https://doi.org/10.1017/S0022112085002622.
[204] Bitsch B, Dittmann J, Schmitt M, Scharfer P, Schabel W, Willenbacher N. A novel slurry concept for the fabrication of lithium-ion battery electrodes with beneficial properties. J Power Sources 2014;265:81–90. https://doi.org/10.1016/j.jpowsour.2014.04.115.
[205] Westphal B, Bockholt H, Günther T, Haselrieder W, Kwade A. Influence of Convective Drying Parameters on Electrode Performance and Physical Electrode Properties. ECS Trans 2015;64:57–68. https://doi.org/10.1149/06422.0057ecst.
[206] Tian R, Park S-H, King PJ, Cunningham G, Coelho J, Nicolosi V, et al. Quantifying the factors limiting rate performance in battery electrodes. Nat Commun 2019;10:1933. https://doi.org/10.1038/s41467-019-09792-9.
[207] Gordon R, Smith A. Towards more realistic Li-ion battery safety tests based on Li-plating as internal cell error. J Energy Storage 2023;72:108200. https://doi.org/10.1016/j.est.2023.108200.
[208] Ui K, Fujii D, Niwata Y, Karouji T, Shibata Y, Kadoma Y, et al. Analysis of solid electrolyte interface formation reaction and surface deposit of natural graphite negative electrode employing polyacrylic acid as a binder. J Power Sources 2014;247:981–90. https://doi.org/10.1016/j.jpowsour.2013.08.083.